

6-2022

AERODYNAMICS AND AEROACOUSTICS OPTIMIZATION OF VEHICLE'S SIDE MIRROR BASE AND EXHAUST PIPE

Moath Nayef Mohamed Zaareer

Follow this and additional works at: https://scholarworks.uaeu.ac.ae/all_theses



Part of the [Aerospace Engineering Commons](#), and the [Mechanical Engineering Commons](#)

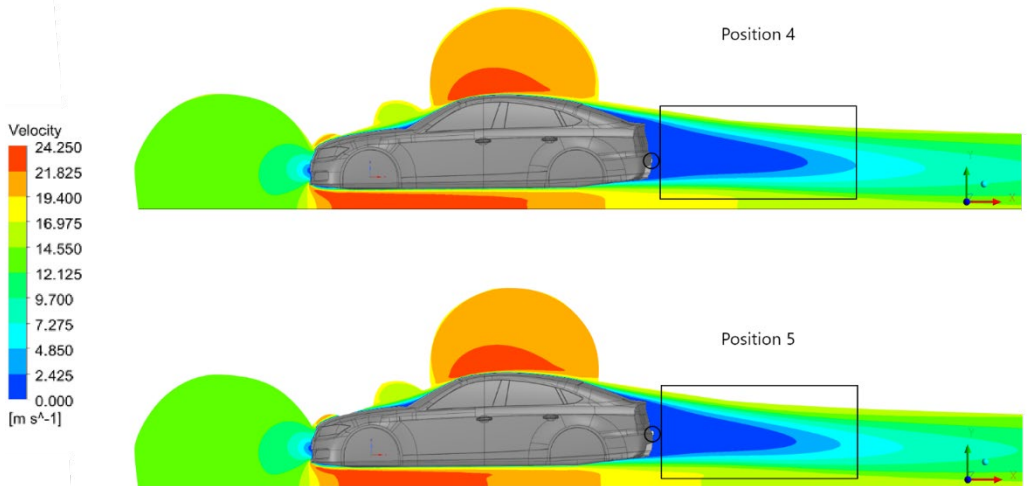
MASTER THESIS NO. 2022: 39

College of Engineering

Department of Mechanical and Aerospace Engineering

AERODYNAMICS AND AEROACOUSTICS
OPTIMIZATION OF VEHICLE'S SIDE MIRROR
BASE AND EXHAUST PIPE

Moath Nayef Mohamed Zaareer



June 2022

United Arab Emirates University

College of Engineering

Department of Mechanical and Aerospace Engineering

AERODYNAMICS AND AEROACOUSTICS
OPTIMIZATION OF VEHICLE'S SIDE MIRROR BASE
AND EXHAUST PIPE

Moath Nayef Mohamed Zaareer

This thesis is submitted in partial fulfillment of the requirements for the
degree of Master of Science in Mechanical Engineering

June 2022


**United Arab Emirates University Master Thesis
2022: 39**

Cover: The following image shows a 2D analysis conducted in ANSYS fluent on the popular experimentally verified DrivAer model. The simulation shows the difference between placing the exhaust pipe at 9 different locations, and the image compares two of those positions. The results are shown for the velocity contour from ANSYS.

(Photo: by Moath Nayef Mohamed Zaareer)

Declaration of Original Work

I, Moath Nayef Mohamed Zaareer, the undersigned, a graduate student at the United Arab Emirates University (UAEU), and the author of this thesis entitled “*Aerodynamics and Aeroacoustics Optimization of Vehicle’s Side Mirror Base and Exhaust Pipe*”, hereby, solemnly declare that this is the original research work done by me under the supervision of Professor Abdel-Hamid Ismail Mourad, in the College of Engineering at UAEU. This work has not previously formed the basis for the award of any academic degree, diploma or a similar title at this or any other university. Any materials borrowed from other sources (whether published or unpublished) and relied upon or included in my thesis have been properly cited and acknowledged in accordance with appropriate academic conventions. I further declare that there is no potential conflict of interest with respect to the research, data collection, authorship, presentation and/or publication of this thesis.

Student’s Signature: _____  _____

Date: ___ 14 April 2022 _____

Advisory Committee

1) Advisor: Abdel-Hamid Ismail Mourad

Title: Professor

Department of Mechanical and Aerospace Engineering

College of Engineering

2) Co-advisor: Tariq Darabseh

Title: Associate Professor

Department of Aeronautical Engineering

College of Engineering, Jordan University of Science and Technology,

Jordan

Approval of the Master Thesis

This Master Thesis is approved by the following Examining Committee Members:

- 1) Advisor (Committee Chair): Abdel-Hamid Ismail Mourad

Title: Professor

Mechanical and Aerospace Engineering Department

College of Engineering

Signature 

Date 29-6-2022

- 2) Member: Sanan Husain Khan

Title: Assistant Professor

Mechanical and Aerospace Engineering Department

College of Engineering

Signature 


Date 29-6-2022

- 3) Member (External Examiner): Kefu Liu

Title: Professor

Mechanical Engineering Department

Lakehead University, Thunder Bay, Ont, Canada

Signature 

Date 29-6-2022

Dr. E. Elhajjar.

This Master Thesis is accepted by:

Acting Dean of the College of Engineering: Professor Mohamed Al-Marzouqi

Signature: Mohamed Al-Marzouqi

Date: August 01, 2022

Dean of the College of Graduate Studies: Professor Ali Al-Marzouqi

Signature: Ali Hassan

Date: August 07, 2022

Abstract

This thesis is concerned with studying two different vehicle parts in terms of aerodynamics and aeroacoustics. Two main factors determine the efficiency and luxury of the vehicle, the low aerodynamic forces and low noise emission. The aerodynamic drag coefficient is concerned with how easy a vehicle can travel through the air; the lower the value, the less fuel is needed to move the vehicle forward and less air resistance the vehicle faces. The aerodynamic lift coefficient is related to vehicle ground stability, and the more negative the value is, the higher the vehicle's stability. Moreover, the aeroacoustics is concerned with noise generated from air interacting with a body, and the lower the noise emitted, the higher the ride comfort of the passengers.

The main objective of this thesis is to optimize the parts' performance in terms of aerodynamics and aeroacoustics. The effect of changing the mirror base orientation on aerodynamics and aeroacoustics is desired. The optimum angle position for the mirror arm that results in the least aerodynamic forces and acoustics is desired. Furthermore, the exhaust pipe generates noise that affects the nearby pedestrians and influences aerodynamic forces. Therefore, the aim is to test nine different height levels for the exhaust pipe on the rear of the vehicle and record the drag and lift coefficient effect on the entire vehicle. The desired optimization is to lower the drag and lift force values and the generated acoustics from the part. The software ANSYS fluent is used for simulating each case.

The results show that by changing the mirror's base while keeping the projected area constant, there is no noticeable effect on the aerodynamic forces but has a significant effect on acoustics. Furthermore, the optimum angle orientation for the base is $\sim 85 \pm 3.75$ degrees, as this position results in the least acoustics generated. The mirror's base orientation has a significant

difference of up to 32 decibels in sound pressure level when comparing them side mirror base at 85 degrees to 45 degrees. The exhaust pipe is added at different heights, and resulting aerodynamic forces are compared with the original model without an exhaust outlet. When the exhaust pipe is placed 100 mm (position 5) above the bottom rear, it results in the lowest drag coefficient value (0.9% difference) compared to the original DrivAer model without an exhaust system. Furthermore, the position for the highest negative lift coefficient is located 125 mm (position 6) above the bottom rear, with a difference of $\sim 7.7\%$.

The mirror base has been completely ignored and overlooked in the literature. However, this thesis contributed significantly to the base mirror by determining a standard position that results in the lowest acoustics generation. The exhaust system's effect on aerodynamic forces is lacking in studies compared to other vehicle parts. This thesis contributed to the aerodynamic optimization of a vehicle by studying the effect of the exhaust system and determining a design standard position that results in the lowest aerodynamic forces.

Keywords: Aeroacoustics, aerodynamics, rear exhaust pipe, side mirror base, vehicle noise sources.

Title and Abstract (in Arabic)

التحسين الهوائي والصوتي لقاعدة المرآة الجانبية للسيارة وأنبوب العادم

الملخص

تهتم هذه الأطروحة بدراسة جزأين مختلفين للمركبة من حيث الديناميكا الهوائية والصوتيات الهوائية. هناك عاملان رئيسيان يحددان كفاءة ورفاهية السيارة، القوى الديناميكية الهوائية المنخفضة وانبعثات الضوضاء المنخفض. يُعنى معامل السحب الديناميكي الهوائي بمدى سهولة انتقال السيارة في الهواء، فكلما انخفضت القيمة، كلما قل الوقود المطلوب لتحريك السيارة للأمام وأقل مقاومة الهواء التي تواجهها السيارة. يرتبط معامل الرفع الديناميكي الهوائي باستقرار السيارة على الأرض، وكلما كانت القيمة أكثر سلبية، زاد استقرار السيارة. علاوة على ذلك، فإن الصوتيات الهوائية تهتم بالضوضاء الناتجة عن تفاعل الهواء مع الجسم، وكلما انخفضت الضوضاء المنبعثة، زادت راحة الركوب للركاب.

الهدف الرئيسي من هذه الأطروحة هو تحسين أداء الأجزاء من حيث الديناميكا الهوائية والصوتيات الهوائية. العاملان الرئيسيان في حدوث ضوضاء من السيارة هما جزء المرآة ونظام العادم. المطلوب معرفته هو تأثير تغيير اتجاه قاعدة المرآة على الديناميكا الهوائية والصوتيات الهوائية. نظرًا لأنه يمكن توجيه قاعدة المرآة من 0 إلى 90 درجة بالنسبة للمحور الذي يربط المرآة بقاعدتها، فإن موضع الزاوية الأمثل الذي ينتج عنه أقل قوى ديناميكية هوائية والصوتيات المتولدة مطلوبة. علاوة على ذلك، يولد أنبوب العادم ضوضاء تؤثر على المشاة القريبين والأشخاص داخل السيارة ويؤثر على القوى الديناميكية الهوائية. نظرًا لأن أنبوب العادم يخرج الغازات، تتفاعل كتلة المخرج مع الهواء الخارجي وتؤثر على خطوط ضغط الهواء، مما يؤثر على القوى الديناميكية الهوائية. لذلك، الهدف هو اختبار تسعة مستويات ارتفاع مختلفة لأنبوب العادم في الجزء الخلفي من السيارة وتسجيل تأثير معامل السحب والرفع على السيارة بأكملها. التحسين المطلوب هو خفض قيم قوة السحب والرفع والصوتيات المتولدة من الجزء. يتم حل كل حالة عددًا باستخدام تقنيات ديناميكيات الموائع الحسابية (CFD) التي تطبق معايير التشغيل والهندسة المختلفة. يتم استخدام برنامج ANSYS بطلاقة لمحاكاة كل حالة.

يتم التحقق من صحة النتائج التي تم الحصول عليها من خلال القيم التجريبية الموجودة المقابلة في الأدبيات. تظهر النتائج أنه من خلال تغيير قاعدة المرآة مع الحفاظ على المنطقة المسقطة ثابتة، لا يوجد تأثير ملحوظ على القوى الديناميكية الهوائية ولكن لها تأثير كبير على الصوتيات. علاوة

على ذلك، فإن الاتجاه الأمثل للزاوية للقاعدة هو 85 ± 3.75 درجة، حيث ينتج عن هذا الموضع أقل الأصوات المولدة. يحتوي اتجاه قاعدة المرآة على فرق كبير يصل إلى 32 ديسيبل في مستوى ضغط الصوت عند مقارنتها بقاعدة المرآة الجانبية عند 85 درجة إلى 45 درجة. أنبوب العادم له تأثير ملحوظ على الديناميكا الهوائية للسيارة، لذا فإن وضع أنبوب العادم ضروري. يكون الوضع المعتاد للجزء السفلي الخلفي الذي سيتم وضع العادم فيه غير فعال عند محاكاته على طراز DrivAer، حيث يتم إضافة أنبوب العادم على ارتفاعات مختلفة، ويتم مقارنة القوى الديناميكية الهوائية الناتجة مع النموذج الأصلي بدون مخرج عادم. تم التوصل إلى وضعين لإنتاج أقل قوى ديناميكية هوائية، أحدهما للسحب والآخر للرفع. عندما يتم وضع أنبوب العادم على ارتفاع 100 مم (الموضع 5) فوق المؤخرة السفلية للسيارة، فإنه ينتج عنه أقل قيمة لمعامل سحب (فرق 0.9%) مقارنةً بطراز DrivAer الأصلي بدون نظام عادم. علاوة على ذلك، فإن موضع أعلى معامل رفع سلبي يقع 125 مم (الموضع 6) فوق المؤخرة السفلية، بفارق $\sim 7.7\%$.

تم تجاهل قاعدة المرآة تمامًا وتجاهلها في الأدبيات القديمة. ولهذا السبب، فإن هذه الأطروحة ساهمت بشكل كبير في المرآة الأساسية من خلال تحديد موضع قياسي ينتج عنه أقل توليد صوتيات الذي لم يتم دراسته من قبل. يمكن لمصممي السيارات الآن تصميم قاعدة مرآة السيارة بناءً على القيمة التي تم الحصول عليها في هذه الأطروحة. تأثير نظام العادم على القوى الديناميكية الهوائية يفتقر إلى الدراسات مقارنة بأجزاء السيارة الأخرى. ساهمت هذه الأطروحة في تحسين الديناميكية الهوائية للسيارة من خلال دراسة تأثير نظام العادم وتحديد موضع قياسي للتصميم ينتج عنه أقل قوى ديناميكية هوائية.

مفاهيم البحث الرئيسية: الصوتيات الهوائية، الديناميكا الهوائية، أنبوب العادم الخلفي، قاعدة المرآة الجانبية، مصادر ضوضاء السيارة.

Author Profile

Moath Nayef Mohamed is a mechanical engineering with experience in maintenance engineering. As he did an internship in TRANSCO (a water distribution company) and held the position of maintenance supervisor. In his bachelors he undertook two Summer Undergraduate Research Experiences (SURE) programs and one Undergraduate Research Opportunities (UGRO), having this experience introduced me to the research field and publications. Moath gained a lot of experience in research by enrolling in university research programs.

In SURE the first project was to measure the value of the spring back of sheet metals for different materials, by bending in a specific angle and recording the final angle reached. The second project was about the effect of the language used by teachers on student's understanding. In the UGRO project, the improvement of the physical properties of memory foam materials is desired, by inserting iron nanoparticles.

After his bachelor's degree and with the knowledge and experiences Moath accumulated, He started to work on my first journal research publication and in March 2021 it got published. Currently Moath has 3 publications (2 journal, 1 conference) with h-index of 1. After Moath published an article, this encouraged him to work more and harder to pursue higher ranked journals. During his master's he prepared 3 publications and 3 more are under work (total 6 publications) from his thesis for journal publication. Currently, one is published in a well renowned Q1 journal (Alexandria Engineering), other is under review in a respected journal, and the other manuscript are currently being prepared for publication.

Acknowledgements

First and foremost, I thank Allah for all the strength he had given me in completing my master's thesis. Allah had given me such a wonderful experience with lovely companions of families, lecturers, and friends. Through hardship, Allah assisted me heaps. There are a lot of things I had gained and learned upon the path I was destined to be in. The knowledge I had obtained which I cannot seek from anywhere will always be remembered Insha'Allah.

Then, I would like to thank and express my sincere gratitude to the person who made this thesis possible and an enjoyable experience for me, my supervisor, Prof. Abdel-Hamid Ismail Mourad as he acted as a father figure to me and guided and encouraged me to finish this thesis. Prof. Abdel-Hamid gave me the freedom to express my ideas and ambitions and acted as a guide in this journey, also would like to thank him for helping me and supporting me through throughout the thesis. The supervisor enabled me to explore a small part of the Mechanical Engineering field in a very efficient way. The motivation and courage given will be remembered by heart, always.

On top of all, I am extremely grateful to my family members who always give me support through my thick and thin, especially my father Prof. Nayef Ghasem, and my brother Dr. Maan Al Zareer. This thesis would not have been possible if Allah hadn't provided them to help me and guide me throughout this journey. The love, hopes, and prayers will never be repaid throughout my entire life. Also, my thanks go to a special teacher that helped me and supplied me with information, Dr. Emad Al Najjar. Dr. Emad always welcomed me and willingly answered every question I had.

Dedication

I dedicate this to my family for their help and support.

Table of Contents

Title	i
Declaration of Original Work.....	iii
Advisory Committee	iv
Approval of the Master Thesis	v
Abstract	vii
Title and Abstract (in Arabic).....	ix
Author Profile.....	xi
Acknowledgements	xii
Dedication	xiii
Table of Contents	xiv
List of Tables.....	xvi
List of Figures	xviii
List of Abbreviation	xxiii
Chapter 1: Introduction	3
1.1 Overview.....	3
1.2 Statement of the problem	5
1.3 Research objectives.....	6
1.4 Relevant literature	8
1.4.1 Looks versus practicality	12
1.4.2 Aeroacoustics.....	13
1.4.3 Vehicle side mirror	17
1.4.4 Airflow numerical models	20
1.4.5 Mesh analysis.....	22
1.4.6 Rear exhaust effect on aerodynamics	24
1.5 Structure of the thesis.....	25
Chapter 2: Methodology.....	29
2.1 Design and geometry	29

2.1.1 Side mirror base part 1 geometry design	29
2.1.2 Side mirror base part 2 geometry design	33
2.1.3 Vehicle rear exhaust geometry design	37
2.2 CFD analysis	42
2.2.1 Material properties	42
2.2.2 Governing equations and model assumptions	43
2.2.3 Numerical setup	59
2.2.3 Boundary conditions	65
2.3 Model validation	68
Chapter 3: Results and Discussion	73
3.1 Geometry meshing and convergence	73
3.1.1 Side mirror base meshing	74
3.1.2 Side mirror base part 2 geometry meshing	76
3.1.3 Different exhaust pipe positions mesh model	79
3.2 CFD simulation and results	84
3.2.1 Side mirror base part 1 results	85
3.2.2 Side mirror base results and discussion	93
3.2.3 Exhaust pipe at different positions results and discussion	115
Chapter 4: Conclusions and Future Work	125
4.1 Conclusions	125
4.2 Future work	126
References	127
List of Publications	136

List of Tables

Table 1: Summary of novel and innovative articles that concern airflow on side mirrors.....	19
Table 2: Summary of simulation methods used to represent airflow.	21
Table 3: Review of articles on other sections of the vehicle.....	23
Table 4: Operating settings used for exhaust simulation.....	43
Table 5: Setup comparison between low computational cost versus numerical accuracy	54
Table 6: Values taken in solving for mass exhaust out	58
Table 7: ANSYS functions and model parameter chosen.	60
Table 8: Methodology used in ANSYS.....	63
Table 9: Methodology used in simulating different exhaust pipe positions and DrivAer model validation.....	64
Table 10: Boundary conditions for mirror base part 2 with reference to Figure 26.....	66
Table 11: Boundary conditions set for every exhaust simulation	68
Table 12: Difference between tetrahedral and polyhedral meshing.	75
Table 13: Tetrahedral mesh analysis number of nodes and elements.	77
Table 14: Polyhedral mesh analysis and size.	77
Table 15: Initial results and the resulted averaged values from the simulation.....	83
Table 16: 2D DrivAer model mesh setup.....	84
Table 17: Angular base mirror acoustics.....	86
Table 18: Horizontal base mirror acoustics.....	86
Table 19: Angular base mirror force results.....	88
Table 20: Horizontal base mirror force results.....	89

Table 21: Receiver 1 to 12 values for the SPL magnitude for the base angle position and the duration it maintains being the lowest in frequency (Hz). 96

Table 22: Receiver 13 values for the SPL magnitude for the base angle position and the duration it maintains being the lowest in frequency (Hz). 97

Table 23: Each receiver number and the mirror base angle that results lowest generated SPL for the longest frequency period..... 98

Table 24: Aerodynamic forces values for exhaust located at positions 1 to 3 with change %. 118

Table 25: Aerodynamic forces values for exhaust located at positions 4 to 6 with change %. 118

Table 26: Aerodynamic forces values for exhaust located at positions 7 to 9 with change %. 118

Table 27: Drag coefficient values: comparison between experimental and numerical..... 120

List of Figures

Figure 1: The vehicle has 3 pillars, A (red), B (green), C (blue) Pillars of the vehicle.	6
Figure 2: Drag coefficient for different shapes and vehicles.....	9
Figure 3: Noise scale for SPL in dB.....	10
Figure 4: Different sections of a vehicle, front (light blue), side (dark blue), back (purple), and wheels (orange).	12
Figure 5: Noise generation from side mirror to passenger’s ears.....	15
Figure 6: Aero-Vibro-Acoustics model of how vortices outside the vehicle, translate into interior noise.	17
Figure 7: Drag coefficient variation when exhaust pipe placed at different positions.	25
Figure 8: Geometry design process based on Camry model, taking two study cases with different angles, 21.25 degrees base mirror (left) and 0 degrees base mirror (right).....	30
Figure 9: Horizontal base (left) & angular base (right).....	31
Figure 10: Horizontal base CAD geometry dimensions.....	32
Figure 11: Angular base CAD geometry dimensions.....	32
Figure 12: Horizontal mirror Mercedes-Benz (left) and vertical mirror Rolls Royce (right).	33
Figure 13: Isometric view for the case study.....	35
Figure 14: Front view of the investigated case study, with side mirror on the left and mirror part is in grey color, and the base is changing positions.	36
Figure 15: The exhaust pipe can be placed at different positions, either on the top of the vehicle like McLaren (left), or at the bottom of the rear like BMW (right).....	37
Figure 16: 2D DrivAer model validation and exhaust system study case.	39

Figure 17: DrivAer model isometric view.....	40
Figure 18: DrivAer model 35% scale dimensions from original model.....	41
Figure 19: CFD analysis framework.....	42
Figure 20: LES perception of flow.....	51
Figure 21: Illustration of Detached Eddy Simulation.....	51
Figure 22: Green Gauss and Node Based methods for computing the gradient.....	55
Figure 23: Least-Squares Cell Method for calculating the gradient.....	56
Figure 24: Receivers location on vehicle's side.....	62
Figure 25: Exhaust pipe different testing positions, with spacing of 25 mm.....	65
Figure 26: View of the case study, without the outside boundary wall (top), and with the boundary wall (bottom).....	67
Figure 27: Boundary labels for 2D simulation.....	68
Figure 28: Geometry studied for side mirror base part 1 with generated mesh.....	75
Figure 29: Mesh refining for studying the effect changing the side mirror base have on the drag force (N) with respect to the number of elements.....	76
Figure 30: Mesh display for the investigated case shows edges, faces, and partitions inside the studied geometry.....	78
Figure 31: Mesh refining for studying the optimum mirror base orientation that results lowest aeroacoustics and/or aerodynamic forces, the drag force (N) is plotted with respect to the number of elements.....	78
Figure 32: Inflation layer (ANSYS Fluent property) on the wall to represent BLS.....	80
Figure 33: Mesh view showing DrivAer model and mesh.....	81

Figure 34: Mesh refining for the 2D DrivAer model to simulate different exhaust pipe position at the error at measure the aerodynamic forces at each position.....	82
Figure 35: Maximum acoustics value at different airflow inlet velocity for angular and horizontal base position.....	85
Figure 36: Drag force values at different airflow inlet velocities for angular and horizontal base position.....	87
Figure 37: Lift force values at different airflow inlet velocities for angular and horizontal base position.....	88
Figure 38: Rear side view of angularly placed mirror base (left) and horizontally placed mirror base (right).....	90
Figure 39: Isometric view for the angularly placed mirror base (left) and front left side view for the horizontally placed mirror base (right).....	91
Figure 40: Side view for both positions.....	92
Figure 41: Driver side in vehicle modelled and receivers' location are placed near the occupants' ears.....	94
Figure 42: Receiver 1 SPL vs frequency with different mirror base angle positions, with the lowest angle position and the range of frequencies it remains the lowest.....	95
Figure 43: Turbulence kinetic energy isometric view comparing between 45 and 85 degrees.....	102
Figure 44: Turbulence Kinetic Energy side profile view comparing between 45 and 85 degrees.....	102
Figure 45: SPL at different receivers for fixed frequency of around 300 Hz: Comparison between 45 and 85 degrees.....	103
Figure 46: Aerodynamic forces for the mirror part and SPL at receiver 13 both presented for each mirror base angle.....	105
Figure 47: Obtained results compared with previous work done in literature.....	107

Figure 48: Receiver 1 at different mirror base angles original results from ANSYS solver.	108
Figure 49: Receiver 1 at different mirror base angles with 4 th order polynomial.	108
Figure 50: Receiver 2 at different mirror base angles with 4 th order polynomial.	109
Figure 51: Receiver 3 at different mirror base angles with 4 th order polynomial.	109
Figure 52: Receiver 4 at different mirror base angles with 4 th order polynomial.	110
Figure 53: Receiver 5 at different mirror base angles with 4 th order polynomial.	110
Figure 54: Receiver 6 at different mirror base angles with 4 th order polynomial.	111
Figure 55: Receiver 7 at different mirror base angles with 4 th order polynomial.	111
Figure 56: Receiver 8 at different mirror base angles with 4 th order polynomial.	112
Figure 57: Receiver 9 at different mirror base angles with 4 th order polynomial.	112
Figure 58: Receiver 10 at different mirror base angles with 4 th order polynomial.	113
Figure 59: Receiver 11 at different mirror base angles with 4 th order polynomial.	113
Figure 60: Receiver 12 at different mirror base angles with 4 th order polynomial.	114
Figure 61: Receiver 13 at different mirror base angles with 4 th order polynomial.	114
Figure 62: DrivAer 2D fastback model without wheels, with exhaust pipe at the rear of the vehicle positioned at 9 different locations (zoom out of Figure 25).....	115
Figure 63: Drag coefficient plot for each exhaust pipe position.	116
Figure 64: Lift coefficient plot for each exhaust pipe position.	116

Figure 65: Velocity contours for exhaust located at position
6 and 9. 119

Figure 66: Velocity contours for exhaust located at position
4 and 5. 119

List of Abbreviation

APL	Acoustic Power Level
BL	Boundary Layer
CAD	Computer Aided Design
Cd	Drag Coefficient
CFD	Computational Fluid Dynamics
Cl	Lift Coefficient
CM	Coarse Mesh
CSM	Car Side Mirror
dB	Decibels
DES	Detached Eddy Simulation
DNS	Direct Numerical Simulation
FM	Fine Mesh
FW-H	Ffowcs Williams Hawkings
LES	Large-Eddy Simulation
MM	Medium Mesh
PISO	Pressure Implicit with Splitting of Operators
PISO	Pressure Implicit of Split Operations
RANS	Reynolds Averaged Navier Stokes
SA	Spalart-Allmaras
SAE	Society of Automotive Engineers

SAS	Scale Adaptive Simulation
SIMPLE	Semi Implicit Method for Pressure Linked Equations
SPL	Sound Pressure Level
TBL	Turbulent Boundary Layer
TKE	Turbulent Kinetic Energy
URANS	Unsteady Reynolds Averaged Navier Stokes
WPF	Wall Pressure Fluctuation
C_1 (Unitless)	K-Epsilon Coefficient
C_2 (Unitless)	K-Epsilon Coefficient
C_μ (Unitless)	K-Epsilon Coefficient
D (Newton)	Drag Force
g (m/s^2)	Gravity
L (Newton)	Lift Force
n (Unitless)	Normal Vector Directed Outward
p (Pascal)	Pressure Fields
S (m^2)	Closed Surface
t (Second)	Time Step
U (m/s)	Velocity Vector
V (Unitless)	Domain of Interest
α (Unitless)	K-Omega Coefficient
β (Unitless)	K-Omega Coefficient

δ (Unitless)	Partial
ε (NA)	Viscous Stress Tensor
μ ($Kg/(m \cdot s)$)	Molecular Dynamics Viscosity
ρ (Kg/m^3)	Density
σ (NA)	Total Stress Tensor
τ (NA)	Elastic Stress Tensor
Δ (m or cm)	Delta
m	Meter
dB	Decibel
Km	Kilometer
h	Hour
s	Second
N	Newton
i/x	Unit Vector in x-direction
j/y	Unit Vector in y-direction
k/z	Unit Vector in z-direction

Chapter 1

Chapter 1: Introduction

1.1 Overview

With the lower demand and higher prices of new cars, the automotive industry is reaching a high level of competitiveness. The automotive companies are forced to provide the best performance, ride quality, comfort, and efficiency at a lower price than their counterparts, especially with ever-aware customers. This competitiveness is reflected in more attractive and efficient design, more extended range, higher comfortability, and ride quality while maintaining lower prices. Efficiency and exterior design are linked through aerodynamics, as the lower the drag coefficient, the longer the car range, which determines the car's exterior shape. Furthermore, comfort and ride quality are linked through aeroacoustics and the level of noise emitted from the vehicle at highway speeds that reach the cabin. Aerodynamics and aeroacoustics (AD & AA) study concerns of how air interacts with a certain body. Aerodynamics is how an object moves through air and has two parameters, drag force and lift force. Drag force acts in the opposite direction to the vehicle's movement, while lift force is in the perpendicular direction to the ground. Both drag and lift forces are considered in the vehicle design phase, and designers take into consideration lowering the drag coefficient and increasing the negative lift coefficient (towards the ground) as much as possible. However, aeroacoustics deals with air emitting sound when interacting with an object. To illustrate, turbulent air has vortices that cause vibration in surrounding objects that are translated into unpleasant noise. In automotive design, different fields of science are combined to result in a vehicle that includes aerodynamics and aeroacoustics, which will be discussed in this thesis. Currently, consumers look for vehicles with higher energy efficiency for longer ranges and high quality of riding.

Higher efficiency and lower fuel/electricity consumption are directly related to the aerodynamic forces, the drag and lift force. The lower the drag coefficient value is, the less energy is needed to move forward as the vehicle experiences less air resistance that hinders the vehicle's movement. Moreover, besides having an efficiency effect, the lift coefficient directly affects the on-ground stability of the car because, unlike the aerospace industry, the lift is desired for plane take-off. However, cars must remain on the ground, and the more negative the lift coefficient, the higher the vehicle's stability. The positive axis is perpendicular to the ground in terms of lift, so a negative value is desired to push the body down to the ground and maintain wheel road contact. Furthermore, the lower the drag coefficient, the lower the fuel consumption, so all automotive designers should consider the aerodynamic principles more intensively when designing commercial vehicles, especially now with the continuously increasing petrol prices and demand for lower carbon pollution.

In terms of high ride quality, this is achieved by low noise levels reaching the passenger's ears. Air after contacting the vehicle's body at high speeds becomes turbulent and creates vortices with varying pressure contours. Vortices are swirling fluids with low pressure and could contain void volumes. The vortices emit sound directly and indirectly by exciting nearby objects causing them to vibrate and emit sound. The lower the noise level and frequency reaching the occupants the higher the ride quality and comfort. To illustrate, low aerodynamic forces do not necessarily correlate to lower acoustics generation. Therefore, researchers consider lowering the noise generated from exterior vehicle parts that are close to occupants' ears by changing the design and shape of the studied part. Therefore, the streamlined flow and the generation of noise should also be considered, as this determines the quality of the ride and comfort, especially in high-end

luxury cars where the high-class consumers look for a seamless driving experience and the lowest disturbance possible.

1.2 Statement of the problem

The automotive industry is believed to have reached its peak with an increasing price of a new car, as the population in the developed markets is going past their car buying prime years and new markets are rare. Due to this issue, each manufacturer is currently aiming for high returns and a bigger market share. As car sales in wealthier regions tumble and the delay in developing markets, the automakers are worried things are not going as expected. Due to the high competitiveness of the automotive industry, this resulted in high demand for research and development in all aspects of the vehicle. Each automotive company research ways of improving the aerodynamics and aeroacoustics properties of either part or section of the vehicle.

Noise from air sources is transmitted through different paths/regions of the structure; it could travel through leaks in sealings and openings. Although vehicles have sound absorption packages to reduce interior sound, they can only handle a range of frequencies or amplitude, and they are heavy to add freely to a vehicle. A vehicle has many wind noise sources that create a fluctuating surface pressure that creates forces resulting in drag and noise. The main contributors to the driver's noise hearing are the A-pillar and side mirrors closest to the driver (Figure 1). The wake structure is generated to create a low-pressure zone that vibrates the surrounding structure creating noise that affects the ride quality.

The vehicle's side mirrors are one of the most important contributions to the wind noise. R.H. Barnard stated, "from a performance point of view, the contribution of a generic side mirror to total drag of a car is around 3-6%" is mentioned by (Bernard, 2010). Furthermore, the side

mirrors contribute greatly to noise generation when in contact with high speed airflow and generate sound up to 130 decibels of sound pressure level in a range of 0 to 1000 hertz frequency as presented by (Belamri et al., 2007).

In terms of noise sources coming from the vehicle, there is another vehicle part that is responsible for noise emission outside the vehicle. The exhaust system does not just affect the occupants but nearby pedestrians and locals. In terms of the exhaust pipe, the acoustics can be handled by placing a muffler and not much optimization can be done. However, the aerodynamic effect of the position of the exhaust pipe on the entire vehicle is to be studied and the optimum position for either the lowest drag and/or lift coefficient is concluded and discussed.

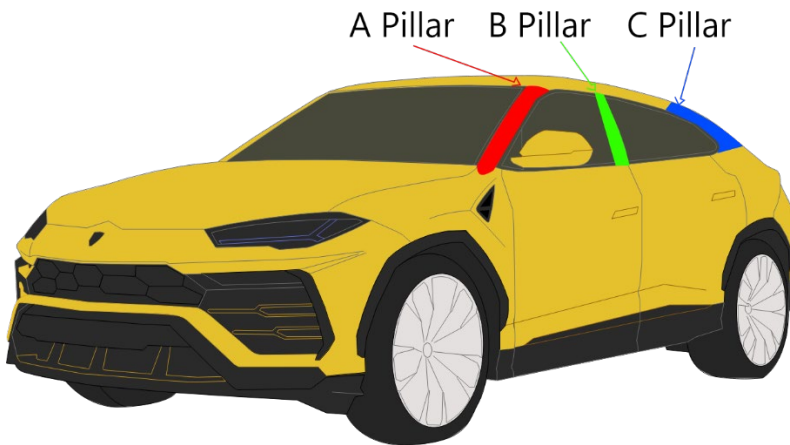


Figure 1: The vehicle has 3 pillars, A (red), B (green), and C (blue).

1.3 Research objectives

The main objective of this thesis is to improve the vehicle's AD & AA performance by modifying the shape and/or design parameters of any part of a section of the vehicle. Furthermore, other operating conditions are simulated to improve the aerodynamic properties. This thesis presents a

detailed literature review to summarise previous work on the AD & AA and the methods available numerically to simulate the optimization. Also, the work presented mentions the latest optimum shape/design for a part/section that improves the AD & AA performance. Furthermore, the thesis sets guidelines for which numerical setup to follow while simulating AD & AA problems. Lastly, the thesis studies which position for the rear exhaust pipe to be placed at that results lowest aerodynamic forces values.

The side mirror has a significant contribution in both the vehicle's aerodynamic forces and aeroacoustics, so research is needed to find a solution to reduce either or both properties. Removing the side mirrors will reduce aerodynamic forces and acoustics generated by it. However, due to regulations in the USA, manufacturing companies cannot remove them, so the only option is to improve the shape and design. The mirror is studied extensively in the literature, and different shapes are suggested to output the least AD & AA values. However, the literature lacks studies about the part linking the mirror to the body; the side mirror base. Therefore, the thesis aims to study the effect of changing the side mirror's base on AD & AA. Then determine which design parameter of the mirror base outputs the least aerodynamic forces and/or acoustics generation.

Another important noise source is the exhaust system. The exhaust pipe noise reaches both occupants and nearby pedestrians and could cause hearing problems if used for a long time. However, exhaust pipe noise could be solved simply by adding a muffler to reduce the noise. Therefore, this thesis mainly focuses on the aerodynamic forces aspect of the exhaust pipe where different positions are tested to measure the effect on drag and lift coefficient while the exhaust pipe is outputting gas at a specific mass flow rate.

1.4 Relevant literature

Due to the current heavy legislation laws, automobile companies are forced to lower fuel consumption and reduce vehicle emissions as mentioned by (Löfdahl, 2005). Drag coefficient got introduced in America in the twenty century Ford and GM, and Chrysler entered a joint venture to produce an efficient vehicle in 1993, and they succeeded with the most efficient petrol consumption car up to date in 2000 with GM making a Vehicle with 0.163 drag coefficient (Cd) value. For this to be possible, GM removed wing mirrors and replaced them with sensors, removed door handles, covered rear wheels, placed flat plate underbody to cover the protrusions, made a duct from front to back to reduce stagnation at the front and fill the wake region, and a gradual taper at the back. In 1934 the car with the least drag coefficient in history got produced (the Tetra T77) with a Cd of 0.21. Recently, LucidAir, an Electric Vehicle car manufacturer, announced their first vehicle with Cd of 0.21, resulting in a higher electricity consumption efficiency with longer distances according to (Lucidmotors, 2020). The least aerodynamic shape in the world is a Teardrop or a water drop, with Cd of 0.04, but it is an impractical shape for automobiles, so half teardrop shape is the next best option Cd of 0.09. An example of bad drag coefficient is 2.1 for a cube, as this is considered a very large value. Figure 2 shows examples of drag coefficient value for two vehicles and full and half water droplet.

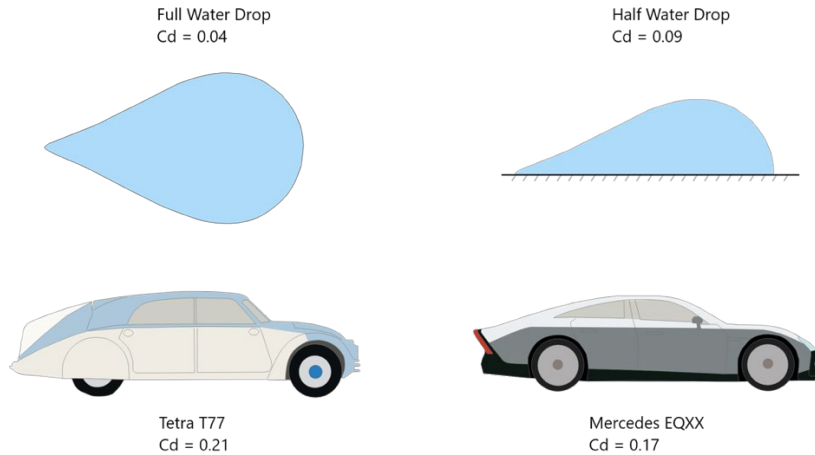


Figure 2: Drag coefficient for different shapes and vehicles.

While aerodynamics affects fuel efficiency, aeroacoustics affects the ride quality. Aeroacoustics studies noise generation by either turbulent flow or aerodynamic forces interacting the surface of the body.

Cities are full of economic opportunities and business activities. However, this development of transport and industry results in loud noise levels, and citizens suffer from noise pollution. Noise pollution causes problems ranging from communication interference and insomnia to deafness and mental breakdown, and for sensitive people could affect memory and raise blood pressure according to (Stansfeld & Matheson, 2003). Although the citizens need to be educated about the general cause of noise pollution and the possible effects as advised by (Goines & Hagler, 2007), and (Maisonneuve et al., 2009), respectively. The authors (Goines & Hagler, 2007) and (Maisonneuve et al., 2009) believe educating the public could lead to preventive measures—for example, wearing noise-cancelling headphones, which are popular nowadays. Government interference is required by setting regulations on vehicle noise and working time of construction. Recognizing this as a prime issue, the European Commission embraced new rules in (Of

& European, 2017) demanding major cities establish a noise management policy, as the (Parliament & Union, 2001) issued similar rules in 2001. Furthermore, the government of Turkey planted trees between the roads to reduce pollution and noise. Although noise is becoming more and more of a problem, it is not regarded as pollution.

Automobiles are a significant source of noise pollution, affecting both the occupants and pedestrians as discussed by (Singh & Davar, 2004). A scale of items emitting noise measured in sound pressure level (SPL) in decibels (dB) is shown in Figure 3. Therefore, the noise generation of the vehicle must be reduced by changing the exterior shape and improving aeroacoustics and possible aerodynamics.

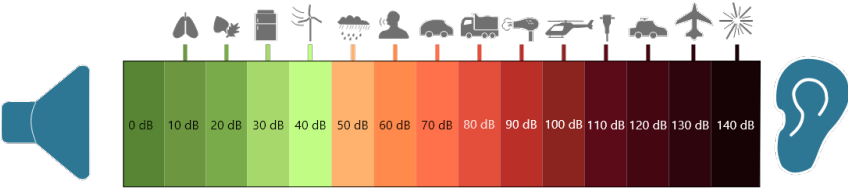


Figure 3: Noise scale for SPL in dB.

To improve vehicles fuel efficiency and ride quality, both aerodynamic and aeroacoustics design should be taken into consideration. Where an improvement on the exterior design should be made to make the vehicle smoother for air to travel around and not be disturbed or separation of flow will occur. Therefore, research is needed on each vehicle body or section to test the optimum shape, angle, orientation, dimensions, or geometry that results in lowest drag coefficient, and least wind separation. Vehicle tests are very important, and the core of all engineering work (concept, testing, validation). However, to test vehicle performance on roads a wind tunnel is used to represent road conditions, since test vehicles are usually incomplete, and parts could break or fall in real world testing, and this could be dangerous

to other drivers and unsafe for testers. However, wind tunnel is very expensive, as it costs \$15-30 million dollars to build, and \$2,000-3,000 to rent per hour. Therefore, computational fluid dynamics (CFD) simulation is used, as it represents a cost and time effective solution to wind tunnel testing, and in recent years the CFD mathematical models are improved to represent real life results as accurately as possible.

The automotive field is very broad and combines many scientific fields in a vast spectrum of knowledge and studies, ranging from sawing cotton to make passenger chairs to designing and programming microchips in the vehicle's computer. Therefore, a review of automotive exterior design in terms of aerodynamics and aeroacoustics must be split into sections, so this thesis is organised into sections, with each section focusing on a specific vehicle part or area. This section will be split into multiple sub-sections covering the different sections of design, and since currently numerical methods are used to output data, a section will concern a summary of articles that used numerical analysis and which method they used and its advantages and disadvantages. The review covers the mirror, and exhaust parts and in terms of background knowledge the numerical setup for previous work is mentioned and summarized in tables.

The lower the drag coefficient the less energy is needed for a vehicle to spend to travel, this correlates to less fuel spent and less harmful gasses are emitted to the environment. Due to environmental issues and new strict regulations, exhaust emissions and fuel consumption in vehicles need improvements to reduce the negative impact on the environment. A minor reduction in drag force is helpful and has a noticeable impact because of the many vehicles in the world; any small change will accumulate. Drag force acts on vehicles in the opposite direction to influence fuel consumption as

mentioned by (Kshirsagar & Chopade, 2018); therefore, a decrease in drag tends to decrease emissions and lower fuel consumption.



Figure 4: Different sections of a vehicle, front (light blue), side (dark blue), back (purple), and wheels (orange).

1.4.1 Looks versus practicality

A question might be asked of why automotive companies don't aim for least drag coefficient design with the highest fuel efficiency. This is explained by the looks versus practicality issue, where the consumers desire vehicles with attractive aesthetics than high efficiency. This problem is noticed in the Precept vehicle created by GM in the 2000, where even though it had 108 miles per gallon mileage it was considered unattractive and undesired by consumers. The battle between looks and practicality is the reason the car industry is inefficient, and to understand this issue, the psychology of looks and their meaning for humans must be explained. The human tendency of animism and anthropomorphism, i.e. interpreting even the non-living as living and in human terms, has long been noticed by (Lorenz, 1943). Humans subconsciously scan for faces in anything as a defensive instinct against predators, e.g. a stone as a bear as illustrated by (Haselton & Nettle, 2006).

Authors (Haselton & Buss, 2000) explained that people compare human faces with car features, like eyes with headlights, nose, and mouth with grille, and ears with side mirrors. Sports cars designers usually add a

wide grille angling downwards to simulate an angry man's face. Moreover, a social study done by (Windhager et al., 2010) is conducted to determine if people regarded vehicle headlights same as human eyes, by observing their point of focus when observing a vehicle, and the outcome shows the number of fixations is most significant on the headlights in every condition. Car face recognition is the main problem in the industry, as car designers make cars that display a certain look each for a purpose. For example, a sports car as mentioned will have a huge grille to give an aggressive look, and luxury cars are designed to be big and very odd inside profile shapes to represent uniqueness and attract attention.

1.4.2 Aeroacoustics

Both aerodynamic and aeroacoustics affect the in-car cabin wind noise. Therefore, to improve the overall vehicle efficiency and ride comfort performance both properties should be taken into consideration. In terms of determining the aerodynamic and aeroacoustics properties, either experimental or numerical modelling should be made. Since the work done in this thesis is done numerically the main focus would be a review of articles concerning numerical representation of aero properties. A direct noise computation code can solve the full compressible three-dimensional Navier-Stokes equations, as the model presented by (Van Herpe et al., 2011). Real-time boundary layer synthesis appears to be only feasible in the low-frequency range as shown by (Maury et al., 2012). Work done by (Maxit & Denis, 2013) explains the interaction between stiffened structures and TBL, as the resulted boundary layer from turbulent flows creates vibration on the object resulting noise emission, and a numerical model is presented. The rear end is identified as the main drag force contributor, then comes the back and front wheels, and lastly the side mirrors as concluded by (Rüttgers et al.,

2019). Therefore, in terms of volume to effect ratio the side mirrors are the main contributor to drag force.

In terms of aeroacoustics there are different ways of reducing the noise. For example, a method of reducing emitted noise is creating a porous cavity flows on a surface can reduce noise considerably in the centreline of the cavity floor and the near field. A cavity can be added to the surface of the vehicle for better aeroacoustics performance but will appear strange in my opinion. The noise control reaches optimum when porosity is 11.2%, where the maximum noise reduction is bigger than 10 dB. However, increasing the porosity from 11.2% to 19.27% reduces the noise control effect as shown by (Li et al., 2020) and it has been proven experimentally by the author. The noise is most significant for the wall-mounted cube along the lateral direction. An experimental validation is done by (Wang et al., 2019) to prove that increasing the distance from the wall increases the radiated sound in the vertical direction and peaks at one-quarter of its side length above the ground. Furthermore, research done by (Wang et al., 2019) provides an important guidelines for automotive designers that aim for noise reduction, as this can be applied on the mirror and set the spacing between it and the vehicle's body.

Research published by SAE discusses all physical phenomena involved in SPL generation and the available methods for characterizing wind noise sources while stating the advantages and disadvantages of each approach as discussed by (Blanchet et al., 2014). The five physical phenomena are as follows: pressure fluctuations of the side mirror, side glass, and A-pillar, the acoustic sources within eddies, and the pressure fluctuations of the side glass-outward effect. An interested researcher is advised to read (Blanchet et al., 2014) article for the available methods.

1.4.2.1 Noise source and path

Besides squeaks, rattles, and tizzes occurring inside the passenger compartment, noise or vibration usually originates outside, somehow interacting with the vehicle structure and then producing radiated sound inside the passenger compartment. Noise generation from the side mirror to the passenger's ears are shown in Figure 5. A higher level of noise is considered very discomforting to humans as discussed by (Huang et al., 1988). There are two possible paths for noise; an airborne and a structure-borne noise path. Airborne noise from outside the compartment that leaks inside is called airborne noise path. Furthermore, a structure-borne noise path is outside vibrations that cause passenger compartment surfaces to vibrate and radiate noise as mentioned by (Harrison, 2004). At higher frequencies, noise received via airborne noise paths is the main contributor to interior noise levels. Even at lower frequencies, airborne noise remains a significant contributor to overall noise levels, especially if the passenger compartment is not properly sealed. Sound absorbing material can reduce noise levels inside the passenger compartment, adding weight to the car. Sound absorbing material (SAM) can absorb noise in a specific frequency range at some distance from the source, but the effect is small as (Harrison, 2004) concluded.

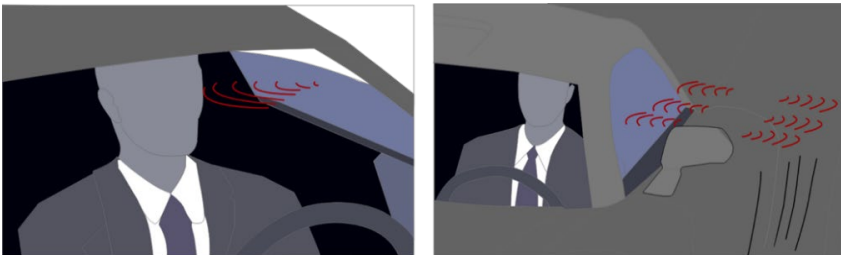


Figure 5: Noise generation from side mirror to passenger's ears.

1.4.2.2 Noise transmission

For sound to reach the driver or passenger it first starts as air fluctuating at the exterior which creates different pressure contours a high and a low-pressure zone. This change in pressure values creates a force in the direction of the lowest. The force resulting from pressure fluctuations vibrates the car body, and in a weak area like glass it has a high effect, then the structure passes these vibrations into the interior air which then reaches the occupant's ear as illustrated by (Bremner et al., 2003) and shown in Figure 6. In order to simulate noise level inside the vehicle a aero-vibro-acoustic model is pursued where three steps are followed in simulation. Firstly, the vehicle is subjected to external air flow and eddies and pressure fluctuations are recorded. Secondly, structure simulation is carried out to observe the effect of pressure fluctuations on the solid structure of the vehicle. Lastly, the inner medium of the vehicle is studied with the structure (side glass) taken as a sound source, due to its vibration (Figure 6). This process is simulated in ANSYS fluent CFD simulation and a structural simulation and is called aero-vibro-acoustics, that has been modelled by (Bremner & Wilby, 2002). The difference between high and low SPL inside the vehicle determines the level of luxury it provides, this is why luxury car manufacturers care so much about cabin noise and aim to reduce it to a minimum in any way possible, either by adding insulating materials or implementing sound-cancelling features into the interior sound speakers. However, luxury brands mention that their aim is not an absolutely quiet ride, as their research shows that extremely low SPL makes occupants feel nauseous and dizzy, that is why they set a limit to the minimum SPL to be reached to result in maximum ride comfort.

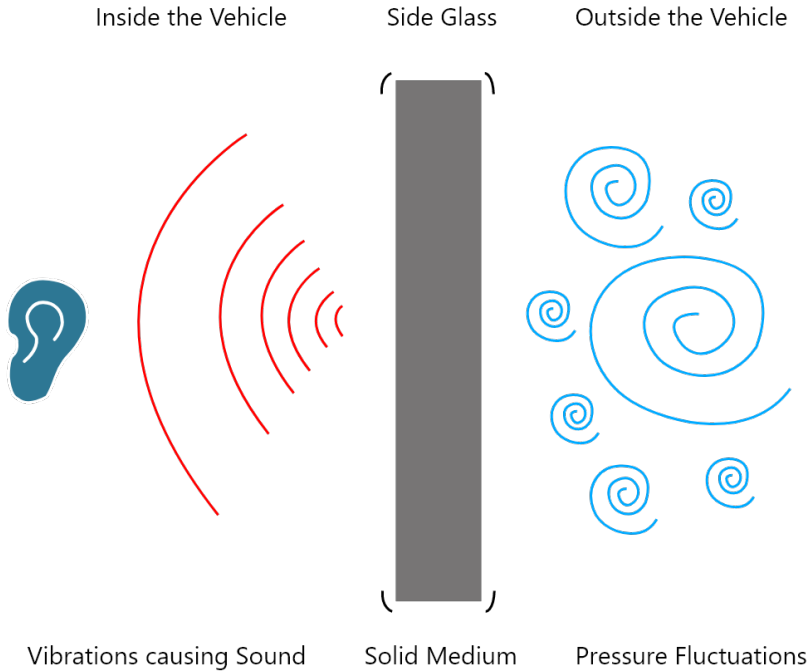


Figure 6: Aero-Vibro-Acoustics model of how vortices outside the vehicle, translate into interior noise.

1.4.3 Vehicle side mirror

The side view mirror contributes greatly to wind noise and drag coefficient (Bernard, 2010). The base of the mirror which connects it to the vehicle's body is an important part in terms of both aerodynamic and aeroacoustics interference on the vehicle and shouldn't be neglected. Furthermore, (Ehlert et al., 2018) determined door-mounted mirrors to be better than sail-mounted mirrors and tested several mirror shapes to determine the most efficient of them in reducing the aerodynamic forces and noise emitted. This outcome was also validated by (Zaareer & Mourad, 2021) where two mirror positions are tested. The base of the mirror placed horizontally (0 degrees) or midway (45 degrees) shows no change in aerodynamic forces, but an aeroacoustics effect, with the midway angle

having lower wind noise output than horizontally placed as mentioned by (Zaareer & Mourad, 2021), where the acoustics are generated aerodynamically. This concept is also mentioned by (Lighthill, 1952).

The closer the mirror's incline to the mounting plate, the lower the emitted noise in both vertical and lateral directions of the wake, and the bigger the mirror's aspect ratio the more noise generated as explained by (Chode et al., 2021). Also (Wang et al., 2020) conducted a similar test and outputted similar conclusion. A 7.3 dB noise reduction is achieved by (Ye et al., 2021) where the authors added a bionic shark fin on the side mirror, the bionic shark fin reduces noise by creating vortices that cling to the surface, decreasing the negative pressure area. A bionic blade can reduce up to 3 dB of generated noise as mentioned by (Liu et al., 2021). Mirror distance placement from the vehicle body has an important wake structure effect, as the recirculation region behind the bluff body shrinks as the gap value increases, which increases the drag force behind the mirror as proven by (Nasif et al., 2019). The relationship between mirror shape and surface pressure and interior cabin noise is studied by (Peng, 2011) while explaining the effectiveness of the measurement method. Table 1 summarizes literature conducted on the side mirrors in terms of optimizing the aerodynamic performance, either by improving the shape, design, and/or addition of parts on the mirror.

Table 1: Summary of novel and innovative articles that concern airflow on side mirrors.

Author/s	Objective	Novelty According to The Author	Method Used	Variables Studied	Resulted Outcome
(Kim & Han, 2011)	Examine the wake structure created by rear-view mirrors	Studies and explains both the vortical and periodic structures	Experimental, hot wire anemometry and two-dimensional laser Doppler velocimetry	velocity fields in streamwise and cross-sectional planes	Reverse flow region at up to $x/d = 1.2$ distance from the mirror
(Yuan et al., 2020)	Finding the contribution of hydrodynamic and acoustic pressure	Other articles don't segregate between pressure sources where is the novelty	Experimental, CFAT method in AAWT	Variation of wind speed, yaw angle, and side mirror geometry	Although much smaller in value the acoustic pressure is the main interior sound pressure source
(Kim et al., 2021)	Sound pressure level analysis	AI-based technique is utilized for fluid dynamic research	Experimental and numerical, Using 4D PTV and ANFIS Method	3 different mirror models with different shapes	ANFIS is an accurate representation of experiments
(Yao & Davidson, 2018)	Simulation of inside noise generation from flow around the mirror	Explores the physical mechanisms of interior noise generation	Numerical, LES model with FW-H	Wavenumber-frequency spectra are examined	Exterior acoustic pressure is the main inside noise source
(Yao et al., 2017)	Noise generated by low to high Reynolds number flow over the hemisphere	The surface correction method is used to remove contamination	Numerical, LES model with FW-H	SPL, PSD, streamlines and contours, aerodynamic forces	Transformation of the structure due to change in Reynolds numbers is examined
(Mahato et al., 2020)	An arrangement for reducing SPL for square cylinder	Uses DNS from the solution of the Navier stokes equation	Numerical, high computation demanding DNS	Drag and lift coefficients, Strouhal number	The proposed arrangement of cylinder and cowl reduces around 24 dB SPL

Table 1: Summary of novel and innovative articles that concern airflow on side mirrors (continued).

Author/s	Objective	Novelty According to The Author	Method Used	Variables Studied	Resulted Outcome
(Ask & Davidson, 2005)	Predict flow field and emitted sound past side mirror	Volume sources are neglected, only fluctuating wall pressure and time derivative are considered	Numerical, Ffowcs-Williams Hawkings	SPL and frequency, PL and frequency, aerodynamic drag	Good agreement between numerical and experimental up to 100 Hz
(Hartmann et al., 2012)	Wind noise caused by side mirrors and A-pillar	Extensive resources are used to compare experimental and numerical results	Experimentation in the wind tunnel, and numerical CFD analysis	SPL, ranging flow velocities from 80 to 200 Km/h	Agreement between numerical and experimental show acoustic pressure is the main noise contributor
(Watkins & Oswald, 1999)	Exterior Flow field on side mirrors	Document the local flow field of exterior mirrors	Wind tunnel and on-road testing	Vehicle yaw angle, SPL, and frequencies	Agreement between on-road and wind tunnel testing

1.4.4 Airflow numerical models

Numerically there are multiple models that are available for fluid flow representation. However, not all yield accurate results, or some output correct results at a huge computational cost. Therefore, a review of previous articles concerning the fluid flow, which outputs aerodynamic forces data and/or acoustics is needed. The summary is used as a guide for optimum turbulence model to use in each specific case (Table 2).

Table 2: Summary of simulation methods used to represent airflow.

Author/S	Objective	Comparison Between	Superior	Area Of Excellence	Limitation Of the Better Method	Disadvantages of the Worse Method
(Spalart, 2000)	Clarify the maximum level possible for numerical prediction of Turbulent flow	Reynolds Averaged Navier Stokes and Large Eddy Simulation	LES	Simulating Boundary Layer separation	Geometry dependent eddies are discarded by an averaging process	Unable to simulate flow separation at large Reynolds numbers
(Shur et al., 1999)	Simulate separated flow at high Reynolds numbers	Large Eddy Simulation and Detached Eddy Simulation	Detached Eddy Simulation	Simulating flow separation of Reynolds numbers above 10^5	High cost and processing time	Poor results and high error in high values of Reynolds number
(Travin et al., 2000)	Testing model differences for Laminar and Turbulent Separation	Unsteady Reynolds Averaged Navier Stokes and Detached Eddy Simulation	DES for Laminar Separation, and URANS for Turbulent Separation	Similar results to experimental for Turbulent Separation	Inaccurate Laminar Separation simulation	Inaccurate Laminar Separation simulation
(Ask & Davidson, 2006)	Turbulence model to complement Ffowcs-Williams sound model	DES and LES	DES	More dissipative and reduces pollution of numerical noise	Inaccurate wall pressure fluctuations	Unresolved fluctuations are treated in the acoustic surface integration
(Strelets, 2001)	Providing a comprehensive review of DES	DES and RANS	DES is superior	DES is considered excellent for massively separated turbulent flows	Transition prediction and Transition control within the turbulence model	Requires expensive computing power
(Vatsa & Singer, 2003)	Testing the credibility of TLNS simulation code	2 and 3D analysis for URANS and DES	DES	DES computed pressure agrees with experimental results for 2 and 3D	Appropriate grid resolution and time step should be chosen to work	The solution is unreliable and erroneous
(Schmidt & Thiele, 2003)	Simulation of flow around an airfoil	DES and RANS	DES	Resolves unsteady flow features	High computation time	Only for steady flows as it dampens transient motion
(Constantinescu & Squires, 2000)	Prediction and investigation of flow around a sphere	DES and LES	Results are similar as DES is a derivative of LES	Accurately predicted boundary layer separation with the transition to turbulence occurring downstream	Other settings play an important part	Other settings play an important part

Table 2: Summary of simulation methods used to represent airflow (Continued).

Author/S	Objective	Comparison Between	Superior	Area Of Excellence	Limitation Of the Better Method	Disadvantages of the Worse Method
(Constantinescu & Squires, 2004)	Investigation of flow around the sphere in subcritical and supercritical regimes	Subcritical and Supercritical DES representation	DES predicted the subcritical more accurately than supercritical	Able to capture large scale shedding	NA	Unable to predict the skin coefficient in the fully turbulent case
(Aljure et al., 2018)	Investigation around DrivAer model	LES and WMLES	WMLES	70% less CPU time	Unclear results where large pressure drops	High computational time
(Menter, 1992)	Navier-Stokes computation for flat-plate boundary layer	$k - \epsilon$ and $k - \omega$	$k - \omega$ (Wilcox, 1988)	No damping functions in the viscous sublayer	Very dependent on the ω freestream value (Modified by J.C. Kok (Kok, 2000))	Not precise numerical results (Modified by Wilcox (Wilcox, 2008))
(Ask & Davidson, 2009)	Study of flow past mirror with different turbulence models	DES, SGS, and dynamic Smagorinsky model	Simple SGS	Captures laminar separation and point of transition between laminar and turbulent BL	NA	DES suffers from pressure fluctuations, Dynamic SGS have oscillations
(Chaouat, 2017)	Model for simulating turbulent flows	LES, RANS, Hybrid RANS/LES models	Hybrid RANS/LES models	Reduces the computational time and memory	Moves the cutoff wavenumber earlier to the inertial zone of the energy spectrum	LES and RANS models are inaccurate and require expensive computational time

1.4.5 Mesh analysis

To conduct any simulation a mesh is applied to the geometry, and the more the elements added the higher the accuracy and time required by the simulation process. Therefore, researchers conduct a trial-and-error process in numerical simulation where different sizes of mesh are applied starting from large to smaller, and the results are examined for convergence. It is easier and more efficient to use unstructured mesh than a structured conforming mesh. However, the central differencing scheme for polyhedral cells has more suitable kinetic energy conservation properties than non-conforming tetrahedral cells as shown by (Afgan et al., 2008), where energy

conservation properties are better in polyhedral cells than in tetrahedral cells. Table 3 summarizes the literature on different sections of the vehicle that compares between mesh types or sizes.

Table 3: Review of articles on other sections of the vehicle.

Author/s	Objective	Comparison Between	Best Choice	Worst Choice	Disadvantages of the Worse Method
(Siegert et al., 1999), (Höld et al., 1999)	Best grid resolutions	Fine, medium, and coarse grid solution	Fine grid solution	Coarse grid solution	Unable to give an accurate representation of the surface pressure distribution
(Ask & Davidson, 2009)	Study of flow past mirror with different advection schemes	Second-order upwind scheme and monotonic central scheme	Little to no effect of change as long as the DES model is avoided	NA	NA
(Ask & Davidson, 2009)	Study of flow past mirror with different grids	Primary grid, second grid with significantly higher resolution, and lower front resolution	First and second grids	Low front resolution	Fails to predict the separation point at the front of the mirror

In simulation, there are different types of mesh, also there is a constant mesh and a dynamic mesh. A moving mesh is studied in a four-wheel model with different openings, a closed rim, an open generic rim, an Audi Q5 rim, and a DrivAer rim to test the feasibility of the sliding mesh method (SMM). The sliding mesh method testing showed that the method is subject to convergence problems for locally reduced cell Peclet Numbers. These can occur when mesh movement causes cells to move along the oncoming flow

locally. However, using multiple pressure and velocity correction loops in each time step can converge the solution but increase computational effort. For example, the merged SIMPLE and PISO solution algorithm (PIMPLE) presented by (Haag et al., 2017). In numerical setup, (Ferziger et al., 1997) showed that the SIMPLE algorithm is regarded for Steady flows, and (Jasak, 1996) proved that PISO is regarded for Transient flow. An in-depth study by (Dong et al., 2014) based on the viewpoint of multiparticle interaction shows the effect of drag on a particle and a present expression for the computed drag force.

1.4.6 Rear exhaust effect on aerodynamics

In terms of aerodynamics, Soares (2015) is an excellent automotive engineer who studied the effect of exhaust position on a 3D model, where 10 different positions were studied with two different orientation of a semi-rectangular shape exhaust pipe. As in the first orientation the pipe is placed horizontally in 9 different positions, then in the last position the pipe is placed vertically. The different positions studied are in a 2D grid representation at the rear of the vehicle shown in Figure 7. The resulted from Renan's thesis showed that the closer the exhaust pipes to the bottom centre of the vehicle, the lower the drag coefficient (Figure 7). Although, there was a change in drag coefficient results, the overall effect is small, with a total change of ~1% when the lowest Cd value is compared to the highest.

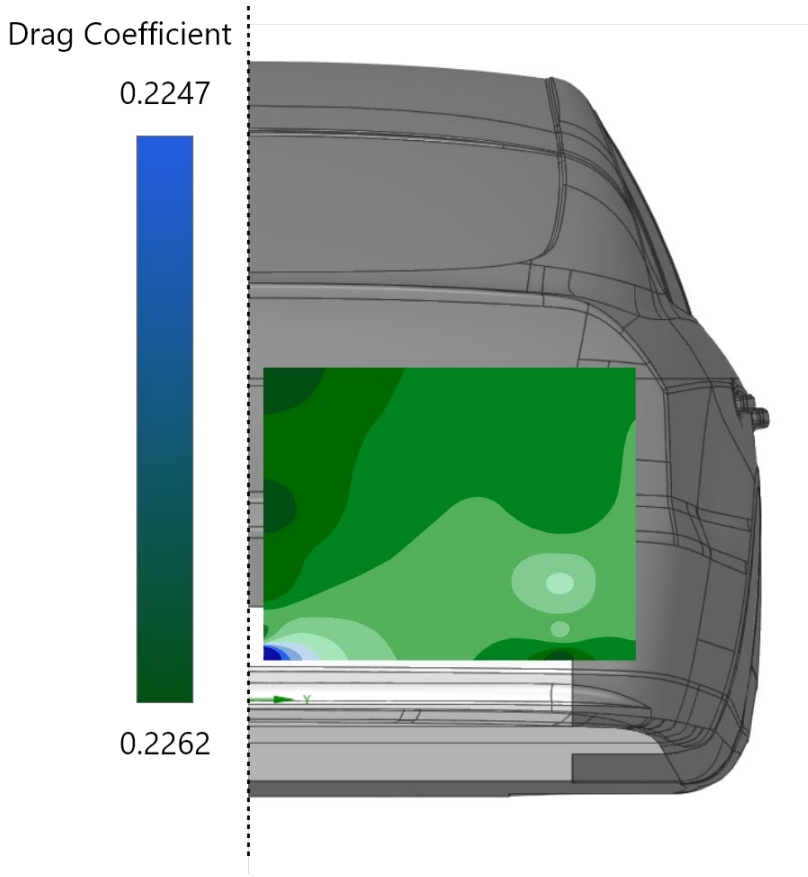


Figure 7: Drag coefficient variation when exhaust pipe placed at different positions.

1.5 Structure of the thesis

The thesis consists of 4 chapters, discussing 3 objectives. Firstly, an introduction to the side mirror base effect is done by studying the effect of changing the base orientation has on aerodynamics and aeroacoustics (Part 1). The second part continues first part's work with the objective of determining the optimum orientation for the base mirror that results lowest generated acoustics. Lastly, the second most important noise source is considered, the exhaust pipe, to simulate the effect of changing the exhaust

pipe position on the vehicle's aerodynamics. Chapters 2, 3, and 4 will include information on each part.

Chapter 1: The first chapter of the thesis introduces and discusses the topic, then the problem statement, then research objectives followed by a review of relevant literature, which builds the background of this work, and finally, the structure of the thesis is detailed.

Chapter 2: The second chapter discusses the design and CFD setup procedure conducted. The design of the model is discussed, and the methodology used in ANSYS fluent is shown with each parameter used, that are used to output the results.

Chapter 3: This chapter covers the results of the simulations of each of the cases as well as the post-processing analysis. This chapter also discusses the numerical results in relation to the existing experimental data.

Chapter 4: The last chapter concludes the thesis by listing the important findings of this work and discusses the possibilities of future work.

Chapter 2

Chapter 2: Methodology

This chapter covers the methodology, mathematical modeling, and experimentations employed for studying the problem statement mentioned in the previous chapter. Many factors or specifications need to consider when designing geometry for comparative study reasons. For example, in terms of the side mirror base study, the design is made to ensure the projected area remains the same and independent of the orientation of the base. Furthermore, in terms of the exhaust pipe modeling, the pipe is inserted into the DrivAer model rear section; therefore, a similar cut-off area is desired between different positions to ensure a fair comparison. In numerical design, the studied part is modeled, then an enclosure is created that surrounds the body, then the original body is cut off from the enclosure. By following this method, the numerical model could be presented.

2.1 Design and geometry

In order to conduct a simulation, firstly a specific geometry is designed to test specific parameters and isolate the other affecting parameters, in order to focus only on the desired parameter or effect. The isolation method is desired especially in terms of airflow representation where any part affects the flow of air and has a boundary layer separation around it. For example, in the side mirror simulation, the geometry is designed to exclude the A-pillar which has a significant effect on air flow and aerodynamics and aeroacoustics properties.

2.1.1 Side mirror base part 1 geometry design

The first part compares between two positions of the mirror base. Either placed horizontally or at an angle of 21.25 degrees as shown in Figure 8. The geometry is designed based on Toyota Camry 2016 model. Figure 8 shows the process of geometry design, where the vehicle's side body

dimensions are measured, then a CAD file is created. In part 1 of studying the effect of changing the mirror base, two orientations are studied as shown in Figure 8.

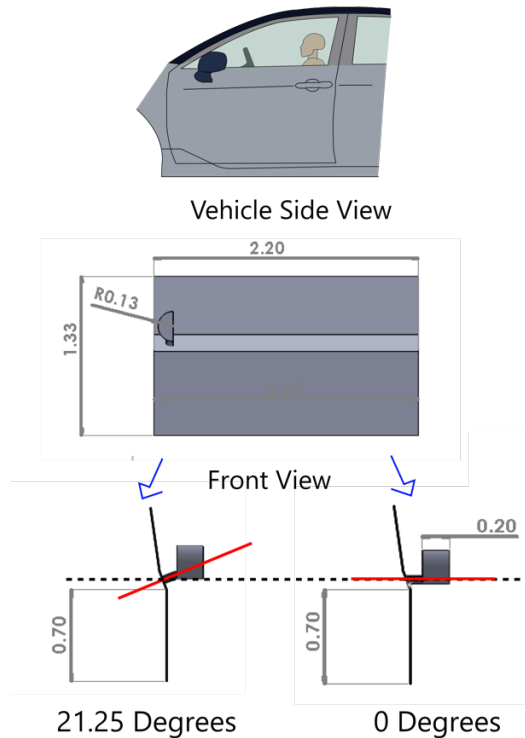


Figure 8: Geometry design process based on Camry model, taking two study cases with different angles, 21.25 degrees base mirror (left) and 0 degrees base mirror (right).

2.1.1.1 Fair comparison

To model this accurately, a fair comparison design and model is required. It is noticed that cars with mirrors placed on side panels tend to have sharp edge turn side profile (Figure 9, 12). Whereas cars with mirrors positioned horizontally on side windows tend to have almost a vertical profile. This slight angular curve might affect vehicle aerodynamics; then,

data will vastly differ. Therefore, for a fair comparison a car body suitable for both positionings is desired. So, the following profile has been suggested. It is an interpolation between both profiles that is suitable for either mirror base positioning. The side plate is only meant as a car side representation.

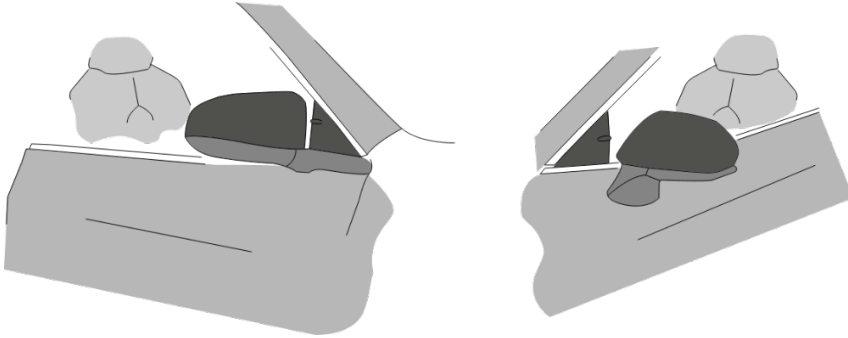


Figure 9: Horizontal base (left) & angular base (right).

2.1.1.2 Side mirror base part 1 geometry dimensions

A vehicle side geometry design is desired that can simulated for two mirror base angles by either placing the mirror base horizontally, or at an angle. The aim to find which position is better either aerodynamically, or to reduce noise generation. The Horizontal Position dimensions are shown in Figure 10, and the angular position geometry dimension is shown in Figure 11.

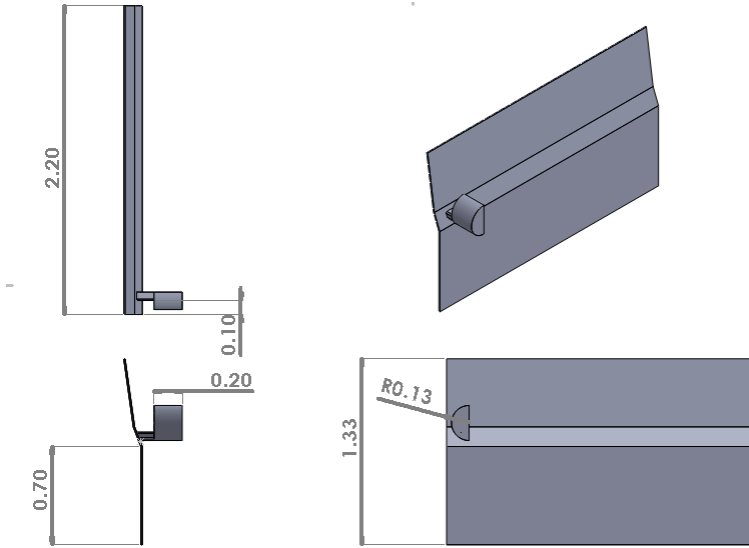


Figure 10: Horizontal base CAD geometry dimensions.

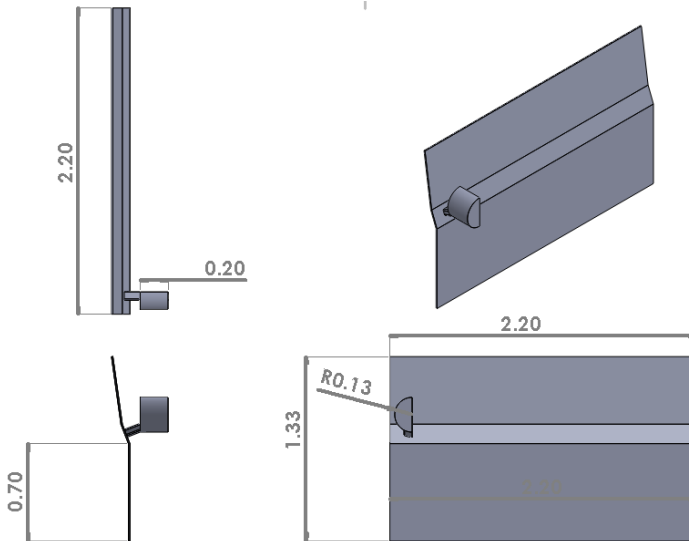


Figure 11: Angular base CAD geometry dimensions.

2.1.2 Side mirror base part 2 geometry design

In order to test mirror base placed at different angles from 0 to 90 a different design is needed that ensures a same projected area is kept at different orientation of the mirror base. This is achieved through a circle, where it has a constant radius and at every mirror base angle the dimensions of the base remains constant. In the pre-processing phase a design must be made that can provide fair comparison for all studied cases. The mirror base depends on the design of the rest of the vehicle, specifically the side of the car. As a more aerodynamic design requires vertically straight side cross section, an angularly placed mirror is not valid here, neither is a 90-degree mirror. As can be seen for the Rolls Royce, it has a wide start for the side where the mirrors are standing (Figure 12). In case of Mercedes Benz, the side is almost vertical, thus the mirror is placed horizontally (Figure 12).

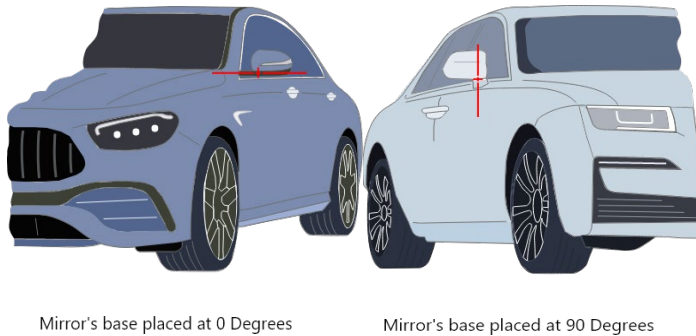


Figure 12: Horizontal mirror Mercedes-Benz (left) and vertical mirror Rolls Royce (right).

To make a fair comparison between angles, the projected area of each angle must be the same for different angles, otherwise the drag coefficient will differ, and this will add an undesired parameter. As the drag property depends on projected surface area. How the base can be fixed at several angles, is by making the vehicle's side a quarter of a circle. This design isolates the mirror to measure its effect without the interference of the A-pillar. So, the design has a quarter of a circle with radius of 0.2 m. On the corner of the mirror there will be half a circle to guide the base surface, with radius of 0.05 m. Figure 13 demonstrates an isometric view of the studied case taking an angle of 90 degrees as an example. Figure 14 shows the dimensions and reference axis for rotation that are used in this thesis.

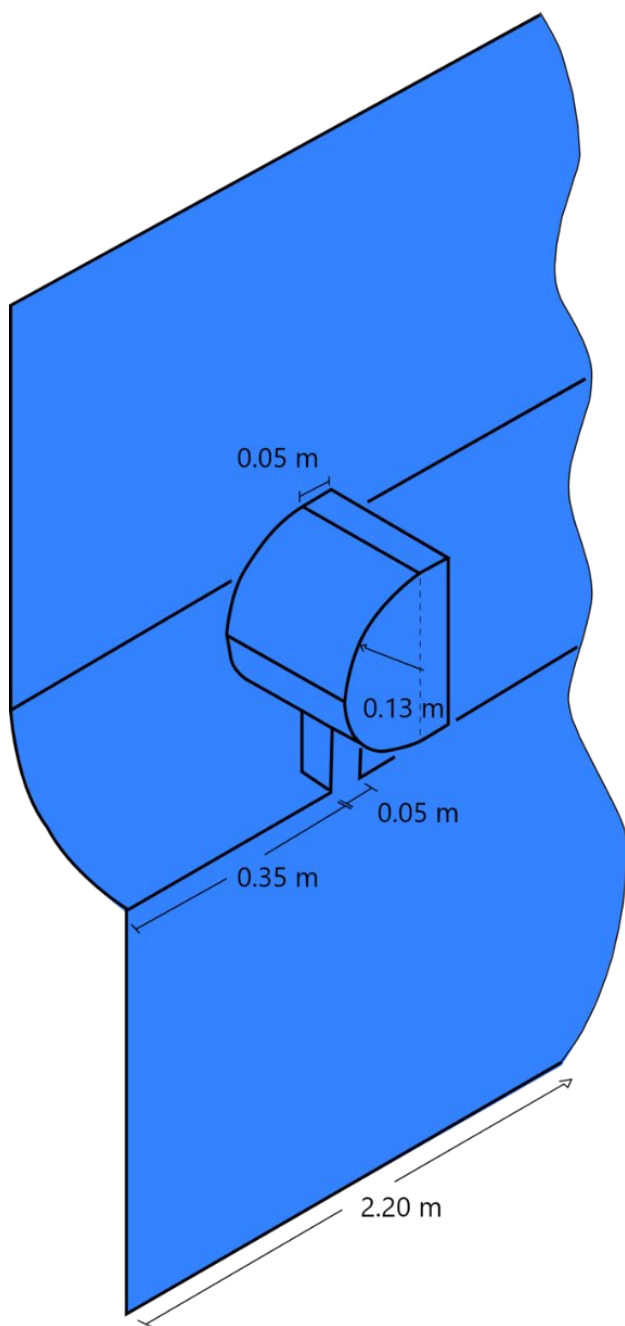


Figure 13: Isometric view for the case study.

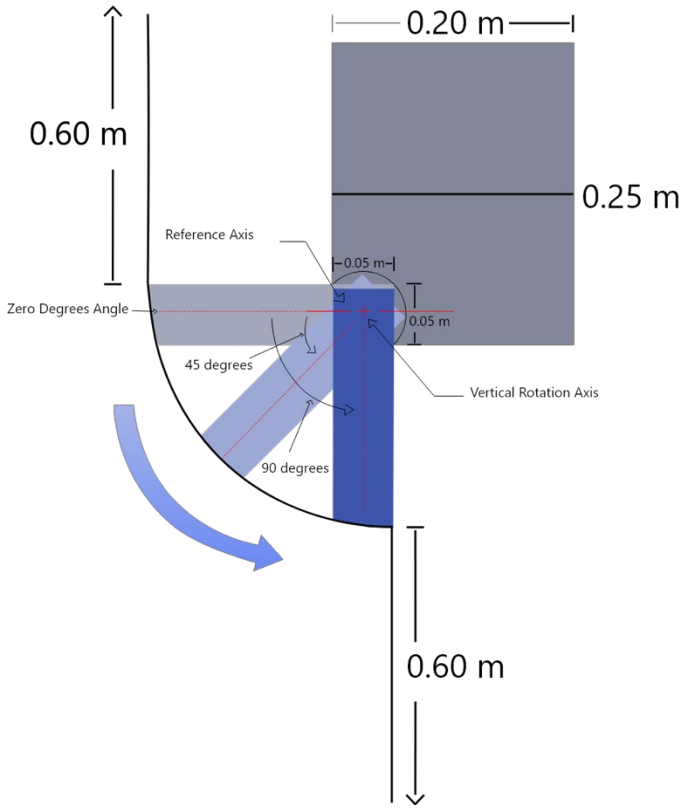


Figure 14: Front view of the investigated case study, with side mirror on the left and mirror part is in grey color, and the base is changing positions.

There are 26 cases examined in studying side mirror base part 2, each having an angle value for the mirror base, and the values for aeroacoustics and aerodynamic forces are obtained for each case. Angles examined are: 0, 11.25, 22.50, 33.75, 45, 50, 51.25, 52.50, 53.75, 55, 56.25, 57.50, 58.75, 60, 61.25, 67.50, 78.75, 80, 81.25, 82.50, 83.75, 85, 86.25, 87.50, 88.75, and 90. These angle values are chosen to cover a wide range of angles with two step sizes 11.25 and 1.25 degrees. At first 11.25-degree step is followed and the results are examined, and whenever there is a significant change in acoustics

or aerodynamic results a smaller step size is used around that angle of value of 1.25 degrees.

2.1.3 Vehicle rear exhaust geometry design

The rear exhaust pipe can be placed at different heights on the rear as shown in Figure 15, where usually sports cars have the exhaust placed at the top of the rear, or the most common position at the bottom. Figure 15 shows a sports car with exhaust at the top, and a sedan with exhaust at the bottom. An investigation of the effect of rear tail pipe height on aerodynamic forces is set. The aerodynamic forces are examined for a 2D DrivAer model where the exhaust pipe is placed at different heights relative to the ground, but on the vehicle's rear. The field of exhaust flow effect on aerodynamics has not been studied much. The objective is to estimate the magnitude of the drag and lift force variation at each position and result in a conclusion for the optimum height for the exhaust pipe to be placed at, in order to result the lowest aerodynamic forces.

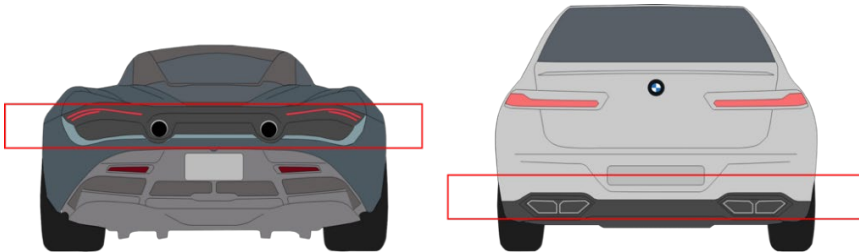


Figure 15: The exhaust pipe can be placed at different positions, either on the top of the vehicle like McLaren (left), or at the bottom of the rear like BMW (right).

In order to accurately represent wind tunnel experimentation in ANSYS fluent, similar dimensions should be included. Wind tunnels are huge compared to the allowed geometry of study, and this is due to blockage ratio

(especially in 2D cases simulation), as air needs large area to move while being distorted by the presence of a body. That's why the dimensions of the study area are important.

In airflow simulation an important property must be taken into consideration, which is the blockage effect. To illustrate, the air interacting with a body is displaced in different directions and needs available volume to flow in otherwise it could affect the results significantly. This is known as the blockage ratio:

$$\delta = \frac{A_{ref}}{(H_{wt}W_{wt})} \text{ for } 3D, \delta = \frac{H_{ref}}{H_{wt}} \text{ for } 2D \quad (2.1)$$

Where, A_{ref} represent the reference area, H_{ref} is the reference height, H_{wt} is the wind tunnel height, and W_{wt} is the wind tunnel width.

The studied area in ANSYS fluent for 2D simulation is designed as follows. The length of the ground is $12L_{ref}$, and height is $4.4L_{ref}$, the vehicle is positioned $2L_{ref}$ from the inlet, the distance between the car and ground is $0.065L_{ref}$. The geometry dimensions concluded from the calculations that results in no blockage in Equation 2.1 are shown in Figure 16. A wake structure is set around the DrivAer model, with specifying the surrounding values as shown in Figure 16.

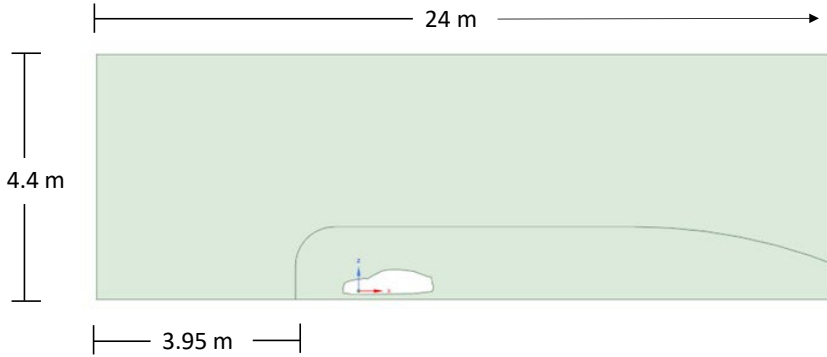


Figure 16: 2D DrivAer model validation and exhaust system study case.

2.1.3.1 Studied vehicle geometry

The popular and experimentally verified DrivAer model is utilized as experimental validation for the exhaust height effect study. The DrivAer fastback model is chosen in 2D simulation as it represents a time effective method with accurate results. The 2D simulation is like Fastback_woW_woM with no wheels and no mirrors, which resulted an experimental drag coefficient value of 0.125 as mentioned experimentally obtained by (Heft et al., 2012a). The effect of wheels and mirrors on aerodynamics is huge, with a difference of $\sim 45\%$ when compared to with and without mirrors and wheels as shown by (Heft et al., 2012a). Therefore, removing these components from the exhaust simulation isolates the effect of the exhaust flow at different heights, which allows for more concentration on the effect of moving the exhaust pipe on aerodynamic forces.

2.1.3.1.1 DrivAer model

Computational Fluid Dynamics has become a powerful tool in the car design process. Therefore, a simplified geometry is created for automotive aerodynamic research like the geometry proposed by (Ahmed, 1981) which was named after him. There are other car geometry models beside (Ahmed et

al., 1984), there is the SAE bodies by (Cogotti, 1998), and model by (Guilmineau, 2008). However, a more realistic model is needed for accurate aerodynamic research, so the DrivAer models are introduced by (Heft et al., 2012b). The models are designed with three different rear-end configurations (fastback, estate back, and notchback) with a choice of the smooth or detailed underbody. The DrivAer model (Figure 17) ever since introduced it has been constantly improved on and currently a fourth generation model is available as an more accessible open source in different formats done by (Soares et al., 2018). The fourth generation model is done by (Soares et al., 2018) and is both validated experimentally and numerically, it provides more vehicle parts (diffuser, rear wing, ventilation system) to study wider range of vehicle modifications to reduce acoustics and aerodynamic forces. The fourth gen model is 35% smaller than the original to provide lower computational cost.

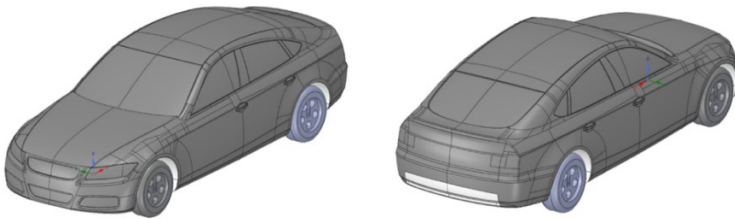


Figure 17: DrivAer model isometric view.

Since introduced the DrivAer model has been continuously improved to cover different parameters and factors, as the original DrivAer doesn't cover high performance car configurations. For example, the diffuser, spoilers, and splitter. Therefore, the 4th generation DrivAer model by (Soares et al., 2018) covers this gap and creates a much versatile and usable model in different formats. The model created by Soares et al. (2018) is available in STEP, STL, IGS, and X_B. Having the model in STEP format is much easier

to deal with, since ANSYS DesignModeler suffers from the highly precise surface mesh of an STL file. While DesignModeler is easier to sketch in, it is currently unusable in complicated geometry files, and this is where Spaceclaim shines, as it is able to deal with different formats and have many properties. The 4th generation DrivAer has different dimensions than the original, as it is scaled to a smaller format 35% (Figure 18).

In terms of verifying the exhaust simulation the DrivAer model experimental data is used. Since the simulation is in 2D and utilize the 2D DrivAer fastback model, a numerical simulation is performed to validate a 2D cross section of the model as is compared with experimental results to validate the exhaust pipe simulation.

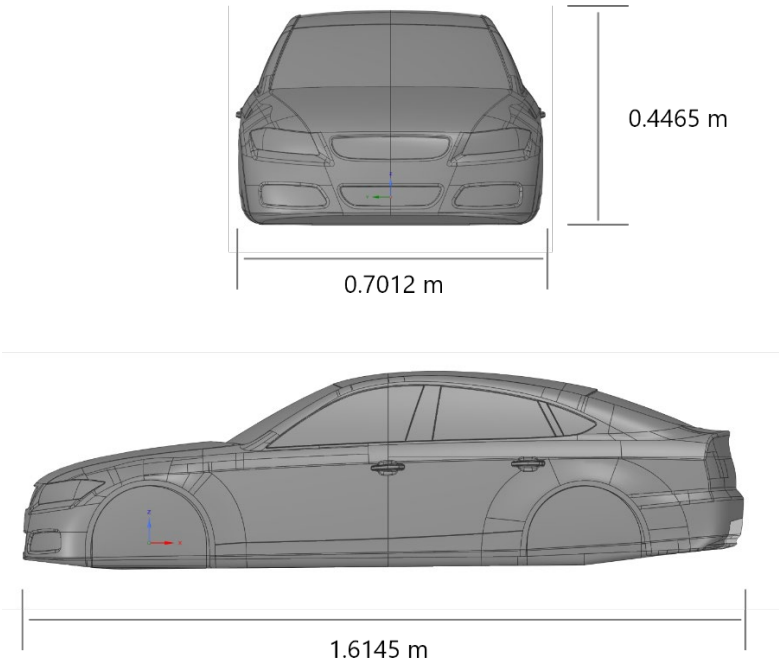


Figure 18: DrivAer model 35% scale dimensions from original model.

2.2 CFD analysis

In terms of CFD simulation, ANSYS Fluent is widely used in articles to determine either the aerodynamic or aeroacoustics effect on vehicles or parts of the vehicle. In ANSYS setup, the starting selection for the simulation to be done is whether the desired results are reached at a steady or transient time. CFD simulation has been proven efficient in simulating real experimental procedures as shown by (Bauskar et al., 2019), and previously by (Belamri et al., 2007). However, still an experimental data is needed to verify the results. Figure 19 shows the main elements of any CFD Analysis.

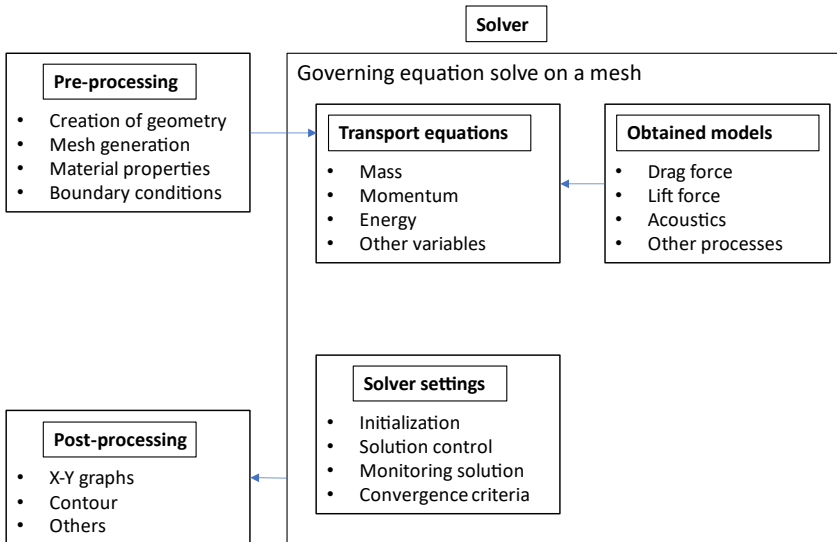


Figure 19: CFD analysis framework.

2.2.1 Material properties

In fluent the surface material has no effect when simulating airflow interaction with the object, as no-slip condition is applied. Also, the surface material roughness value has no effect on the results. The main properties needed in this simulation are density and viscosity of air where both are

implemented in Reynolds number equation and the drag and lift coefficient laws.

2.2.1.1 Side mirror base part 1 simulation airflow properties

At the first part in mirror base simulation, the default values of air properties is chosen in ANSYS. The values of air are as follows, density 1.225 Kg/m³ and a viscosity of 1.7894E-05 Kg/(m.s),

2.2.1.2 Side mirror base part 2 and vehicle rear exhaust simulation airflow properties

In the 2D model for exhaust pipe simulation and validation the air properties are set at 298 kelvin, this results a density of 1.18415 Kg/m³ and a viscosity of 1.86E-05 Kg/(m.s), and these values are similar to previous work pursued for verification. Table 4 shows the airflow properties used in both cases.

Table 4: Operating settings used for exhaust simulation.

Parameter	Value	Unit
Density	1.18415	kg/m ³
Viscosity	1.86E-05	Ns/m ²

2.2.2 Governing equations and model assumptions

There are multiple models used in this thesis depending on the case. For example, in ANSYS fluent when simulating a steady case model, usually k-omega is used to obtain aerodynamic forces. However, in transient solution, a more detailed model with higher computational accuracy is required like SAS to simulate the problem and obtain aerodynamic forces, SAS is paired with FFW in order to get acoustics results. Each model is explained, and the mathematical model presented, as well as famous models that are continuously applied in literature.

2.2.2.1 Aerodynamics forces model

Aerodynamic forces are very important for vehicles and there are two main parameters concerned when designing or testing a vehicle: the drag coefficient and the lift coefficient. The drag coefficient is responsible for how smooth the air passes around the vehicle body and how vortices are generated behind the body and the drag force applied at the rear of the vehicle. The drag coefficient is calculated by the following formula:

$$C_d = \frac{F_D}{\frac{1}{2} \rho U^2 A} \quad (2.2)$$

Where, F_D is the drag force (N), ρ is the density (Kg/m^3), U is the fluid velocity (m/s), and A is the reference area (m^2). The lower the drag coefficient the better the fuel efficiency and the smoother the ride quality. Better fuel efficiency correlate to less fuel consumption at highway speeds because the less drag force exerted which acts as backward pulling force. Ride quality is dictated by many things, but noise levels is a deal breaker for high end luxury cars, the smoother the air travels around the vehicle with less vortices generated results in lower noise emission. The vortices created outside the vehicle create a fluctuating pressure field that causes the vehicle body to vibrate which acts as sound transmitter to the inner cabin.

Another important factor for automobiles is the lift coefficient. Lift coefficient is calculated similar to drag coefficient with just the lift force instead of drag force. The lift force as the name suggests creates an upward force that lifts the vehicle, and this reduces the stability greatly. Unlike airplanes the lift force is needed there to cause flight, but it is undesired in vehicles, and automotive designers look for negative lift value to keep holding the vehicle to the ground at high speeds. The lift coefficient equation is as follows:

$$C_l = \frac{F_L}{\frac{1}{2} \rho U^2 A} \quad (2.3)$$

Where, F_L is the lift force (N), ρ is the density (Kg/m^3), U is the fluid velocity (m/s), and A is the reference area (m^2).

2.2.2.2 Navier Stokes equation

The one-million-dollar question of deriving a mathematical model to represent fluid behaviour is still open to the public, but right now Navier-Stokes equation is the most accurate and precise equation derived. Originally (Navier, 1822) developed a mathematical model to represent viscosity, then (Stokes, 1850) improved on his work to reach the current mathematical model. Any CFD model of solution is somewhat derived or resembles the Navier-Stokes equation. The following are the three-dimensional unsteady Navier-Stokes equations:

Continuity Equation (2.4)

$$\frac{\partial U}{\partial x} + \frac{\partial V}{\partial y} + \frac{\partial W}{\partial z} = 0$$

X – momentum (2.5)

$$\begin{aligned} \frac{du}{dt} + u \frac{\partial u}{\partial x} + v \frac{\partial u}{\partial y} + w \frac{\partial u}{\partial z} \\ = -\frac{1}{\rho} \frac{dP}{dx} + g_x + \frac{\mu}{\rho} \left[\frac{\partial^2 u}{\partial x^2} + \frac{\partial^2 u}{\partial y^2} + \frac{\partial^2 u}{\partial z^2} \right] \end{aligned}$$

Y- momentum (2.6)

$$\begin{aligned} \frac{dv}{dt} + u \frac{\partial v}{\partial x} + v \frac{\partial v}{\partial y} + w \frac{\partial v}{\partial z} \\ = -\frac{1}{\rho} \frac{dP}{dy} + g_y + \frac{\mu}{\rho} \left[\frac{\partial^2 v}{\partial x^2} + \frac{\partial^2 v}{\partial y^2} + \frac{\partial^2 v}{\partial z^2} \right] \end{aligned}$$

Z- momentum

(2.7)

$$\begin{aligned} \frac{dw}{dt} + u \frac{\partial w}{\partial x} + v \frac{\partial w}{\partial y} + w \frac{\partial w}{\partial z} \\ = -\frac{1}{\rho} \frac{dP}{dz} + g_z + \frac{\mu}{\rho} \left[\frac{\partial^2 w}{\partial x^2} + \frac{\partial^2 w}{\partial y^2} + \frac{\partial^2 w}{\partial z^2} \right] \end{aligned}$$

Where, t is time, P is pressure, q is the heat flux, ρ is the density, μ is the viscosity, and the velocities are u , v , w in the x , y , and z direction respectively. The gravity component is represented by g in each equation.

2.2.2.3 Turbulence models for automotive applications

In recent research, (TAŞTAN, 2011) compared the reliability and performance of turbulence models used in CFD software to determine the aerodynamic features over passenger cars. The geometry adopted in the simulations was based in a BMW 3-series passenger car, in 1/6 scale. The Rhinoceros and Catia CAD software were employed to generate the vehicle in IGES format. Afterwards, the geometry was imported into Gambit software and the surface meshing was created. The Tgrid software concluded the volume meshing process.

The researcher ran the CFD simulations in the ANSYS Fluent software, where the reliability and performance of seven turbulence models were tested: (i) Spalart-Allmaras, (ii) standard $kk-\varepsilon$, (iii) RNG $kk-\varepsilon$, (iv) realizable $kk-\varepsilon$, (v) standard $kk-\omega$, (vi) SST $kk-\omega$, and (vii) Reynolds Stress Model. The results were expressed by drag and pressure coefficients, streamlines, velocity and pressure distributions in different positions in the symmetry plane.

As the main contribution of (TAŞTAN, 2011), the author established the following brief description of each turbulence model tested.

2.2.2.3.1 *k-Epsilon model*

The accuracy of drag prediction is under the average of the other models. Pressure coefficient results are on the average of other models. Like other models, pressure peak at a same point is not detected. The general flow pattern around the car is predicted realistically. Computational cost of this model is a bit high compared to other $kk-\varepsilon$ models. Despite higher computational cost, this model does not excel RNG $kk-\varepsilon$ model.

2.2.2.3.2 *k-Omega model*

Regarding drag force, this model gives most accurate results. For velocities between 13 and 25 mm/ss , the error in C_d is under 2%. Pressure distribution is relatively accurate. Whenever compared to the other models, this turbulence model predicts the most accurate pressure coefficient at rear-end edge. However, the wake vortex predicted is much stronger and recirculation region at the wake is larger. A tiny vortex formation is observed at the beginning of the windshield due to local separation bubble. Flow at the sides is predicted as similar to other models. Computational cost is higher than $kk-\varepsilon$ models, but this model outshines $kk-\varepsilon$ models according to overall results.

Drag results are on the average of the other models, similarly to the pressure coefficient results. The prediction of general flow pattern around the car is realistic. Contribution of side flow separation to recirculation region at the wake is predicted as much stronger compared to other models. In the view of computational effort, this model is the most expensive two-equation turbulence model. Nevertheless, the computational time is similar to the average value of other two-equation models.

K-Omega is another turbulence model and has been proposed to give better performance in adverse pressure gradient, to overcome the limitation

of the K-Epsilon model. The two-equation model is as shown by (Wilcox, 1988, 2006, 2008):

$$\frac{\partial(\rho k)}{\partial t} + \frac{\partial(\rho u_j k)}{\partial x_j} = P - \beta \rho \omega k + \frac{\partial}{\partial x_j} \left[\left(\mu + \sigma_k \frac{\rho k}{\omega} \right) \frac{\partial k}{\partial x_j} \right] \quad (2.8)$$

$$\begin{aligned} \frac{\partial(\rho \omega)}{\partial t} + \frac{\partial(\rho u_j \omega)}{\partial x_j} &= \frac{\gamma \omega}{k} P - \beta \rho \omega^2 + \frac{\partial}{\partial x_j} \left[\left(\mu + \sigma_k \frac{\rho k}{\omega} \right) \frac{\partial k}{\partial x_j} \right] \\ &+ \frac{\rho \sigma_d}{\omega} \frac{\partial k}{\partial x_j} \frac{\partial \omega}{\partial x_j} \end{aligned} \quad (2.9)$$

Where,

$$P = \tau_{ij} \frac{\partial u_x}{\partial x_j} \quad (2.10)$$

$$\tau_{ij} = \mu_t \left(2S_{ij} - \frac{2}{3} \frac{\partial \mu k}{\partial x_k} \delta_{ij} \right) - \frac{2}{3} \rho k \delta_{xj} \quad (2.11)$$

$$S_{ij} = \frac{1}{2} \left(\frac{\partial u_x}{\partial x_j} + \frac{\partial u_j}{\partial x_i} \right) \quad (2.12)$$

For the turbulent eddy viscosity:

$$\mu_t = \frac{\rho k}{\hat{\omega}} \quad (2.13)$$

$$\hat{\omega} = \max \left[\omega, C_{lim} \sqrt{\frac{2\overline{S_{ij}} \overline{S_{ij}}}{\beta^*}} \right] \quad (2.14)$$

$$\overline{S_{ij}} = S_{ij} - \frac{1}{3} \frac{\partial K_{ij}}{UK \partial x_k} \delta_{xj} \quad (2.15)$$

Where ρ is the density, and μ is the molecular dynamic viscosity as discussed by (Menter, 1992). With the following parameter values: $\alpha_*=1$, $\alpha=0.52$, $\beta^*=0.09$, $\partial 1=0.31$, $\beta_{inner}=0.075$, $\beta_{outer}=0.0828$, $TKE_{inner}=1.176$,

$TKE_{outer}=1$, $SDR_{inner}=2$, $SDR_{outer}=1.168$, and the production limiter clip factor = 10 as discussed by (Kok, 2000).

2.2.2.3.3 Scale Adaptive Simulation (SAS)

The current turbulence models suffer from the lack of an underlying exact transport equation as explained by (Egorov et al., 2010). This lack of an exact solution for the omega and epsilon equations leads to an inaccurate solution for large scales. The research done by (Rotta, 1951) developed a more consistent approach for formulating a scale-equation. The SST-SAS transport equations in ANSYS are based on (Rotta, 1951) approach, and are defined as:

$$\frac{\partial pk}{\partial t} + \frac{\partial}{\partial x_i}(\rho u_i k) = G_k - \rho c_\mu k \omega + \frac{\partial}{\partial x_j} \left[\left(\mu + \frac{\mu_t}{\sigma_k} \right) \frac{\partial k}{\partial x_j} \right] \quad (2.16)$$

$$\begin{aligned} \frac{\partial \rho \omega}{\partial t} + \frac{\partial}{\partial x_i}(\rho u_i \omega) \\ = \alpha \frac{\omega}{k} G_k - \rho \beta \omega^2 + Q_{SAS} + \frac{\partial}{\partial x_i} \left[\left(\mu + \frac{\mu_t}{\sigma_\omega} \right) \frac{\partial \omega}{\partial x_j} \right] \\ + (1 - F_1) \frac{2\rho}{\sigma_{\omega,2}} \frac{1}{\omega} \frac{\partial k}{\partial x_j} \frac{\partial \omega}{\partial x_j} \end{aligned} \quad (2.17)$$

Where p is the pressure, t is the time, i, j, and k are the unit vectors, F is the force, ρ is the density, C_s is a constant with value of 0.11, as well as α, β, ω , and σ . A more detailed derivation for the equation (or equations) is done by (Egorov et al., 2010).

2.2.2.3.4 Large Eddy Simulation (LES)

As the name suggests, it deals with large eddies formed in the studied area (Figure 20), and it follows a direct solution method called Direct Numerical Simulation (DNS). LES model is not utilized in this thesis but is

worth mentioning as it is one of the most popular turbulence models. DNS is great for solving case studies, but not in high turbulent flows. For the small eddies that cannot be captured by the mesh size they are accounted for by modelling. It is worth mentioning that huge cost of LES, as it depends on the value of Reynolds number (Re) by Re^3 , so the larger the Re the more computational cost is required. The LES turbulence model solves for large eddies as mentioned, and for the smaller eddies there are different model choices. The wale adapting local eddy viscosity (WALE) model is the most famous and the eddy viscosity is modelled by:

$$\mu_t = \rho L_s^2 \frac{(S_{ij}^d S_{ij}^d)^{3/2}}{(\overline{S_{ij} S_{ij}})^{5/2} + (S_{ij}^d S_{ij}^d)^{5/4}} \quad (2.18)$$

Where L_s and S_{ij}^d in the WALE model are defined as

$$L_s = \min(kd, C_w V^{1/3}) \quad (2.19)$$

$$S_{ij}^d = \frac{1}{2}(\bar{g}_{ij}^2 + \bar{g}_{ij}^2) - \frac{1}{3}\delta_{ij}\bar{g}_{kk}^2 \quad (2.20)$$

$$\bar{g}_{ij} = \frac{\partial \bar{u}_i}{\partial x_j} \quad (2.21)$$

Where $k=0.41$ is the von Karman constant, and the values of WALE constant that result superior results in ANSYS fluent is $C_w = 0.325$. The WALE model is more preferred than Smagorinsky-Lilly model because it returns a zero turbulent viscosity for laminar shear flows.

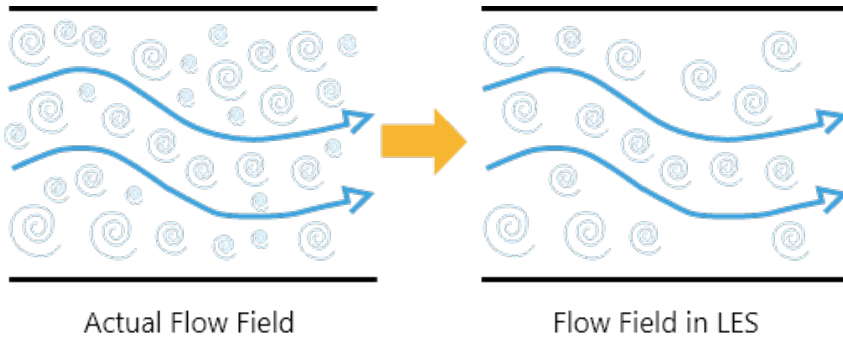


Figure 20: LES perception of flow.

2.2.2.3.5 Detached Eddy Simulation (DES)

Since LES model is mentioned, DES model should also be included as DES utilizes LES. The DES model is a hybrid between LES and Reynolds Averaged Navier Stokes (RANS), as it fulfills the gap of small eddies calculation using RANS. However, the model requires less computational cost than LES but more than RANS. ‘Detached Eddy’ term refers to ‘eddy that is apart from wall’ as in eddies that drift away from walls (Figure 21). In terms of the model equation, it depends on which model DES is paired with.

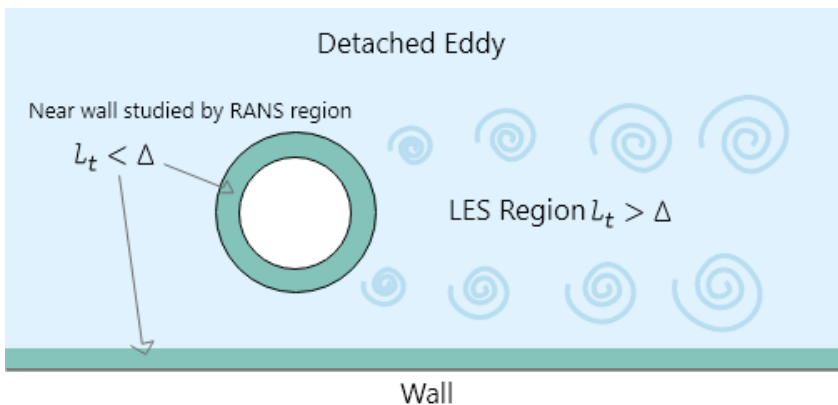


Figure 21: Illustration of Detached Eddy Simulation.

2.2.2.3.6 Ffowcs-Williams and Hawking (FW-H)

Turbulence models are used for general numerical airflow solution. However, if acoustics are desired the turbulence model should be accompanied with an acoustics model. The Ffowcs-Williams and Hawking model (FW-H) is an inhomogeneous wave equation that is derived from the continuity and the Navier-Stokes equations it is used to solve for acoustics. The FW-H model works with transient case turbulence model. The FW-H equation is written as follows (Ffowcs Williams, J. E., and Hawkings, 1969):

$$\begin{aligned} \frac{1}{a_0^2} \frac{\partial^2 p'}{\partial t^2} - \nabla^2 p' &= \frac{\partial^2}{\partial x_i \partial x_j} \{T_{ij} H(f)\} \\ &- \frac{\partial}{\partial x_i} \{[P_{ij} n_j + \rho u_i (u_n - v_n)] \delta(f)\} \\ &+ \frac{\partial}{\partial t} \{[P_o v_n + \rho (u_n - v_n)] \delta(f)\} \end{aligned} \quad (2.22)$$

Where u_i is the fluid velocity component in the Xi direction, u_n is the fluid velocity component normal to the surface $f=0$, v_i and v_n are the surface velocity component in the Xi direction, and normal to the surface, respectively, $\delta(f)$ is the Dirac delta function, and $H(f)$ is the Heaviside function.

The wave equation is integrated analytically following the assumption of the absence of obstacles between the sound sources and the receivers since it is a free-space flow. The solution is a combination of surface and volume integrals. The volume integrals contribution is neglected in low subsonic flow. Therefore, ANSYS fluent solution becomes:

$$p'(\vec{x}, t) = p'_T(\vec{x}, t) + p'_L(\vec{x}, t) \quad (2.23)$$

$$\text{Where,} \quad (2.24)$$

$$4\pi p'_T(\vec{x}, t) = \int_{f=0} \left[\frac{p_o(\dot{U}_n + U_{\dot{n}})}{r(1 - M_r)^2} \right] dS \quad (2.25)$$

$$+ \int_{f=0} \left[\frac{p_o U_n \{r\dot{M}_r + a_o(M_r - M^2)\}}{r^2 (1 - M_r)^3} \right] dS$$

$$4\pi p'_L(\vec{x}, t) = \frac{1}{a_o} \int_{f=0} \left[\frac{\dot{L}_r}{r(1 - M_r)^2} \right] dS + \int_{f=0} \left[\frac{L_r - L_M}{r^2 (1 - M_r)^2} \right] dS \quad (2.26)$$

$$+ \frac{1}{a_o} \int_{f=0} \left[\frac{L_r \{r\dot{M}_r + a_o(M_r - M^2)\}}{r^2 (1 - M_r)^3} \right] dS$$

Where,

$$U_i = v_i + \frac{\rho}{\rho_o} (u_i - v_i) \quad (2.27)$$

$$L_i = P_{ij} \hat{n}_j + \rho u_i (u_n - v_n) \quad (2.28)$$

2.2.2.3.7 Summary of turbulence models

When it comes to any simulation there is no right way of doing it, because it depends on the constraints, and in simulation case it depends on the available resources and time constraint. In CFD simulation two main approaches can be followed, either highest accuracy or lowest computational cost, but both resulting accurate results compared to experimental. Table 5 shows the different setup that could be followed for 3D approach. Table 5 is written based on 3D DrivAer model simulation at 16 m/s speed done by (Soares, 2015).

Table 5: Setup comparison between low computational cost versus numerical accuracy

Factor	Low Computational Cost	Numerical Accuracy
Model	Half-model	Full-model
Turbulence model	Realizable K-Epsilon	Realizable K-Epsilon
Gradient	2 nd -order Green Gauss	2 nd -order Hybrid Gauss-LSQ
Mesh base size	10 mm	05 mm

2.2.2.3.8 Gradient scheme

In order to calculate the transmission between properties between every node/cell a gradient scheme is used. In every simulation in this thesis, least squares-cell method is chosen as the gradient scheme. An explanation of the working model of two gradient schemes is presented and the difference between both is shown. In Fluent software's the flow variables such as temperature, pressure and velocity are stored at the cell centroid. For some calculations the gradient of these variables is required. The gradient is required for linear upwind differencing, non-orthogonal correctors, and a variety of other sources seen in fluent setup process. Least-Squares Gradient (LSQ) is a method to calculate the gradient at the cell centroid, other popular gradient method is green-gauss and the Node-Based schemes. Since the Least-Squares Gradient is an advanced method over the original Green-Gauss gradient (GG) and Node based methods, previous models need to be explained in order to appreciate the new and latest advancements in calculating the gradient.

Taking GG scheme as an example, a cell as shown in Figure 22 with any number of sides on the elements and to calculate the gradient at the

centroid each cell face is looked at and a unit normal vector n is multiplied by the area of the face and also by the value of the field at the center of that face. Shown in Figure 22 is the face value, which could be temperature, velocity or any other parameter, and A is the reference area. For example, if temperature is the desired value, the temperature at the center of the face is taken then multiplied by the area and the normal vector, then add up those contributions for all of the cell faces. Therefore, the gradient method works for different number of faces. Lastly, the resulted value is divided by the volume of the cell, and this results the gradient of the centroid, as shown in the following equation.

$$(\nabla T)_p = \frac{1}{V_p} \sum [T_f \hat{n}_f A_f] \tag{2.29}$$

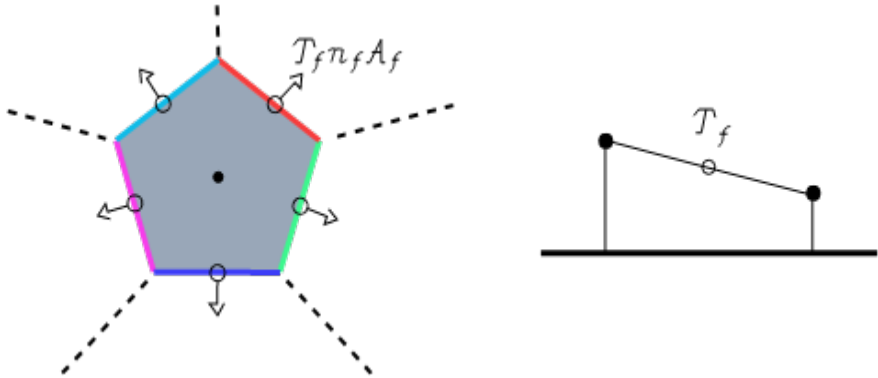


Figure 22: Green Gauss and Node Based methods for computing the gradient.

Unlike the GG method, the LSQ does not include the face values T_f , but a more of cell value to cell value approach, disregarding the number of sides of the elements. Having the centroid value of an element (T_p) and the centroid of a neighboring element value is desired (T_N) as shown in Figure 23. The centroid is calculated by a linear extrapolation method as shown in the following equation.

$$T_N = T_P + d_{PN} \cdot (\nabla T)_P \quad (2.30)$$

Where to calculate the new cell centroid value, the value of the previous neighbouring cell (T_P) is added with the multiplication of the distance vector (d_{PN}) multiplied by the gradient of the centroid $(\nabla T)_P$. The only unknown is the gradient, which is what the method solves for. Continuing the solution, this approach is repeated for each cell side N, which creates a matrix solution. However, the matrix does not result in an exact solution since it is not a square matrix. The resulted matrix is in the form of $(N \times 3) \times (3 \times 1) = (N \times 1)$. The LSQ method (Figure 23) solves based on approximation and error (ϵ), each side equation is used for error, and the uniqueness of the LSQ method is that it takes the sum of the error squared and aim to minimize it.

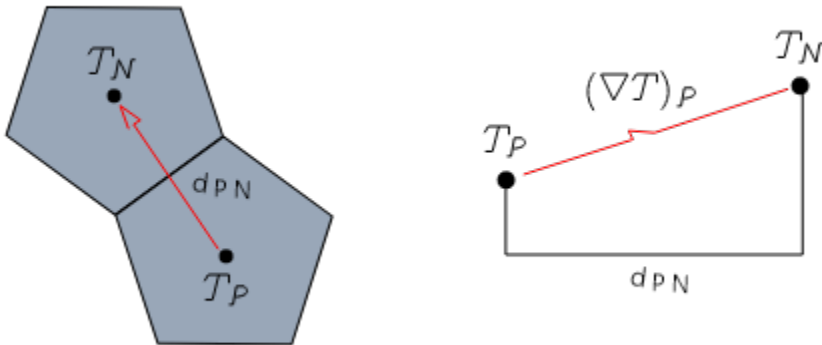


Figure 23: Least-Squares Cell Method for calculating the gradient.

After discussing the main turbulence models and acoustic model for transient flow, as well as the gradient scheme solution model. Each case in this thesis is set with the appropriate model depending on the required simulation and results.

2.2.2.4 Exhaust flow modelling

The calculation model is taken from (Soares, 2015). To simulate the effect of exhaust on the aerodynamics of the vehicle, the amount of gas at the outlet needs to be known. However, the exact value of any vehicle is unknown, therefore estimations are made for several parameters, such as, mass rate of fuel, fuel to air mass ratio, and exhaust mass flow. Then a realistic exhaust flow rate is calculated.

2.2.2.4.1 Mass flow rate of fuel

Of course, the exhaust pipe does not eject air at a constant value, but assumptions are necessary when simulating real life as accurately as possible. Firstly, an estimation of the volumetric amount of fuel consumed per second ($\Delta_f[l/s]$) is calculated as a function of velocity ($U_V[m/s]$) and fuel consumption ($\mathcal{X}[km/l]$). The equation is expressed as follows:

$$\Delta_f = \frac{U_V}{1000\mathcal{X}} \quad (2.31)$$

Δ_f is expressed in ($\rho_f[kg/m^3]$). Using the above equation, the mass of fuel ($\rho_f[kg/m^3]$) consumed is calculated as

$$\dot{m}_f = \rho_f \Delta_f = \frac{\rho_f U_V}{1000\mathcal{X}} \quad (2.32)$$

2.2.2.4.2 Fuel to air mass ratio

The combustion stoichiometry in the engine allows for evaluation of the theoretical fuel/air mass ratio (ϕ_{eq}) taken from (Bauer et al., 1998; Caton & Heywood, 1981), in the following equation:

$$\phi_{eq} = \left(\frac{m_f}{m_{air}} \right)_{eq} \quad (2.33)$$

It should be noted that each ICE vehicle is equipped with an Air/Fuel ratio sensor that adapts constantly to the air intake and amount of speed desired. Therefore, it is difficult to estimate a constant value, so the parameter r is adopted as air fuel mixture ratio. The r ratio below 1 represents the engine regime of full combustion of oxygen, which provides the maximum power from the engine. On the other side, r higher than 1 is related to engine regime that ensures the full combustion.

Following a similar approach to (Soares, 2015), and taking similar assumption for results verification as shown in Table 6.

Table 6: Values taken in solving for mass exhaust out

Parameter	Symbol	Description
Fuel	-	Isooctane (C_8H_{18})
Fuel density	ρ_f	740 kg/m^3
Fuel consumption	\mathcal{X}	12.3 Km/l
Car speed	U_∞	40 m/s
Air mixture ratio	r	1.05

Using the assumption made by Renan in the following equation, results in a mass flow rate of 40.4 g/s.

$$\dot{m}_r = (1 + r \phi_{eq}) \frac{\rho_f U_V}{1000X} \quad (2.34)$$

The value obtained is used in every exhaust position as the mass flow outlet in ANSYS simulation.

2.2.3 Numerical setup

The setup used in ANSYS is mentioned for each case with the governing values of the equation where applicable.

2.2.3.1 Side mirror base part 1 ANSYS setup

Since the main objective of this section is to observe the concept of mirror base effect the main focus is if change is noticed or not. Therefore, steady state solution is utilized. The methodology used in this paper is written in Table 7.

Table 7: ANSYS functions and model parameter chosen.

Property	Setup
Viscous	SST K-Omega
Values	
$\alpha_* = 1$	$\alpha = 0.52$
$\beta^* = 0.09$	$\partial 1 = 0.31$
$\beta_{inner} = 0.075$	$\beta_{outer} = 0.0828$
$TKE_{inner} = 1.176$	$TKE_{outer} = 1$
$SDR_{inner} = 2$	$SDR_{outer} = 1.168$
<i>Production Limiter Clip Factor = 10</i>	
Algorithm	SIMPLE
Solution Method	
Gradient	Least Squares Cells Based
Pressure	Second Order
Momentum	Second Order Upwind
Turbulent Kinetic Energy	Second Order Upwind
Specific Dissipation Rate	Second Order Upwind
With Warped Face Gradient Correction Applied	
Time	Steady
Mesh	Polyhedral
Acoustics	Broadband Noise Sources
Mesh Grid	Fine Mesh
Type	Pressure Based
With No Slip Condition Applied	
Residual	0.001
Iterations	1000
Standard Initialization	
Turbulent Kinetic Energy	1.851482 (m2/s2)
Specific Dissipation Rate	12675 (1/s)

2.2.3.2 Side mirror base part 2 ANSYS setup

Sound reaches the driver by a series of events: first, air causes fluctuating pressure on the side glass, next the glass (solid) transmits the waves inside the medium, and finally, vibrations created in the inner air cabin reach the driver's ears. To simulate this model known as Aero-Vibro-Acoustics, a three-part process must be followed, consisting of an ANSYS fluent, then an ANSYS mechanical structure, and finally an ANSYS harmonic acoustics, where first the turbulence created by the vehicle is measured outside, then the solid transmission is simulated with ANSYS mechanical, and finally the structure acts as a vibrator created noise inside the cabin using ANSYS harmonic acoustics. In the studied case the outside window is concentrated on because the goal is to compare alternative angle positions for the same scenario, as a comparative study. In many applications, the sound radiation from a uniform flow over a stationary object is focused on. For example, model testing in wind tunnels is a uniform steady flow at large distances from the region of turbulence that causes the sound. In principle, the modified equation can be solved using the techniques described earlier in this section using solutions to the convected wave equation model by (Weckmüller et al., 2010). Therefore, Ffowcs-Williams & Hawkings (FFW) formulation model is used to extract acoustic data with Hanning window, with the mirror and base set as the source and 13 receivers placed on the vehicle side to collect data (Figure 24). Ffowcs-Williams and Hawkings model is verified to output accurate and precise results by (Li & Sharma, 2021) and (Wu et al., 2022).

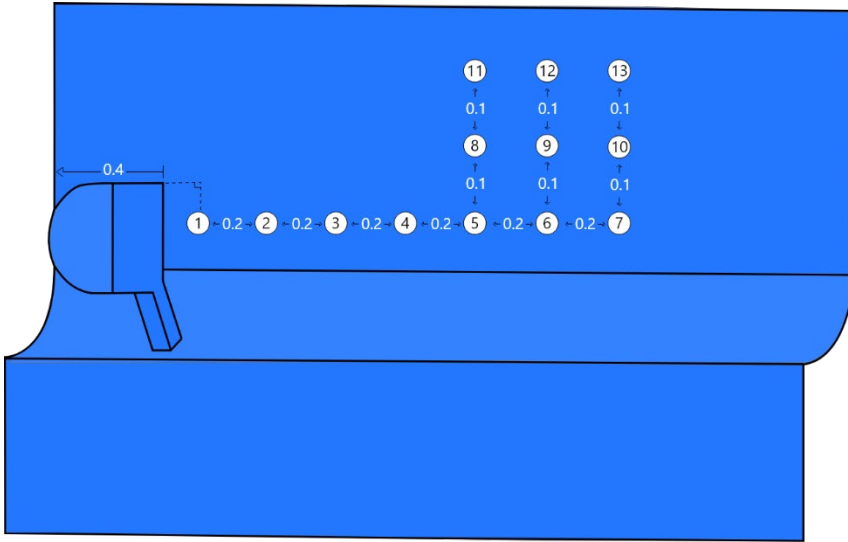


Figure 24: Receivers location on vehicle's side.

Air after hitting the side mirror becomes turbulent and turbulent air is hard to be transient and changes with time, but a steady state solution can be obtained for a specific time and compared with the steady state cases. As long as the comparison is fair then the studied case in this thesis is valid.

Since this is a transient flow the number of time steps and the size of it is very important. The air flow speed is considered 40 m/s and therefore, it crosses the 2.2 meters study area in 0.055 seconds. As, vortices occur, the simulation will take time longer than this. Therefore, the simulation is run till 0.0825 seconds, and the maximum iterations are chosen based on whenever the residuals start to become constant or reach convergence. Table 8 shows the methodology utilized in simulating the optimum mirror angle in mirror base simulation part 2.

Table 8: Methodology used in ANSYS.

Title	Setup
Flow	Incompressible
Turbulence model	Scale Adaptive Simulation
Air Flow Velocity	40 m/s
Algorithm	PISO
Gradient	Least squares cells based
Warped Face Gradient Correction	Applied
Mesh	Polyhedral
Acoustics	FFW
Type	Pressure based

2.2.3.3 Vehicle rear exhaust

Since 2D model simulation is proven to be a more reliable and very less time consuming when compared to its 3D counterpart. The exhaust simulation is conducted in 2D domain on the DrivAer model. This approach will not affect the credibility of the results, since the main focus is the exhaust system at different heights from the ground without considering the 3D domain effects, as the simulation is considered symmetrical.

The methodology used in simulating the exhaust pipe at different location is shown in Table 9. As well as in the 2D DrivAer model validation a similar method is chosen, as it proved to be the most reliable for 2D simulating.

For conducting the simulation, 9 different positions for the exhaust are studied with a constant spacing of 25 mm between centre to centre (Figure 25). The exhaust pipe is 20 mm in height with rounded edges for easier meshing of radius 1 mm. For fair comparison, the added cutting area in the 2D DrivAer simulation is pursued to be constant for each position as much as possible, of course having the area to be exactly same is difficult since no sharp edges are possible for meshing to work easier. For reference the first

exhaust is distanced 94.5 mm above the touching point of the wheel and the ground, and for position 9 it is 294.5 mm above the wheel surface with contact to the ground. The exhaust pipes are added to the 4th generation DrivAer model done by (Soares et al., 2018), which is 35% smaller than the original model. Therefore, the rear height is measured as ~260 mm, so a change of 25 mm is around 10% difference in total height.

Table 9: Methodology used in simulating different exhaust pipe positions and DrivAer model validation.

Title	Setup
Flow	Incompressible
Turbulence model	K-omega
Air Flow Velocity	16 m/s
Algorithm	Coupled
Gradient	Least squares cells based
Mesh	Quad/Tri
Type	Pressure Based

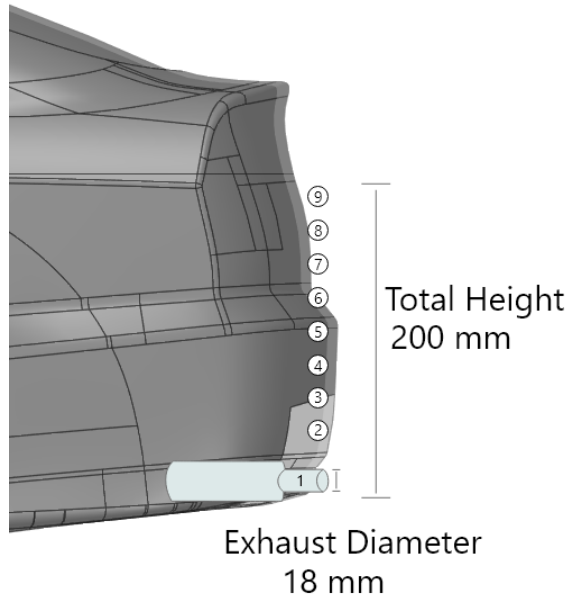


Figure 25: Exhaust pipe different testing positions, with spacing of 25 mm.

2.2.3 Boundary conditions

In order to accurately represent real cases in simulation, accurate boundary conditions are required with values as the real experimentation. Therefore, this section shows each case's boundary conditions applied in the ANSYS fluent solver.

2.2.3.1 Side mirror base part 1 and part 2 boundary conditions

In both part 1 and 2 of the mirror base model the geometry has almost the same parts with the only difference of shape around the mirror. Therefore, the boundary conditions are mentioned for mirror base part 2 which is the similar to part 1 except for the velocity value, as in part 1 multiple airflow velocities are examined.

Figure 26 shows the coloured boundary conditions. In Figure 26 there are two displaces, one without the outside boundary wall, and other with the

boundary wall. In Figure 26 the purple surface is the inlet and the red surface is the outlet, the grey part is the mirror and car surface, and the green wall is the boundary wall. In CFD simulation the geometry is designed first then an enclosure is created that surround the body and act as the boundary of the studied area, the boundary conditions are shown in Table 10 with reference to Figure 26 colors.

Table 10: Boundary conditions for mirror base part 2 with reference to Figure 26.

Boundary	Setup
Inlet (Purple)	Varying velocity
Outlet (Red)	Pressure outlet atmospheric
Mirror and Base (Light Grey)	No-slip wall surface
Vehicle body (Light Grey)	No-slip wall surface
Top and bottom wall (Green)	Slip, zero shear wall
Wall opposite to vehicle body (Green)	Slip, zero shear wall

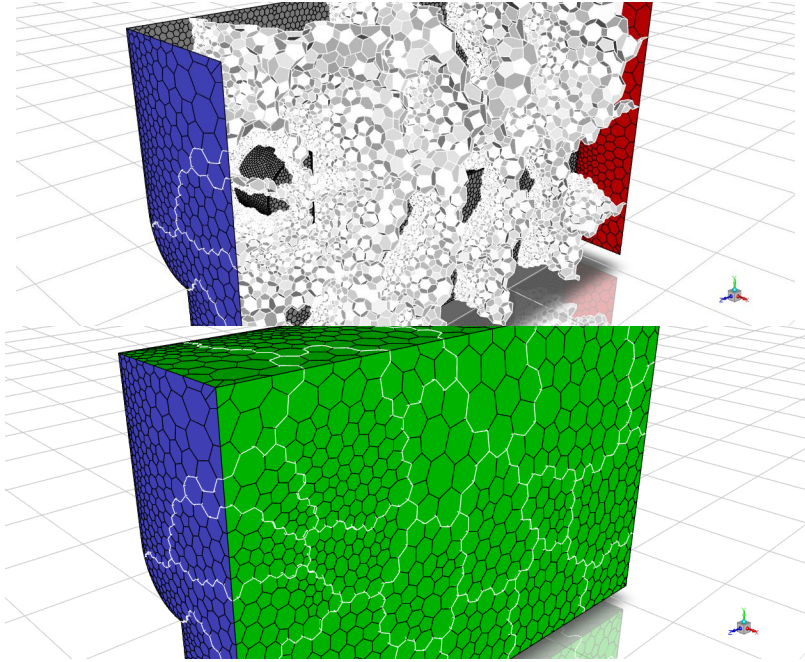


Figure 26: View of the case study, without the outside boundary wall (top), and with the boundary wall (bottom).

2.2.3.3 Vehicle rear exhaust boundary conditions

Utilizing the previous information on boundary layers and fluid separation, the values for this simulation are displayed in Table 11, which displays the boundary conditions. The boundary for the problem is shown in Figure 27.

Table 11: Boundary conditions set for every exhaust simulation

Boundary	Condition	Parameters
DrivAer car	Wall	No-Slip
Inlet	Velocity-inlet	16 m/s
Outlet	Pressure-outlet	
Top line	Symmetry	
Ground	Wall	Zero shear
Exhaust wall	Wall	No-Slip
Exhaust jet	Mass flow inlet	$\dot{m}_{exhaust} = 40.4 \text{ g/s}$

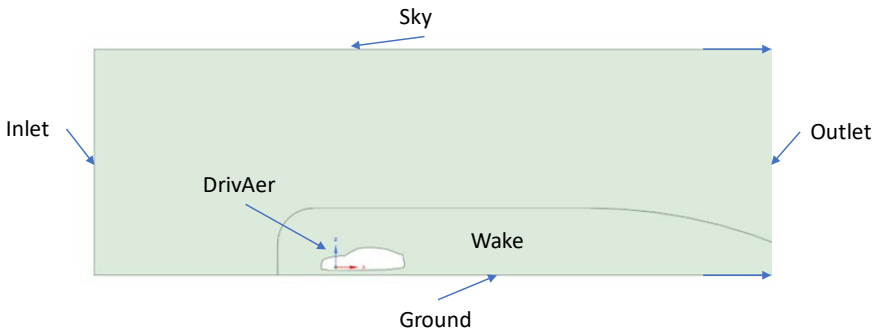


Figure 27: Boundary labels for 2D simulation.

2.3 Model validation

Verification of results is the most important part of the engineer’s project. Before engineers relied on experimentation only to verify the results and determine the method of optimization and how to proceed with the final design. However, now that technology developed and high-end CPUs are available, simulating programs are developed backed by numerical equations to represent the experiment numerically. This resulted in easier access to predict the actual performance with a cheaper and very accessible method. However, this does not exclude the importance of experimentation, as a reference is required to check if the numerical analysis is correct. Ever since simulations are gaining popularity with continuous work on improved

methods to implement in the programs to provide more accurate results. In the following chapter after the results are presented an experimental validation is linked through literature or shown in the work.

Chapter 3

Chapter 3: Results and Discussion

In this chapter, the simulation results are reported and discussed with validation. Mesh method and analysis will be presented. The three cases studied are mirror base part 1, part 2, and exhaust pipe position. The results of aerodynamic forces and aeroacoustics analysis due to changing the side mirror base position are discussed in detail. Also, the optimum angle value that results in the least aerodynamic forces and/or aeroacoustics generated is determined. The results relevant to the exhaust pipe position that results in the least aerodynamic force, either drag or lift and aeroacoustics are also presented in this chapter. In CFD simulation, a method of mesh refining is sometimes used to make sure accurate results are outputted. This method is continuous trial and error mesh refining method, that aim to record whether the obtained values converge with respect to number of elements (mesh size). The method of continuous trial and error to find the optimum mesh size should not be always followed as accurate results could be found easily with first trial. To illustrate, if the geometry is small, the least mesh element size (5 mm) could be chosen at the first trial to output the most accurate results, and since the geometry is small, not many elements will exist. Therefore, the computational time required will be relatively short compared to the continuous trial and error process.

3.1 Geometry meshing and convergence

Mesh refining is an important step in any numerical simulation, where in CFD software's usually the automatically generated mesh is inaccurate with large size elements. Therefore, the mesh size is reduced in areas with high computational requirement and increased in areas with less accuracy is needed. This section is divided into three sub-sections, each discussing the mesh refining process for the respective case.

3.1.1 Side mirror base meshing

Six different inlet airflow velocities of: 22.22, 27.78, 33.33, 40, 44.44, 50 m/s (80, 100, 120, 144, 160, 180 Km/h respectively) are examined, to find the drag and lift forces at each velocity. At each velocity the maximum and minimum sound generated on vehicle side body is presented. The body material is assumed to be made from Aluminum. Aluminum Roughness is set to be 0.345. The reason for choosing aluminum as the body material because this is the current trend in automotive industries. The material type will have no effect on the results. The Mesh size should be chosen to yield the best results without taking long computational time. Polyhedral mesh is used, as it provides results similar to Tetrahedral Mesh but with less computational time (Figure 28). Figure 28 shows the dense area of elements near the mirror part which is the most important area that needs high computational accuracy. Then the element size increases away from the mirror, where less computational accuracy is needed. The difference between both meshes types is shown in Table 12, where it is noted that polyhedral mesh values are lower than tetrahedral values as according to (Afgan et al., 2008) even with the same element size. Therefore, the accuracy and efficiency of polyhedral mesh is as described by (Afgan et al., 2008). The SIMPLE algorithm is used with the following settings, Least Squares Cell-Based Gradient, Second Order Pressure, Second-Order Upwind Momentum, Second-Order Upwind Turbulent Kinetic Energy, and Second-Order Upwind for Specific Dissipation Rate, with Wrapped-Face Gradient Correction. The values for the element size are chosen based on the results reported in the literature. To illustrate, the lowest size used in ANSYS fluent is 5 mm, and this is proven to produce accurate results, but with longer computational time. However, in the side mirror base meshing case the studied volume is small and even if the 5 mm mesh size is chosen it won't have much of a difference on

computational time. Therefore, in ANSYS fluent meshing the mirror and base exterior surface is set at 5 mm and the vehicle body at 10 mm.

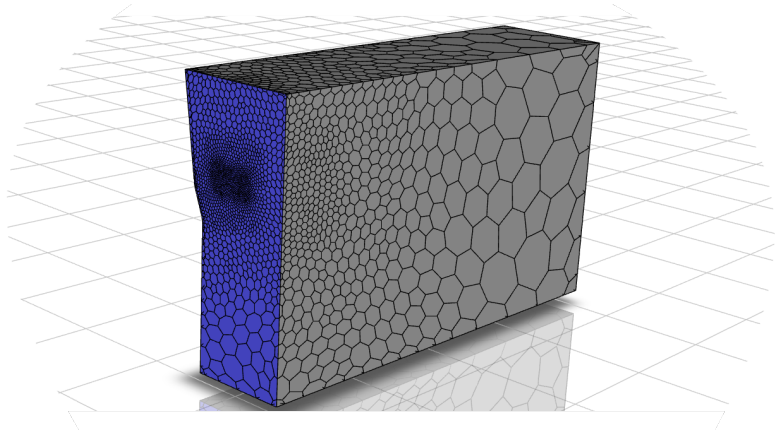


Figure 28: Geometry studied for side mirror base part 1 with generated mesh.

Table 12: Difference between tetrahedral and polyhedral meshing.

Mesh type	Tetrahedral	Polyhedral
Level	0	0
Cells	187322	39723
Faces	382131	255804
Nodes	35177	211780
Partitions	16	16
Cell zone	1	1
Faces	6	6

Figure 29 shows the mesh refining method done for the geometry. For the mesh refining process, ANSYS fluent generates automatic mesh at first, and the solver runs, and results are recorded. Then a mesh sizing method is applied, taking the mirror and side body surfaces and applying 50 mm

element size, then constantly decreasing the value to 10 mm with a step size of 5 mm. At each step of the mesh refining process, the solver is run, and data is recorded. Figure 29 shows results are in 2 N range, so results are accurate at smaller mesh size.

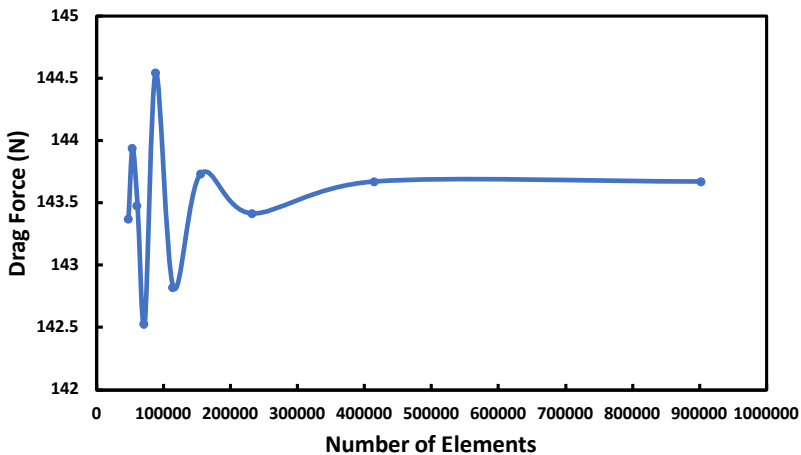


Figure 29: Mesh refining for studying the effect changing the side mirror base have on the drag force (N) with respect to the number of elements.

3.1.2 Side mirror base part 2 geometry meshing

In order to understand how convergence is achieved, the element size and residual are presented. At each element the pressure and velocity components are calculated at the inlet and then at the outlet with assumptions, then the assumed value is checked for error, and this is called residual. In ANSYS simulation, the value of residual desired is set by the user and the solver keeps solving until the number of iterations set or the residual value is reached thus value reaches convergence. The smaller the element size the more precise the results. However, a very small size could be chosen but this may result a long computational time and require high end CPUs. Further, large element size may produce inaccurate results. Therefore, continuous trial

and error is followed to obtain the element size that results relatively constant/converged results.

In this work, ANSYS automatic mesh generator is firstly applied, then the mesh base size is constantly reduced in a trial-and-error method, till a constant output is achieved. The results obtained from mesh refining are shown in Table 13 where the number of nodes and elements for the automatic mesh and the settled mesh size with tetrahedral elements are represented. In the setup phase the mesh is switched to polyhedral thus changing the mesh size as shown in Table 14. The mesh used is divided into 9 zones with total of 351,555 nodes. The mesh is shown in Figure 30 which displays the edges, faces, and partitions in the case study, and as mentioned and clearly shown, polyhedral mesh element is chosen as it is considered to be the best meshing method for CFD analysis as mentioned in Chapter 1 literature review.

Table 13: Tetrahedral mesh analysis number of nodes and elements.

Tetrahedral	Automatic	Modified
Nodes	2,952	59,145
Elements	14,106	312,539

Table 14: Polyhedral mesh analysis and size.

Polyhedral	Automatic	Modified
Cells	4,401	64,768
Faces	25,093	421,606
Nodes	19,289	351,555
Partitions	32	32

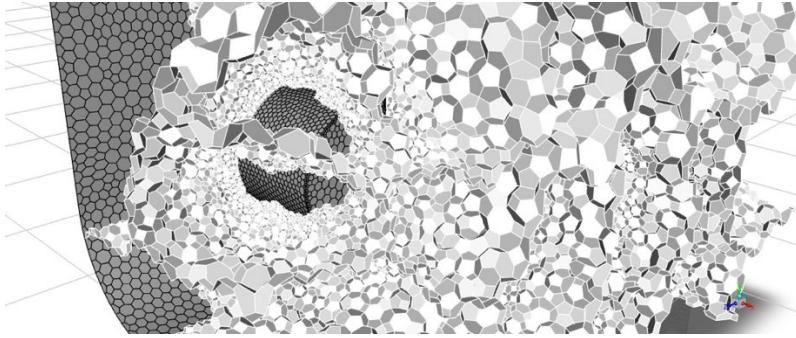


Figure 30: Mesh display for the investigated case shows edges, faces, and partitions inside the studied geometry.

For the mesh refining process, ANSYS fluent generates automatic mesh at first, and the solver runs, and results are recorded. Then a mesh sizing method is applied, taking the mirror and side body surfaces and applying 50 mm element size, then constantly decreasing the value to 10 mm with a step size of 5 mm. At each step of the mesh refining process, the solver is run, and data is recorded. Figure 31 shows results are in 7 N range, so results are accurate at smaller mesh size.

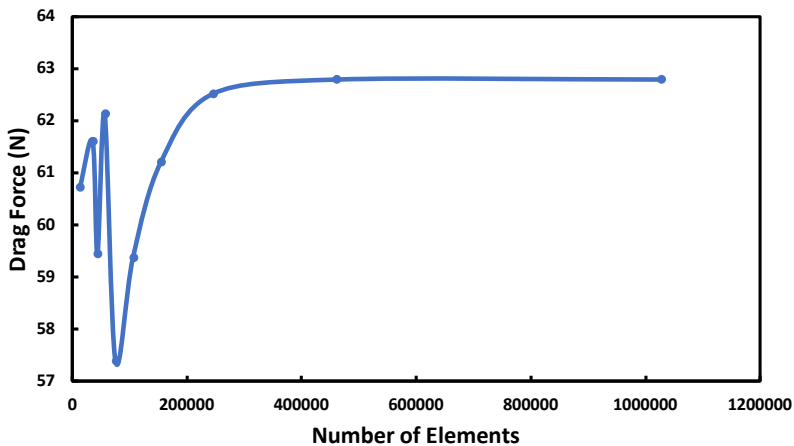


Figure 31: Mesh refining for studying the optimum mirror base orientation that results lowest aeroacoustics and/or aerodynamic forces, the drag force (N) is plotted with respect to the number of elements.

3.1.3 Different exhaust pipe positions mesh model

In the exhaust pipe case, the exhaust outlet is added to the DrivAer model's rear, and the aerodynamic forces are obtained for the whole geometry. Since this case is studied in 2D simulation, it is easier to apply inflation layer meshing to accurately represent the boundary layer separation.

As mentioned, really small mesh size requires large computational time with high accuracy, and large mesh size is computationally easy but with less accurate results. Therefore, a balance is needed between the accuracy and computation time must be established by conducting trial and error case of recording the output at different mesh size, starting from coarse to fine then checking till convergence is achieved.

In order to obtain accurate results from CFD simulation, the boundary layer separation (BLS) needs to be accurately presented. The BLS requires fine mesh around the object that has no-slip condition applied, and the best meshing method that represents the BLS is the inflation layer. At the boundary layer, the no-slip condition creates a fluid boundary layer (δ_{99}) which is the BLS thickness value from the wall, and this value is usually very small, so very small mesh elements are required to simulate this result. Inflation or prism layers are used to simulate boundary layer separation at the wall. To use inflation several parameters are needed (Figure 32). For example, the height of the first layer y_H , and the distance from the wall to the center of the cell y_p , numbers of layers N , and growth rate G , with $G > 1$. The following equations represent how to calculate the inflation layer required parameters. To find the total height of all layers the equation is:

$$y_T = y_H + y_H * G + y_H * G^2 + \dots + y_H * G^{N-1} \quad (3.1)$$

The total height y_T should equal δ_{99} to accurately represent the boundary thickness.

$$\delta_{99} = \frac{4.91L}{\sqrt{Re_L}} \text{ for } Re < 5 \times 10^5 \quad (3.2)$$

$$\delta_{99} = \frac{0.38L}{Re_L^{\frac{1}{5}}} \text{ for } Re > 5 \times 10^5 \quad (3.3)$$

In terms of the total number of layers N , it depends on the y^+ value if $y^+ \sim 30$ then $N = 10$, and if $y^+ \sim 1$ then $N = 25$. After finding N , the growth rate value G is found through:

$$y_H \frac{1 - G^N}{1 - G} - \delta_{99} = 0 \quad (3.4)$$

The equation gives the maximum value of G to match the height of the inflation layers δ_{99} . In general automotive applications, boundary wall are valid when y^+ lies between 30 to 300 value (Soares, 2015). In 2D simulation y^+ value can reach below 1 which is the result obtained in case three.

$$y^+ = \frac{\rho u_\tau y_P}{\mu} \quad (3.5)$$

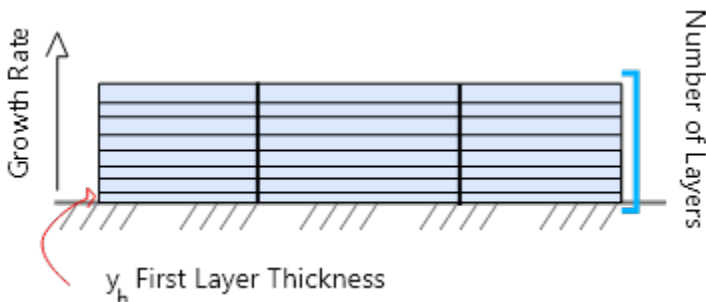


Figure 32: Inflation layer (ANSYS Fluent property) on the wall to represent BLS.

After conducting the first layer thickness calculations, the values are inputted in ANSYS meshing to create the inflation layer. A side view of the generated is shown in Figure 33 for the DrivAer vehicle without the exhaust pipe.

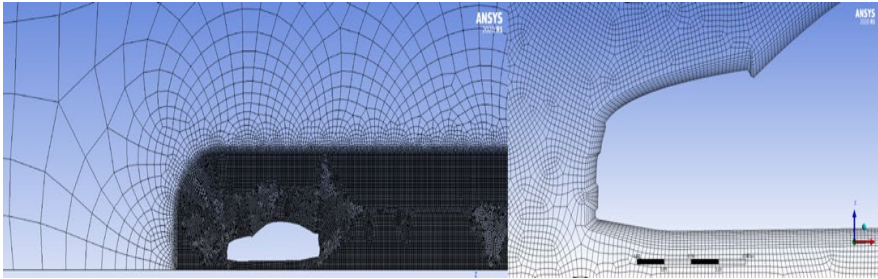


Figure 33: Mesh view showing DrivAer model and mesh.

For the mesh refining process, ANSYS fluent generates automatic mesh at first, and the solver runs, and results are recorded. Then a mesh sizing method is applied, taking the wake structure (Figure 33) applying 50 mm element size, then constantly decreasing the value to 10 mm with a step size of 5 mm. At each step of the mesh refining process, the solver is run, and data is recorded. Figure 34 shows results are in 0.1 drag coefficient range and reaching convergence.

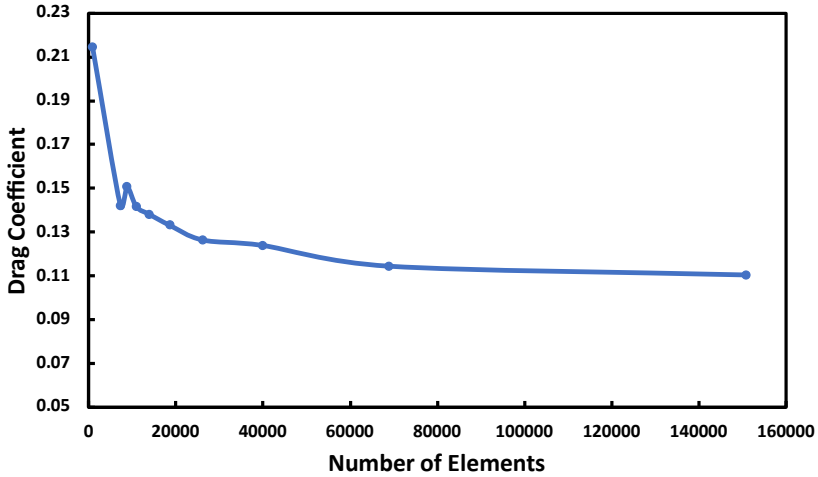


Figure 34: Mesh refining for the 2D DrivAer model to simulate different exhaust pipe position at the error at measure the aerodynamic forces at each position.

3.1.3.1 Turbulent boundary conditions in ANSYS setup

In the ANSYS setup step for the exhaust pipe simulation, several parameters are assumed. However, the assumption isn't always accurate therefore the relevant equations are used to accurately output the values. In any simulation an assumption is made at first for different parameters, then the simulation is run based on these assumptions. It should be noted that calculations are also considered assumptions here since there are no exact equations to represent turbulent flow (including first layer thickness). Therefore, the initial values are set at default values of 5% for turbulent intensity, and eddy viscosity ratio is 10. After the simulation finishes these parameters are extracted, showing the actual values of each parameter. Table 15 shows the initial values and the resulted averaged values from the simulation. For the Shear Stress Transport (SST) K-Omega model the mathematical equations are as follows:

$$k = \frac{3}{2}(UI)^2 \quad (3.6)$$

$$I = \frac{u'}{U} \quad (3.7)$$

$$u' = \sqrt{\frac{1}{3}(u_x'^2 + u_y'^2 + u_z'^2)} = \sqrt{\frac{2}{3}k} \quad (3.8)$$

$$U = \sqrt{U_x^2 + U_y^2 + U_z^2} \quad (3.9)$$

$$\omega = C_\mu^{\frac{3}{4}} \frac{k^{\frac{1}{2}}}{l} \quad (3.10)$$

$$v_t = \frac{k}{\omega} \quad (3.11)$$

Where, k is the turbulent energy, U is the inlet velocity, I is the turbulent intensity, u' is the root-mean-square of the turbulent velocity fluctuations, l is the turbulent length scale, ω is the specific dissipation rate, C_μ is a turbulent model constant with a value of 0.09, and v_t is the turbulent viscosity. The turbulent length scale is the size of eddies that are not resolved.

Table 15: Initial results and the resulted averaged values from the simulation.

Parameter	Assumption	Resulted for 16 m/s
Turbulent Intensity	5%	19.188%
Specific Dissipation Rate (1/s)	277.5199	11726.832
Turbulent Viscosity Ratio	10	3487.588
Turbulent Kinetic Energy (k) (m2/s2)	0.96	14.139
Molecular Viscosity (Kg/m.s)	1.5E-05	1.789E-05
Turbulent Viscosity (kg/m.s)	-	0.062
Turbulent length scale	-	5.269E-05

The 2D setup is set and the mesh type and characteristics are shown in Table 16. An inflation layer is applied to accurately represent the boundary layer separation.

Table 16: 2D DrivAer model mesh setup.

Property	Value
Mesh type	MultiZone Quad/Tri
Wake element size	10 mm
Reynolds number	1.65E+06
Elements	130899
Nodes	131677
Inflation layer mesh properties	
Number of layers	10
Growth rate	1.2
First layer thickness	1.35E-03

It should be noted that there is no such a thing as actual 2D simulation, as ANSYS solver takes the 2D x,y geometry and extends it symmetrically in the z-axis resulting in a 3D simulation. The amount of extension should be twice as the actual 3D representation. For example, in the DrivAer 3D model the width of the vehicle is ~0.4m but in ANSYS 2D solver, the value is inputted as ~0.8m, and only with this number can the simulation result accurate results.

3.2 CFD simulation and results

After preparing the mesh for each case, the simulation is run till convergence where applicable. This section is divided into three sub-sections. First sub-section discusses the results obtained in mirror base simulation part 1 and the concluded results. Then, second sub-section continues part 1 conclusion and shows the orientation that results the least aerodynamic forces and aeroacoustics emissions. Lastly, the third sub-section deals with the

second most significant noise source, the exhaust pipe. The sub-section shows the position on the DrivAer’s rear the results in least aerodynamic forces.

3.2.1 Side mirror base part 1 results

The side mirror base results are divided into aerodynamic forces and acoustics emission from airflow. Each part discusses the relevant results obtained.

3.2.1.1 Acoustics results

Tables 17 and 18 show the acoustics results for both angular and horizontal base position, respectively. The setup methodology in discussed in Chapter 2 with all the required setup parameters. Figure 35 shows the maximum acoustics value for angular and horizontal base position at different airflow inlet velocity. The values obtained show constant difference in acoustics between the two base positions (Figure 35).

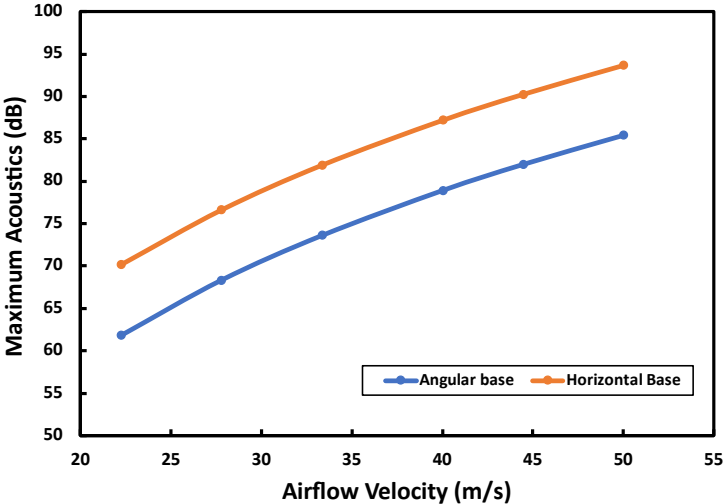


Figure 35: Maximum acoustics value at different airflow inlet velocity for angular and horizontal base position.

Table 17: Angular base mirror acoustics.

Velocity (m/s)	Velocity (km/h)	Maximum APL (dB)	Minimum APL (dB)
22.22	80	61.759	0
27.78	100	68.304	3.360
33.33	120	73.574	9.481
40	144	78.891	15.029
44.44	160	81.962	18.244
50	180	85.410	21.842

Table 18: Horizontal base mirror acoustics.

Velocity (m/s)	Velocity (km/h)	Maximum APL (dB)	Minimum APL (dB)
22.22	80	70.174	0
27.78	100	76.62	2.34232
33.33	120	81.8759	7.86279
40	144	87.1481	13.4029
44.44	160	90.1921	16.6128
50	180	93.6065	20.2091

The Maximum sound for the horizontal base is more than the angular position, however, it is the opposite for the minimum sound, where the horizontal position is slightly lower than the angular position. The location of the highest noise for the horizontal position occurs of about $5.868E-03$ meters closer to the mirror than the angular position. However, the difference between maximum acoustic power level (APL) is almost constant at every velocity. In terms of minimum APL, the difference seems to be decreasing as velocity increases. The aeroacoustics vary due to change in the position vortices are formed. As discussed in Chapter 1 literature review, the sound is generated from air vortices, so the physical explanation is due to moving a

part in the simulation (mirror base) affects the airflow's wake path and the formation of turbulent flow, thus generation of vortices.

3.2.1.2 Aerodynamic forces

The aerodynamic forces lift and drag at each velocity for the mirror and vehicle's side body are presented in Tables 19 and 20. The reason behind similar drag force between the two positions, is due to constant projected frontal area, as drag depends heavily on the frontal area. However, in terms of lift force, the results vary due to the base acting as a wing placed at different pitches. Results obtained are shown in Figure 36 for the drag force, and Figure 37 for the lift force, in terms of different airflow inlet velocities for both angular and horizontal base position. Figure 36 shows the drag results almost identical as both lines are on top of each other. Figure 37 shows slight difference in lift force at higher airflow inlet velocities.

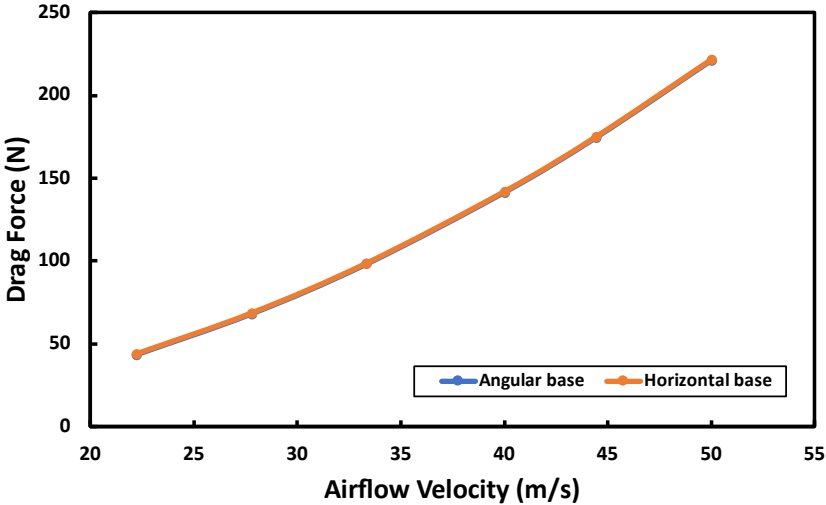


Figure 36: Drag force values at different airflow inlet velocities for angular and horizontal base position.

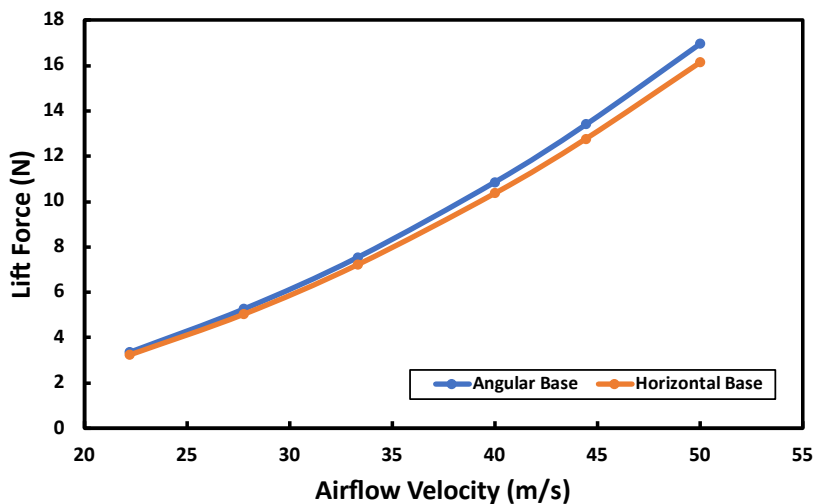


Figure 37: Lift force values at different airflow inlet velocities for angular and horizontal base position.

Table 19: Angular base mirror force results.

Angular Position						
Velocity (m/s)	22.22	27.78	33.33	40	44.44	50
Velocity (km/h)	80	100	120	144	160	180
Drag Mirror Force (N)	43.784	68.404	98.400	141.660	174.823	221.232
Drag Side Force (N)	2.458	3.677	5.091	7.075	8.562	10.599
Lift Mirror Force (N)	3.344	5.254	7.537	10.855	13.403	16.964
Lift Side Force (N)	2.013	3.125	4.612	6.688	8.283	10.533

Table 20: Horizontal base mirror force results.

Horizontal Position						
Velocity (m/s)	22.22	27.78	33.33	40	44.44	50
Velocity (km/h)	80	100	120	144	160	180
Drag Mirror Force (N)	43.862	68.515	98.583	141.927	175.155	221.673
Drag Side Force (N)	2.485	3.705	5.140	7.142	8.640	10.697
Lift Mirror Force (N)	3.216	5.014	7.206	10.353	12.765	16.137
Lift Side Force (N)	1.637	2.583	3.735	5.408	6.688	8.493

Table 19 and 20 values depict that, there is little to no difference in aerodynamic forces. This is logical since for a fair comparison to be conducted, the surface area must be equal and the shape of the mirror. Since both are similar, the results values are also almost the same as well. This proves that the simulation is accurate, as well as that mirror position has no effect on aerodynamic forces. The small difference shows an increase in drag forces but a decrease in lift forces for the horizontal position. Generated results are used to simulate airflow around the mirror for the velocity streamlines as well as the Pressure contour.

Figure 38 shows the rear side view for each base position in terms of velocity streamlines. It is observed that angularly placed mirror base results higher streamline velocity, as shown in the legend, when compared to horizontally placed mirror base. Furthermore, the horizontal base has more airflow passing under the mirror when compared to angular base, where airflow is allowed to pass on the vehicle's side body. Results in Figure 38 prove that although the aerodynamic forces are relatively constant, the airflow streamlines differ significantly, and the vortices created are in different positions.

Figure 39 shows front view of the mirror with pressure contour and airflow velocity streamlines. Figure 39 shows relatively similar pressure

results formed at the mirror surface, but with different velocity values and characteristics. Figure 40 shows the cross section at the mirror center with velocity streamlines. The aim of Figure 40 is to show the turbulent air formed behind the side mirror and the wake structure it forms.

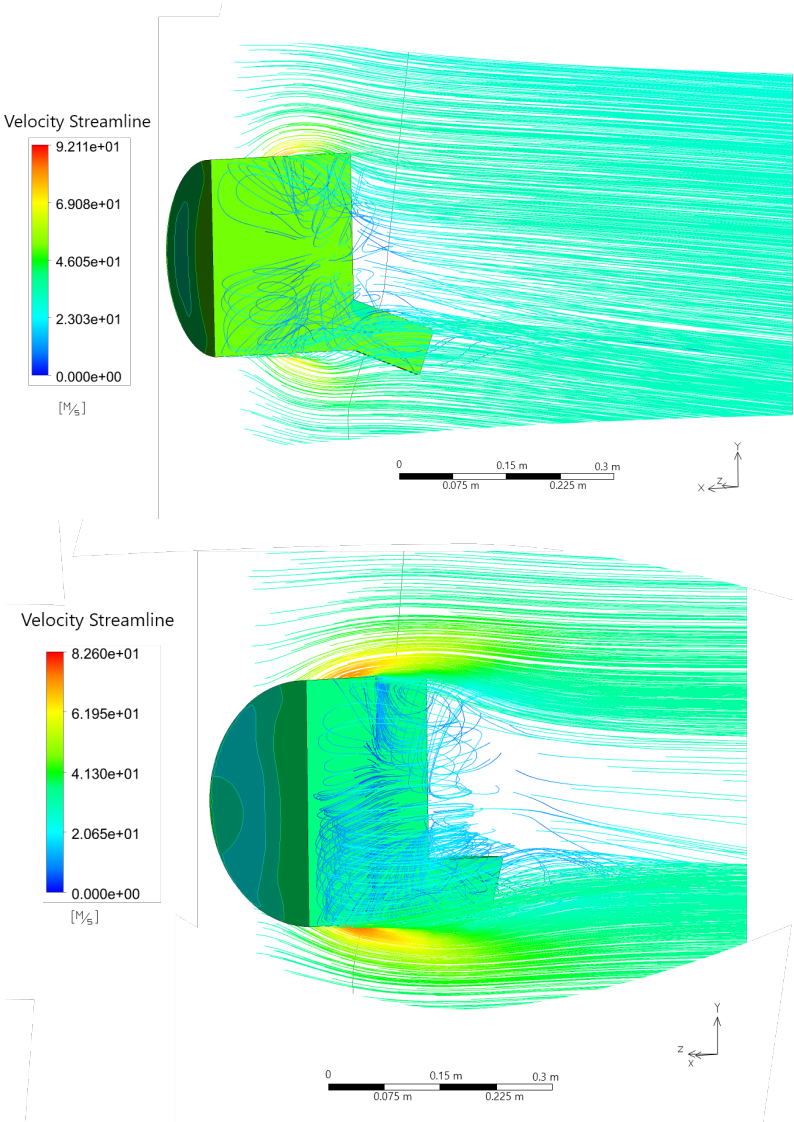


Figure 38: Rear side view of angularly placed mirror base (left) and horizontally placed mirror base (right).

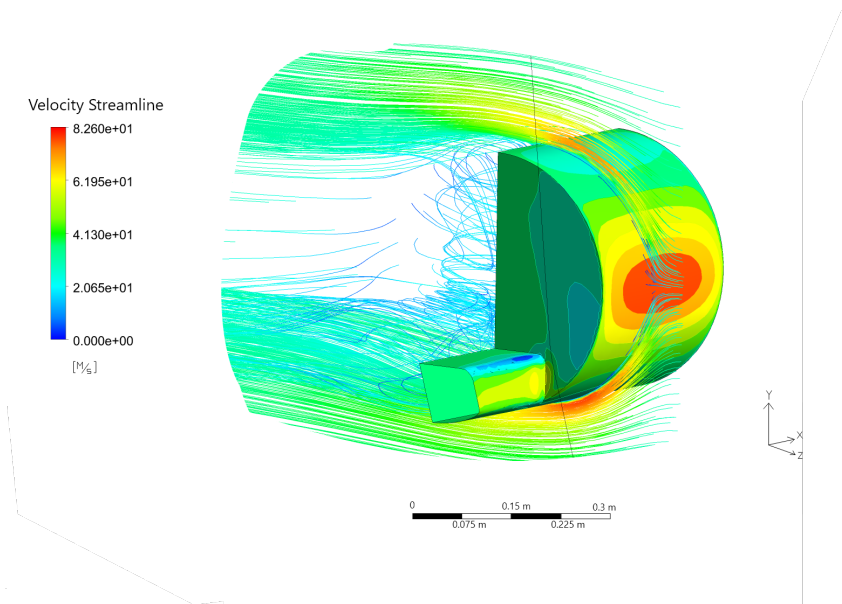
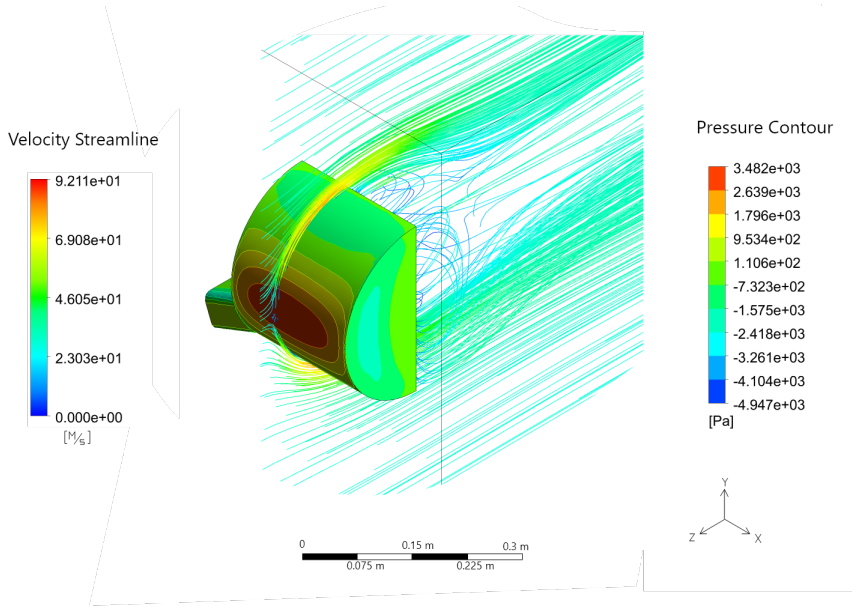


Figure 39: Isometric view for the angularly placed mirror base (left) and front left side view for the horizontally placed mirror base (right).

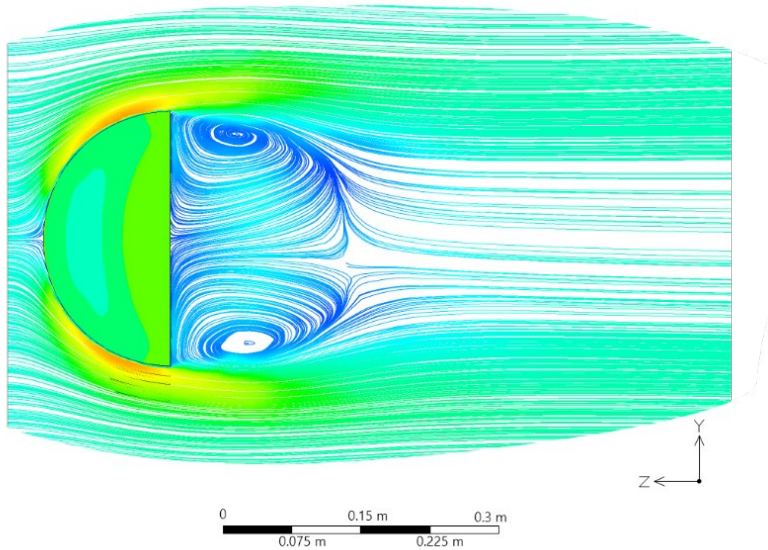


Figure 40: Side view for both positions.

3.2.1.3 Side mirror model part 1 conclusion

The results depict that there is not the major difference between the aerodynamic forces between the two-mirror base positions, however, there is a noticeable difference in APL. The noise generated from the horizontal mirror is much larger than the noise generated from the angular position. This could be due to a larger area of horizontal separation in the horizontal mirror, unlike angular, where air can bypass the base.

This concept is verified by Ehlert et al. (2018) as three different arms (mirror base) are tested experimentally to determine the effect on the aerodynamics and aeroacoustics. The work presented is novel in its idea as the side mirror base effect is severely lacking in the literature. As automobile car companies have said unofficially that angled mirror is ‘better’ without explaining in which sense nor validating their outcome.

3.2.2 Side mirror base results and discussion

Taking the knowledge acquired in previous section that show the mirror's base affects aeroacoustics significantly but not as much in aerodynamic forces. The desired objective is to determine the optimum orientation for the mirror to be placed at those results in lowest aeroacoustics emission. As mentioned previously in Section 2.2.2.6, multiple receivers (sensors) are simulated at the vehicle body, with the focus on the area close to the occupant's ear. Results are collected from each receiver and extracted. When extracting data from receivers, the ANSYS solver outputs pressure fluctuations recordings at each location, and the results are hard to read. Therefore, Fourier Transform with Hanning Window was used to represent the data, taking SPL in decibels in the Y-axis and frequency in the X-axis.

The data obtained is very hectic in values because Fourier transform is applied, and the results show continuous up and down movement in values. Therefore, several procedures (shown in Section 3.2.2.1) were used to determine the best base angle position out of the 26 cases studied. For example, since Fourier Transform results in frequency related parameters, and in terms of sound the magnitude of the SPL at lower frequency is more important than at the higher frequency noise levels, as they are more audible to the driver as discussed in Chapter 1. Furthermore, the 13 receiver's location should also be considered, as the receivers from 5 to 13 in Figure 24 are more important since they are closer to the drivers' ears is shown in Figure 24 and 41. The generated noise closer to the occupant's ears are more important than noise away from the ears. Therefore, Figure 41 is used with dimensions taken based on Toyota Camry 2016 model to figure out where the driver's location will be while travelling inside the vehicle. Utilizing this information, the receivers location is determined as shown in Figure 24.

The acoustic levels at the driver's window is the main concern compared to other locations. From Toyota Camry 2016 model design the

driver’s window/door starts with the mirror from 0.4 till 1.5 meters with the door being 1.1 meters in length as the main area of concern surround the driver as shown in Figure 41 and 8. Receivers location are chosen to focus on the occupant’s head location, as noise generated there has the most noticeable effect on the driver.

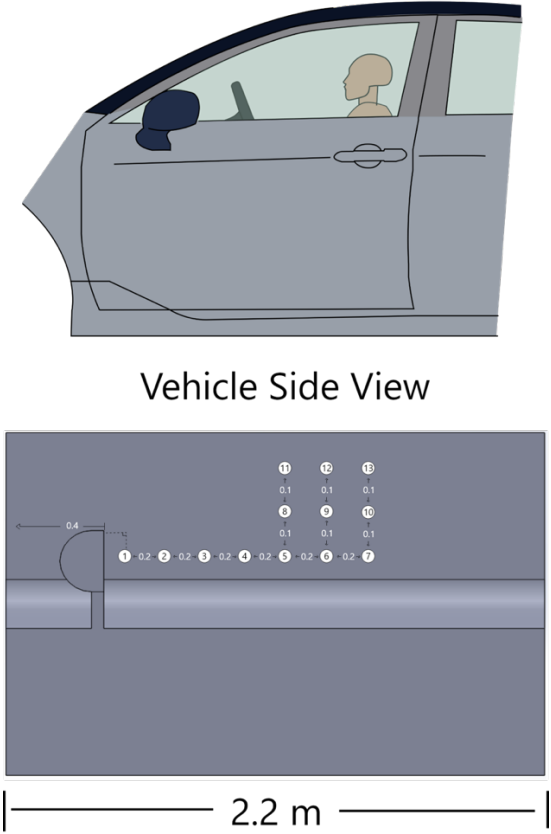


Figure 41: Driver side in vehicle modelled and receivers’ location are placed near the occupants’ ears.

3.2.2.1 Aeroacoustics analysis

The result consists of many up and down curves since it is a Fourier Series (Figure 48), so in order to better understand the data and be able to output a

result, a 4th order polynomial is obtained for each line, to better see the results. The order of polynomial is chosen as the most accurate representation by taking the values at the start of the curve. For example, at 78.75 degrees in receiver 10 the original results starts at 77.4 dB, and when applying polynomial, the starting value is as follows; 2nd order 71, 3rd order 74, 4th order 76, 5th order 80, and 6th order is 82 dB. This shows that the 4th order is the most accurate representation since the value obtained is closest to the original starting value (error 1.8%). The data starts from 10 Hz to 910 Hz, but the first 100 Hz is removed because of error as well as the last 10 Hz as taken from (Yuan et al., 2020).

To choose the optimal angle, the lowest SPL value over the longest period in frequency is desired. Each receiver (Figure 24) is studied based on lowest SPL and the duration it remains the lowest, and the values are presented in Table 21 for the first 12 receivers and Table 22 for receiver number 13. Figure 42 shows the values of angles and the frequency range it remained having the lowest SPL values.

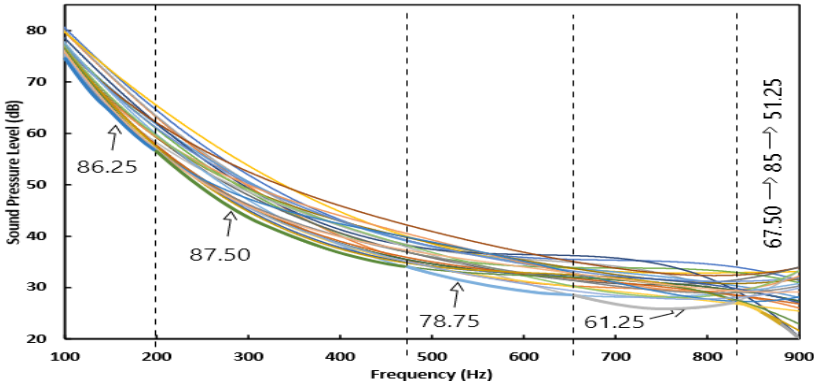


Figure 42: Receiver 1 SPL vs frequency with different mirror base angle positions, with the lowest angle position and the range of frequencies it remains the lowest.

Table 21: Receiver 1 to 12 values for the SPL magnitude for the base angle position and the duration it maintains being the lowest in frequency (Hz).

Receiver 1		Receiver 3		Receiver 5	
Angle in degrees	Frequency Duration (Hz)	Angle in degrees	Frequency Duration (Hz)	Angle in degrees	Frequency Duration (Hz)
86.25	100	86.25	90	88.75	20
87.5	260	85	210	85	390
78.75	190	87.5	130	78.75	140
61.25	170	78.75	60	53.75	100
67.5	10	83.75	200	55	30
85	40	50	50	51.25	120
51.25	30	22.5	60		
Receiver 2		Receiver 4		Receiver 6	
Angle in degrees	Frequency Duration (Hz)	Angle in degrees	Frequency Duration (Hz)	Angle in degrees	Frequency Duration (Hz)
86.25	100	85	360	88.75	90
88.75	200	78.75	150	85	280
87.5	190	83.75	210	90	50
11.25	40	87.5	20	78.75	50
61.25	160	22.5	60	67.5	80
11.25	35			55	160
50	75			87.5	90
Receiver 7		Receiver 9		Receiver 11	
Angle in degrees	Frequency Duration (Hz)	Angle in degrees	Frequency Duration (Hz)	Angle in degrees	Frequency Duration (Hz)
88.75	90	87.5	80	85	380
85	220	85	200	83.75	180
90	130	83.75	220	57.5	110
67.5	60	55	200	50	130
55	210	51.25	100		
87.5	90				

Table 21: Receiver 1 to 12 values for the SPL magnitude for the base angle position and the duration it maintains being the lowest in frequency (Hz) (continued).

Receiver 8		Receiver 10		Receiver 12	
Angle in degrees	Frequency Duration (Hz)	Angle in degrees	Frequency Duration (Hz)	Angle in degrees	Frequency Duration (Hz)
85	410	87.5	95	87.5	30
78.75	130	85	195	85	260
55	90	90	120	90	100
50	70	78.75	90	78.75	100
51.25	40	50	90	83.75	100
22.5	60	55	110	50	210
		83.75	100		

Table 22: Receiver 13 values for the SPL magnitude for the base angle position and the duration it maintains being the lowest in frequency (Hz).

Receiver 13	
Angle in degrees	Frequency Duration (Hz)
87.5	120
85	200
83.75	190
55	140
50	60
22.5	90

Table 21 and 22 summarize the results obtained by each receiver (Figure 48 to 61), where the lowest curve value representing the mirror base angle is mentioned and the duration it remains the lowest. From the observed data, almost each receiver has a different base angle that results lowest

generated acoustics for the longest frequency range, and the results are shown in Table 23.

Table 23: Each receiver number and the mirror base angle that results lowest generated SPL for the longest frequency period.

Receiver Number	Mirror Base Angle (Degrees)
1	87.50
2	88.75
3	85
4	85
5	85
6	85
7	85
8	85
9	83.75
10	85
11	85
12	85
13	85

Figure 48 shows the original results for receiver 1 obtained data from ANSYS solver without applying the 4th order polynomial. The plot of acoustics is divided into 13 figures, each figure for a specific receiver with all the different mirror base angles. Receivers 1, 2, 3, up to 13 are shown in Figures 48, 49, 50, up to 61. The receivers here act as sensors in real life experiment, and they are much more optimistic since other factors are not included. For example, other factors like the sensor’s volume, as sound sensors are large and can affect the airflow and even generate aeroacoustics

noise of its own. In real life experimentation the sound level can't be with a value less than 50-60 dB as this is the ambient noise level.

The obtained results show SPL reaching almost 100 dB (Figure 48) and this might seem to the reader as a huge value, but it is not. Although SPL is measured in dB it is different from the sound amplitude which is also measured in decibels. However, if the sound amplitude reaches above 85 dB could result in permanent ear injury for humans. The SPL is found from sound pressure as follows:

$$SPL(dB) = 10 \log_{10} \left(\frac{p^2}{p_o^2} \right) \quad (3.12)$$

Where, SPL (dB) is the sound pressure level in dB, p is the sound pressure in Pa, and p_o is the reference sound pressure level in Pa which has a fixed value of $20 \mu P$.

The data shows that receiver 1 (Figure 48) recorded the highest SPL value (close to a 100 dB), since closest to the mirror, then the maximum SPL value kept decreasing as in receiver 13 (Figure 61) till it reached around 70 dB. The resulted data obtained had accumulated error, and some values at higher frequencies reached a negative value and this is physically impossible. All these negative errors were disregarded.

After examining a variety of mirror base angles, it is concluded that a mirror base positioned at an angle of 85 degrees from the horizontal level gives the lowest SPL (dB) for the longest frequency range as indicated in all receivers, with values plus and minus 3.75 around the 85 values. This could be related to more air flow passes in between side and mirror, and it redirects turbulent flow from the mirror away from the side window. To illustrate, the more the mirror base angle value the further it is from the side body, thus allowing more linear airflow to pass unaffected by the geometry at the aide body.

The Turbulent Kinetic Energy (TKE) is associated with eddies formed in turbulent flow, it is characterised by the Root Mean Squared (RMS) velocity fluctuations as shown in Equation 3.13, in (m^2/s^2) . The velocity components are solved numerically from the turbulent intensity that is taken as 0.5% in this work (Section 3.1.3.1). The TKE is an important parameter in understanding acoustic generation, as the bigger the TKE value the higher the velocity fluctuations. Velocity fluctuations create vortices which as mentioned before generate acoustics. Therefore, the less the TKE, the lower the acoustic emission. A visual comparison is made between the concluded optimum range of angles (85 ± 3.75 degrees) and another angle with high SPL output to prove the obtained results (45 degrees). Figures 43, and 44 show a comparison between 85 and 45 base mirror angles in the range of $10 m^2/s^2$ TKE. Figures 43 and 44 are concerned with TKE but is represented differently from each other. Figure 42 shows TKE value in isosurface isometric view, and Figure 44 shows TKE in isosurface side profile view. Isosurface is a 3D representation of points with equal magnitude, vortex core region is a region in a fluid where flow revolves around an axis line, and volume rendering is just a 3D representation of the values.

$$TKE = \frac{1}{2} (\overline{(u')^2} + \overline{(v')^2} + \overline{(w')^2}) \quad (3.13)$$

Where, u' , v' , and w' are the velocity components in the x, y, and z axis. The TKE Figures 42 and 43 created support the conclusion that the angle 85 degrees have the lowest noise emissions. This means, lower TKE value since they are proportional.

In terms of frequency the Strouhal number is usually used to determine the predominant frequency value f_s in the following equation:

$$Sr = \frac{f_s L}{U_\infty} \quad (3.14)$$

Where L is the characteristic length, and U_∞ is the freestream velocity. The Strouhal Number (Sr) is found to be a function of Reynolds number. However, in this work the Reynolds number equal to 5.95×10^6 which is turbulent flow and results vortex shedding over a wide range of frequencies, which cannot be determined analytically.

Since the range of 85 ± 3.75 degrees is chosen to be the optimum position to result in the lowest noise emission possible. To prove the difference in results between angles a comparison is made between the optimum 85 degree and 45 degrees. The results show that there is a 40-degree difference, but the noise emitted difference is significant with a value up to 32 dB in SPL (Figure 45).

Figure 44 gives a side profile view which shows the concentration of the eddies and vortices, and at the 85 degrees the shape spreads out to the lower part of the vehicle, while at 45 degrees it focuses on the driver's window, causing high noise emission close to the driver's ears. These results prove the validity of the outcomes of this study as there is large difference in SPL when changing the mirror base position.

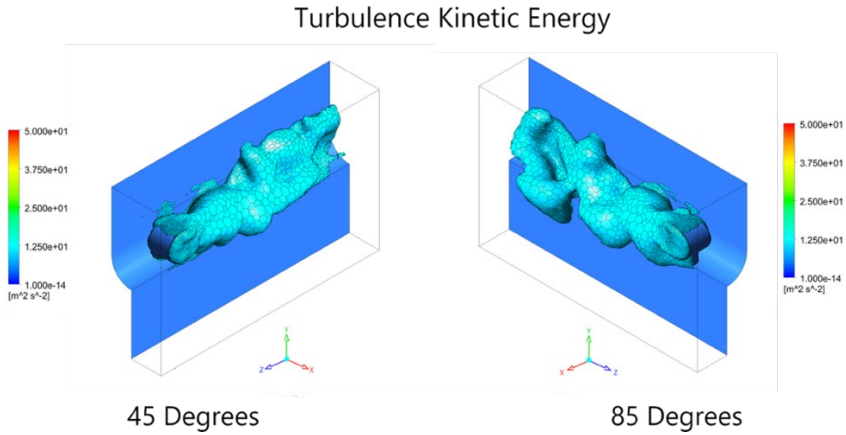


Figure 43: Turbulence kinetic energy isometric view comparing between 45 and 85 degrees.

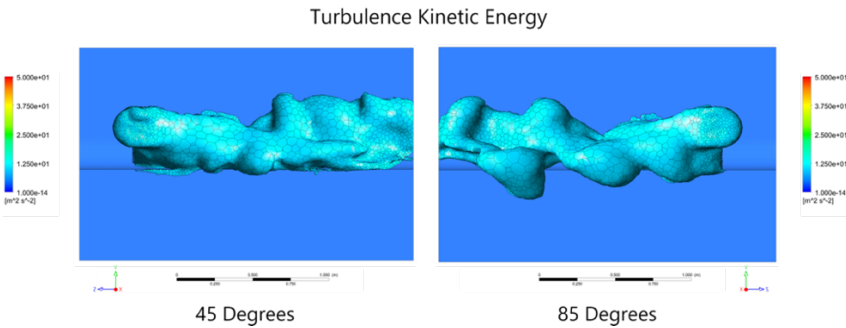


Figure 44: Turbulence Kinetic Energy side profile view comparing between 45 and 85 degrees.

Noise at 300 Hz is considered harmful and could cause headaches when subjected to for long periods of time, and the results from Figure 48 to 61 show the spread of values around 300 Hz. To measure the difference of SPL at different receivers, the frequency value is fixed at 300 Hz and the 85-degree base is compared with 45 degrees as shown in Figure 45 for receiver 13. It is obvious that, the value of SPL at receivers 1 and 2 seem close between the two angles, but as the receivers move away from the mirror the difference

appears more and more significant, reaching around 32 dB at receiver 11. This observation is logical since the area close to the mirror mainly shows the mirror effect as it is the larger geometry but as the distance increases the effect of the base mirror starts to show. Again, this proves the optimum base angle is at 85 degrees as this angle achieve the most vehicle comfort and ride quality, by reducing the emitted noise.

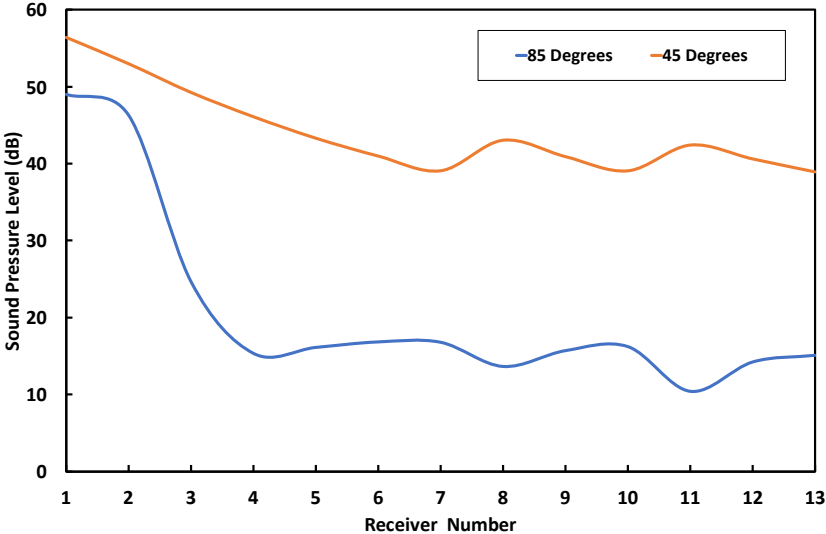


Figure 45: SPL at different receivers for fixed frequency of around 300 Hz: Comparison between 45 and 85 degrees.

3.2.2.2 Aerodynamic force analysis

Results for aerodynamic forces (Figure 46) are obtained in a separate simulation using a steady state that uses K-Omega model unlike the acoustics model which is simulated in transient flow. The figure is combined with the SPL acoustic values taken at receiver 13 since it is the closest to the driver’s ear at a fixed frequency of around 300 Hz. The 300 Hz value is chosen because the values there are spread out and easily differentiable as can be seen from the acoustics plot (Figure 46). In terms of aerodynamic forces, the drag

side and mirror are almost constant for every angle, and this is because the surface area is constant, and as (Dong et al., 2014) concluded by the drag equation, that drag is directly proportional to the projected area. The aerodynamic drag force obtained proves the efficiency of the developed comparison model and its preciseness. As the focus here was to isolate the acoustics effect by having a constant projected area and having a constant drag force is an indicative parameter for the developed and its valid/applicability. However, the lift force varies constantly, as a mirror act somehow as aircraft wings, and this lift the vehicle upwards as discussed by (Lee & Ho, 1990). These results consider the positive y-axis pointing upward, so the bigger the value of the lift force the worse it is for vehicle stability. Unlike in aircrafts the upward lift is desired for flying and taking the plane off the ground, but in terms of vehicles stability downward lift is desired to push the vehicle to the ground, as the more the vehicle hugs the ground the better. Although there is an increase in lift force when changing the angle of the base mirror, the change is relatively small with a maximum value reaching around 15 N. The 15 N value is not capable of lifting the vehicle or cause major stability change, since most vehicles weight is more than 1000 Kg. The slight lift force is due to air passing upwards faster than downward of the body, creating a pressure difference, where the lower side has more pressure, thus going upwards to the lower pressure area as discussed by (Auton, 1987). At 0-degree angle, the lift force is at its minimum; this is related to having turbulent air created from the side of the vehicle under the mirror. The lift force value keeps increasing then decrease sharply for the 90-degree angle. The reason for this is similar to the 0-degree angle, which has enough surrounding area not to affect the airspeed in either direction. This effect is due to separation and wake region created by the mirror and base being very close which results a big zone of low-pressure wake. Adding the SPL to Figure 45, adds more insight on the results, and proves the conclusion

obtained is accurate as it can be seen the angle of 85 degrees and the surrounding 3.75 degrees have the lowest noise emission.

In Figure 46, the aerodynamic forces are obtained for the mirror part (mirror and mirror base) and plotted with respect to the mirror base angle. Furthermore, the SPL at 300 Hz for receiver 13 is added to the plot with own y-axis (right).

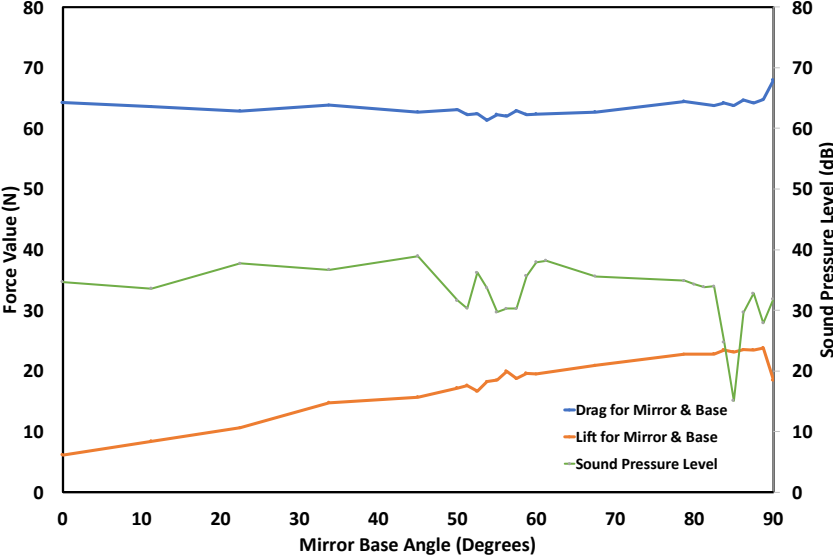


Figure 46: Aerodynamic forces for the mirror part and SPL at receiver 13 both presented for each mirror base angle.

3.2.2.3 Side mirror part 2 results and discussion

Since this thesis explores a research gap that has not been studied before, experimental validation is not available in the literature yet. However, the obtained results follow an expected trend of past articles that studied the mirror such as the work done by (Belamri et al., 2007), and this is used to validate the results. The experimental data done by (Belamri et al., 2007) focused on the side mirror part with similar dimensions and resulted up to

1000 Hz noise and with similar starting SPL value of around 100 dB, which is similar to the obtained results in this thesis. Therefore, the obtained results are validated, as they show similar trend in values and behaviour of results. Figure 47 shows a comparison between the results obtained and the already existing numerical and experimental results done by (Belamri et al., 2007). The result shows good correlation with the trend of results. The different values are due to the fact that (Belamri et al., 2007) have considered only the mirror, but in this thesis the mirror base is considered as well, so results should not have similar values. There is also a shift in values due to slightly closer receiver position towards the mirror, and as mentioned previously in this section, that the closer the receiver to the mirror the higher the maximum SPL value. To illustrate, (Belamri et al., 2007) obtained the results at 0.1 m from the mirror part, and in this thesis, receiver 1 is 0.2 m away from the mirror. Receiver 1 is also not in the wake region of the mirror, but it is placed on the vehicle's side, unlike (Belamri et al., 2007) experimentation where the receiver is in the wake of the mirror. The difference in the setup explains the difference in results, but the results behave in similar manner when increasing the frequency values.

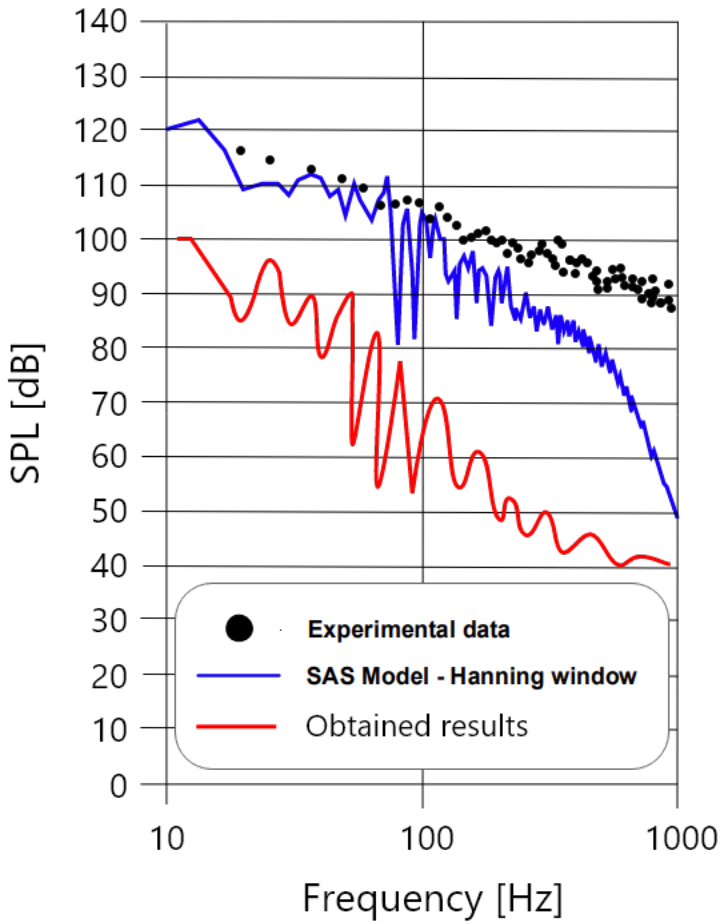


Figure 47: Obtained results compared with previous work done in literature.

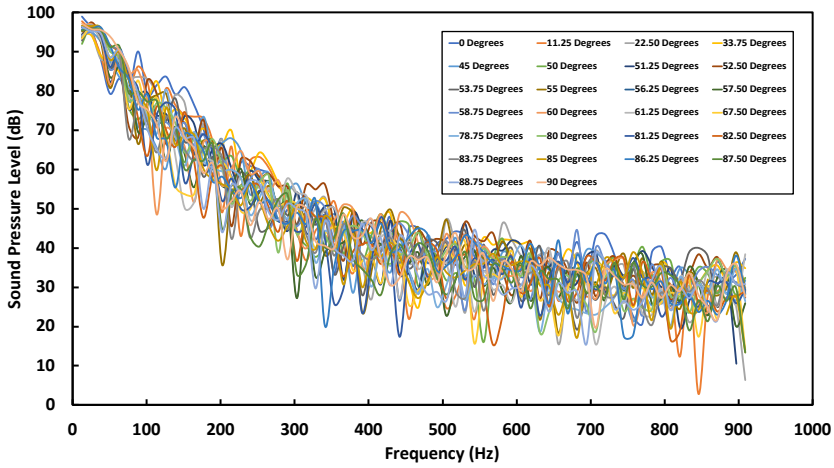


Figure 48: Receiver 1 at different mirror base angles original results from ANSYS solver.

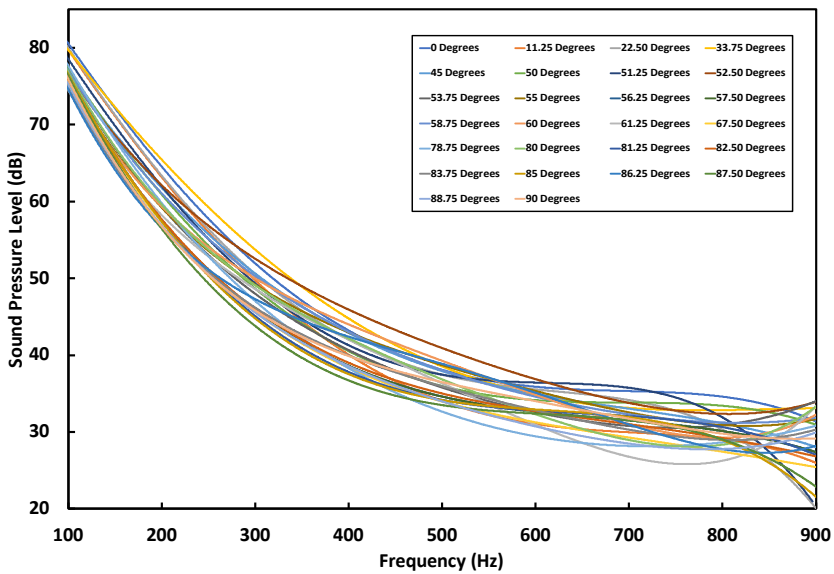


Figure 49: Receiver 1 at different mirror base angles with 4th order polynomial.

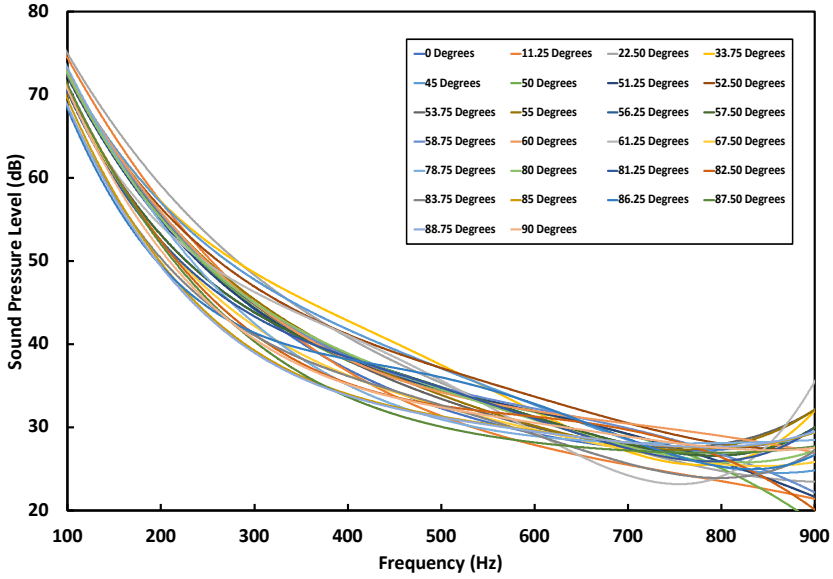


Figure 50: Receiver 2 at different mirror base angles with 4th order polynomial.

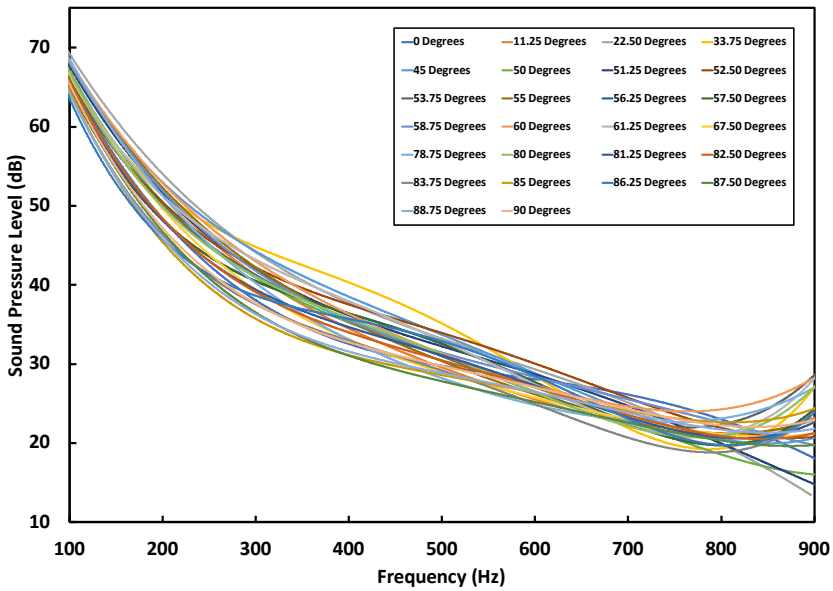


Figure 51: Receiver 3 at different mirror base angles with 4th order polynomial.

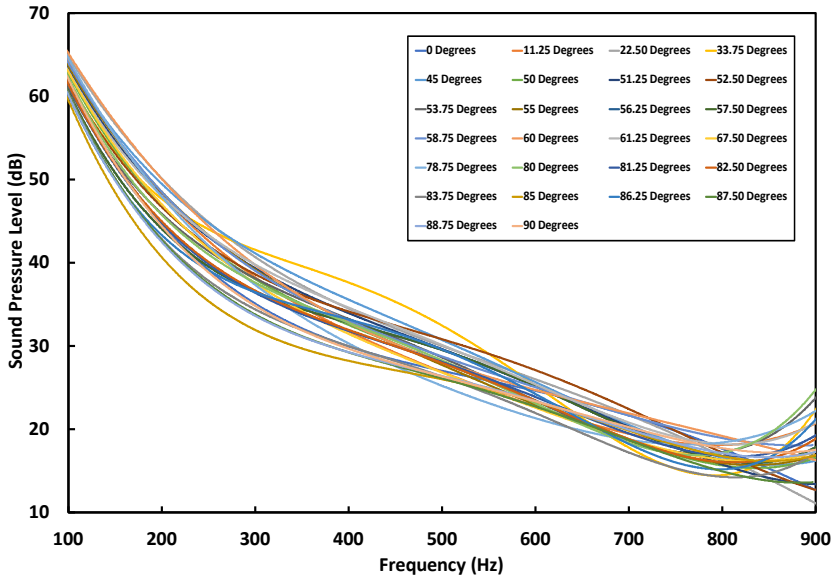


Figure 52: Receiver 4 at different mirror base angles with 4th order polynomial.

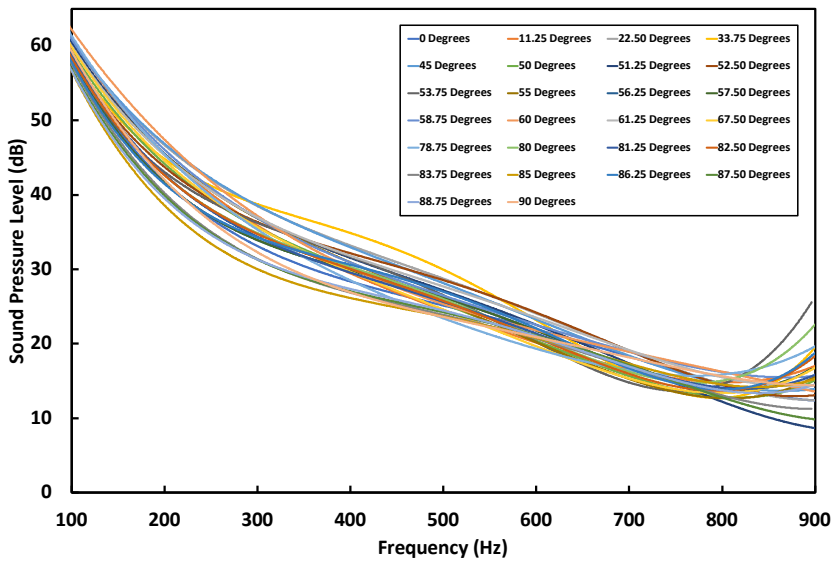


Figure 53: Receiver 5 at different mirror base angles with 4th order polynomial.

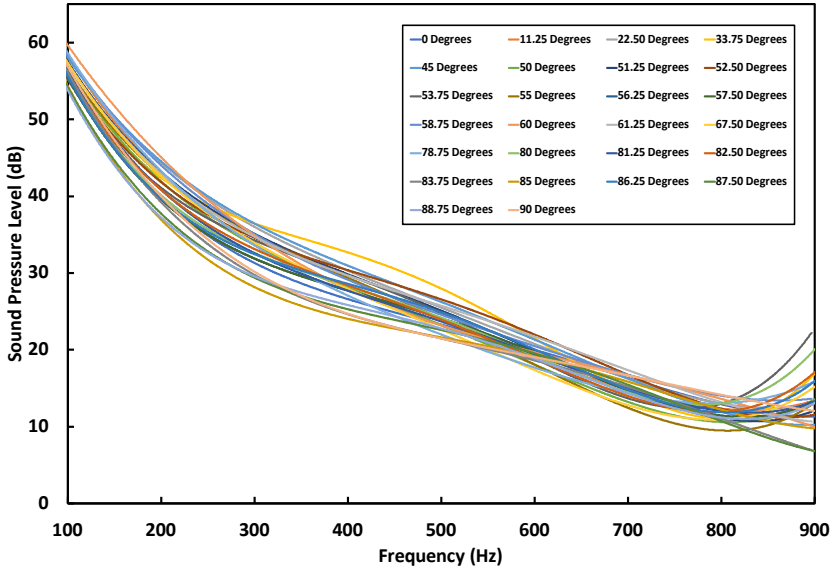


Figure 54: Receiver 6 at different mirror base angles with 4th order polynomial.

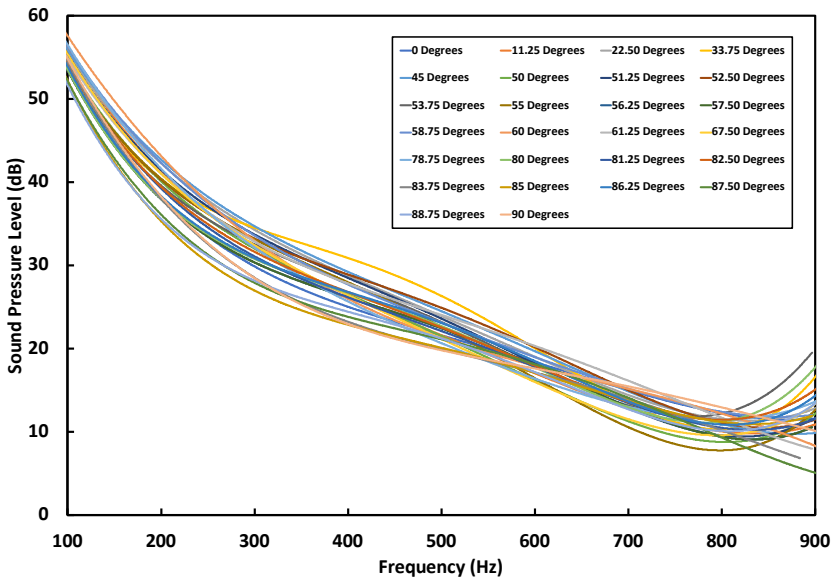


Figure 55: Receiver 7 at different mirror base angles with 4th order polynomial.

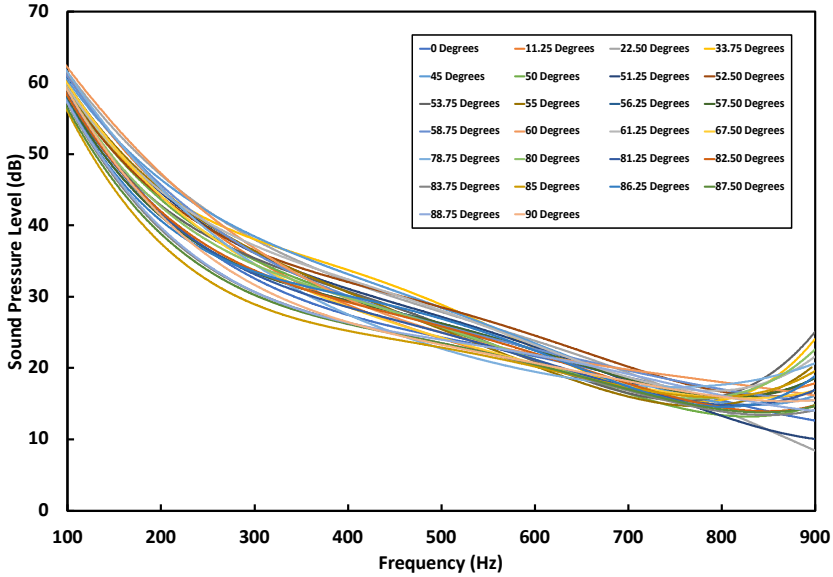


Figure 56: Receiver 8 at different mirror base angles with 4th order polynomial.

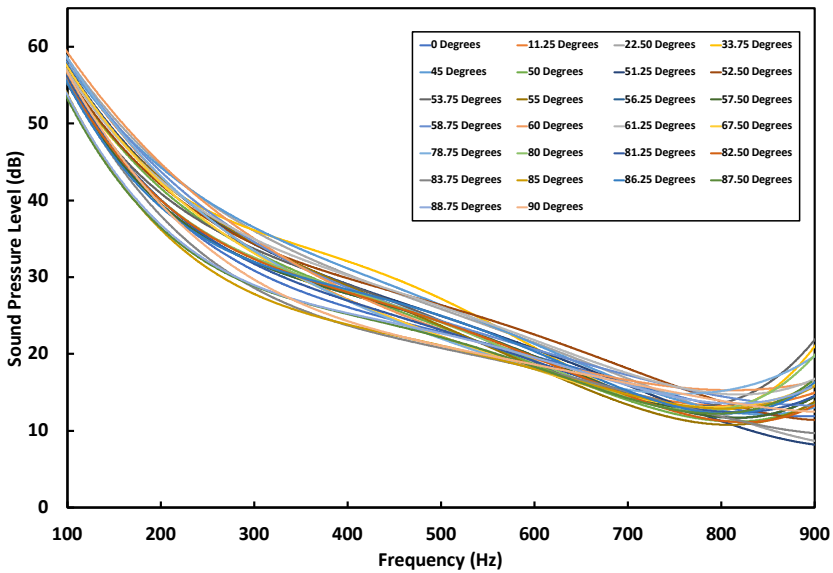


Figure 57: Receiver 9 at different mirror base angles with 4th order polynomial.

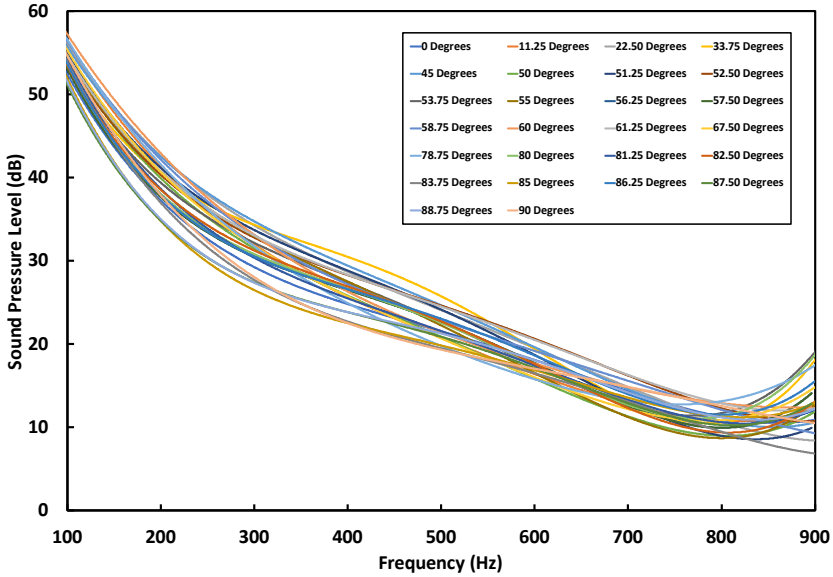


Figure 58: Receiver 10 at different mirror base angles with 4th order polynomial.

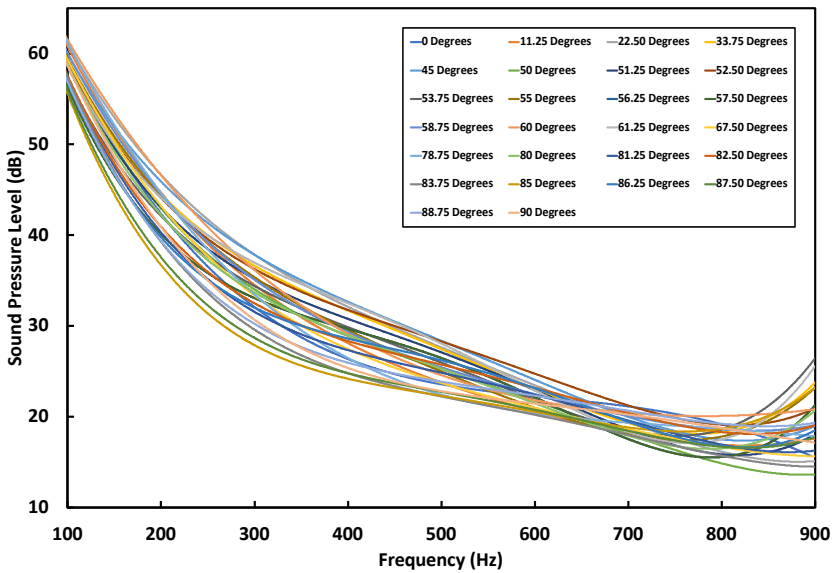


Figure 59: Receiver 11 at different mirror base angles with 4th order polynomial.

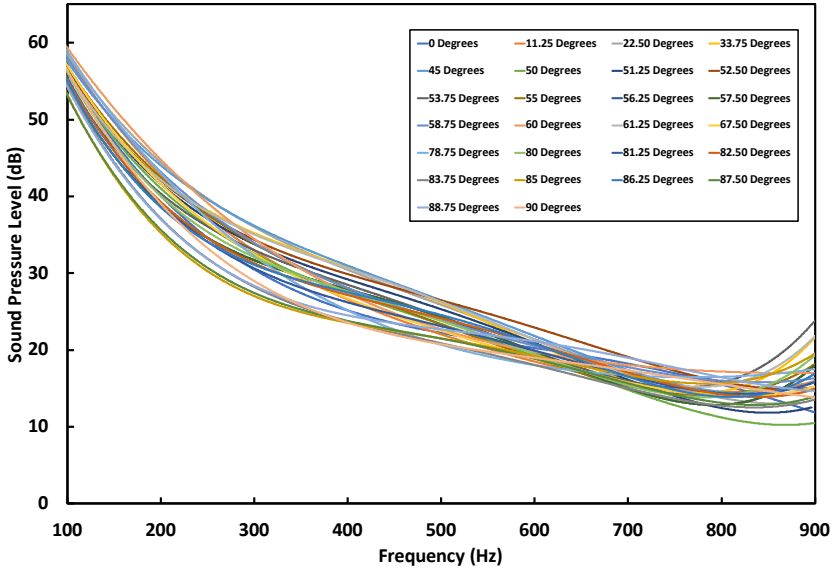


Figure 60: Receiver 12 at different mirror base angles with 4th order polynomial.

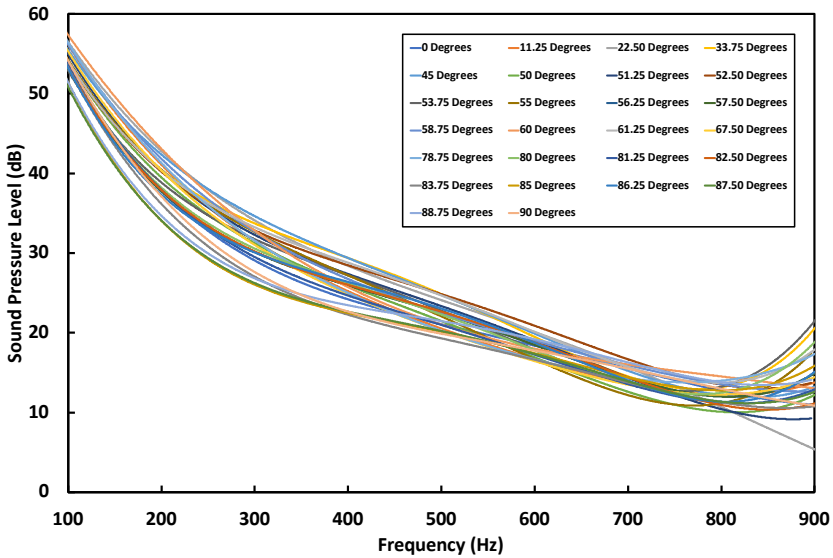


Figure 61: Receiver 13 at different mirror base angles with 4th order polynomial.

3.2.3 Exhaust pipe at different positions results and discussion

Simulating multiple positions at the rear for the exhaust pipe to be placed at is conducted, and at each position the aerodynamic forces are reported. The exhaust pipe is positioned at the rear of the DrivAer model as shown in Figure 62 and previously Figure 25. Since the exhaust pipe ejects gases, the outlet mass interacts with outside air and affects the air pressure contours, thus affecting the aerodynamic forces.

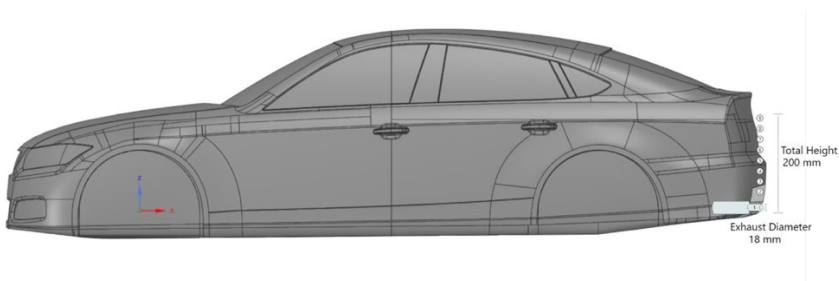


Figure 62: DrivAer 2D fastback model without wheels, with exhaust pipe at the rear of the vehicle positioned at 9 different locations (zoom out of Figure 25).

3.2.3.1 Aerodynamic forces results

Referencing Figures 25 and 62 which show the different positions for the exhaust pipe, the aerodynamic forces results obtained are shown in Tables 24, 25, and 26. In terms of lift coefficient (Tables 24, 25, and 26), position 6 has the biggest negative lift coefficient (close to position 4) value of -0.4768 with a 7.73% increase in negative value than the original, and position 9 has the lowest negative lift coefficient value of -0.2605 with a significant difference of 41.13%. As mentioned before the more negative the lift coefficient the greater the downward force, which results greater vehicle stability. The generated results as shown in Figure 63 and 64. Figure 63 shows the least drag coefficient is achieved at position 5 and the highest drag

coefficient is at position 4. Furthermore, Figure 64 shows the highest negative value is achieved at position 6 and the lowest negative value is at position 9.

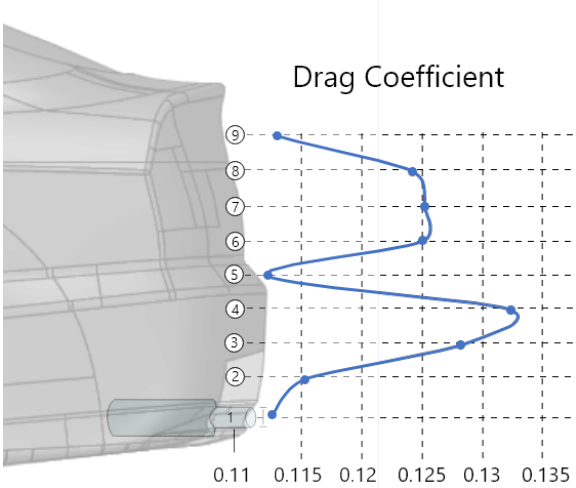


Figure 63: Drag coefficient plot for each exhaust pipe position.

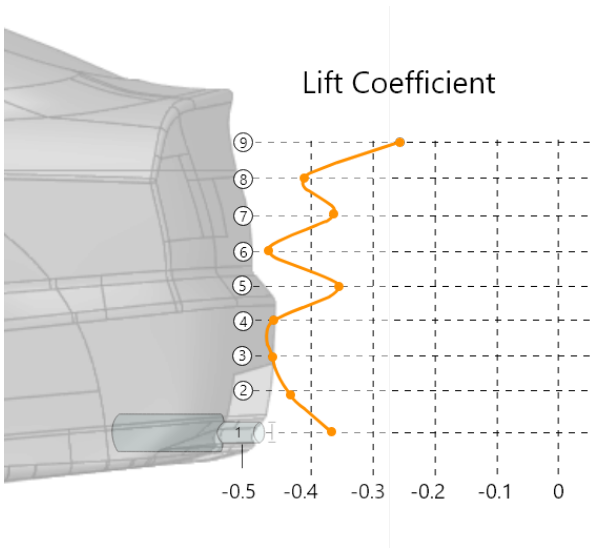


Figure 64: Lift coefficient plot for each exhaust pipe position.

The significant negative decrease in lift noticed at position 9 is due to difference in pressure contours as shown in Figure 65 which compares between velocity contours between exhaust located at position 6 and 9. Figure 65 also shows the difference in velocity under the vehicle (velocity legend), and it is known that the higher the velocity the lower the pressure. Therefore, at position 6 the pressure under the vehicle is high when compared to lower pressure at the top of the vehicle (Figure 65), this pressure difference creates a force towards the lower pressure contour, therefore resulting the highest negative lift at position 6. The low velocity under the vehicle for position 6 is due the exhaust located above the centre of the rear which creates a high velocity stream coming from the exhaust, that travels downwards. It is also noted that position 6 has a higher drag than position 9 due to the same effect. This long drag wake at the rear creates as an opposite to a vacuum for the air under the vehicle, which works more as squeezing the air under the vehicle body, that results a lower velocity air under the vehicle.

The difference in drag coefficient between position 4 and 5 is shown in Figure 66. Figure 66 shows the clear difference in drag wake region at the rear of the DrivAer model, as when the exhaust is placed at position 4 it creates a longer vacuum profile than when placed at position 5. The longer vacuum is explained by position 4 having a centre position to the wake at the rear of the vehicle. This advantage of being placed at the centre of wake works as an addition to the wake length. Unlike position 5 which is located at the top of the centre of the wake, works against the drag profile by reducing influencing the profile direction. The effect of position 5 is also shown under the vehicle, as position 5 exhaust has lower negative lift than position 4.

Of course, most vehicles have the exhaust system positioned at position 1, which reduces the drag and increases the negative lift. Position 1 has a drag coefficient value of 0.1125 which is 7.91% lower than the verification value, and very close the lowest Cd obtained at position 5. For

the lift coefficient the value is less negative than the verification model with a value of -0.3725, which is 15.82% negative decrease (Table 24, 25, and 26).

Table 24: Aerodynamic forces values for exhaust located at positions 1 to 3 with change %.

Variable	Original	Position 1	Change %	Position 2	Change%	Position 3	Change %
Drag Coefficient	0.1222	0.1125	7.9135	0.1151	5.7247	0.1282	-4.9353
Lift Coefficient	-0.4426	-0.3725	15.8273	-0.4390	0.7989	-0.4696	-6.1153

Table 25: Aerodynamic forces values for exhaust located at positions 4 to 6 with change %.

Variable	Original	Position 4	Change %	Position 5	Change %	Position 6	Change %
Drag Coefficient	0.1222	0.1324	-8.3778	0.1121	8.2373	0.1250	-2.3466
Lift Coefficient	-0.4426	-0.4713	-6.4997	-0.3614	18.3321	-0.4768	-7.7299

Table 26: Aerodynamic forces values for exhaust located at positions 7 to 9 with change %.

Variable	Original	Position 7	Change %	Position 8	Change %	Position 9	Change %
Drag Coefficient	0.1222	0.1251	-2.4244	0.1242	-1.6295	0.1129	7.5562
Lift Coefficient	-0.4426	-0.3683	16.7867	-0.4184	5.4775	-0.2605	41.1370

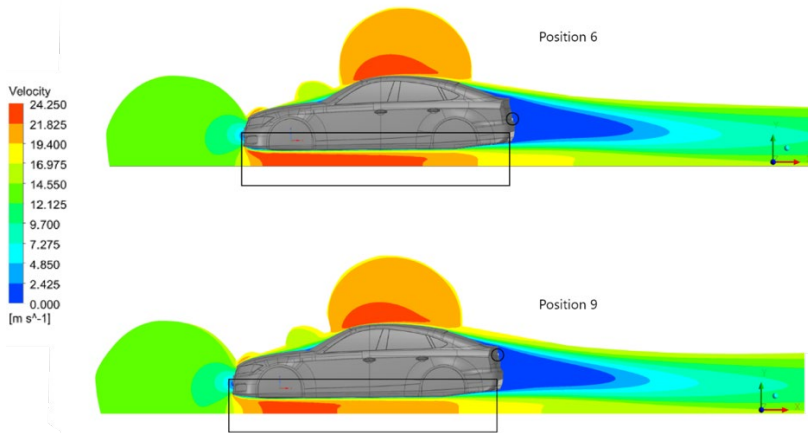


Figure 65: Velocity contours for exhaust located at position 6 and 9.

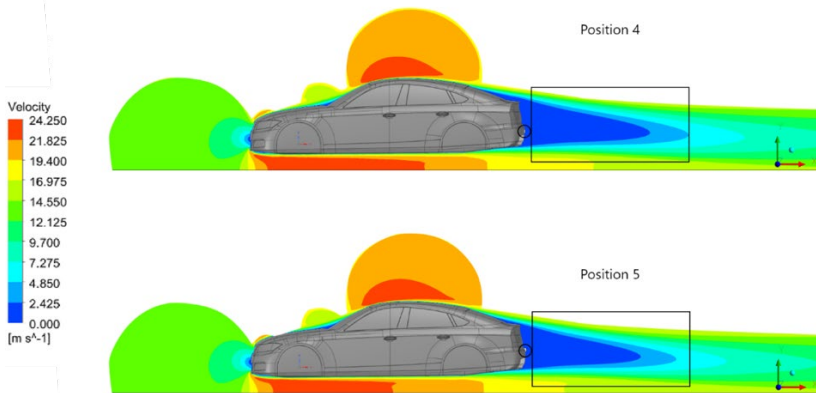


Figure 66: Velocity contours for exhaust located at position 4 and 5.

3.2.3.2 Experimental validation from literature

In terms of experimental validation, the model used is the DrivAer model with the addition of the exhaust pipe at the rear. Therefore, a numerical validation is valid by solving for the aerodynamic forces of the DrivAer model and comparing the values obtained with the available experimental data.

In terms of verification of mesh, the value of y^+ is followed for the DrivAer profile and the result is set as the maximum y^+ value to be in the range from 30 to 300, which is considered very accurate. Using the previous mentioned equations of inflation layer (Section 3.1.3), at a Reynolds number of $1.65e6$ the boundary layer thickness is 0.035 meters at the vehicle body. To obtain an accurate representation of the boundary layer, 10 inflation layers are chosen with a growth ratio of 1.2 this results a first layer thickness of $1.35E-03$ meters. The obtained y^+ value for min, avg, and max are 4, 110, and 227, respectively. After conducting the simulation, the drag coefficient values are obtained for the DrivAer 2D profile, and Table 27 shows the obtained results for the DrivAer fastback without mirrors and without wheels model in 2D simulation compared to the existing experimental data done by (Heft et al., 2012a) for the same geometry. Moreover, the resulted numerical drag coefficient is compared to (Heft et al., 2012a) numerical value and the result obtained show higher accuracy than (Heft et al., 2012a).

Table 27: Drag coefficient values: comparison between experimental and numerical.

Experimental drag coefficient by (Heft et al., 2012a)	0.125
Numerical drag coefficient by (Heft et al., 2012a)	0.115
(Heft et al., 2012a) error percentage	8%
Obtained drag coefficient	0.122
Error percentage to experimental	2.4%

3.2.3.3 Rear exhaust pipe position conclusion and discussion

After conducting the simulation, the results are shown in Tables 24, 25, and 26. The results show position 5 resulting the lowest drag coefficient of 0.1121 with a difference percentage lower than the verified original DrivAer model value of 8.37%, and the 25 mm lower position 4 results the

highest drag coefficient value of 0.1324 with a difference of 8.23% more than the original.

From the obtained results, it is clearly shown that exhaust pipe placed at position 6 has the optimum effect on the vehicle's aerodynamic forces. Even though the drag coefficient is bigger than position 5, the change is slight. Therefore, in terms of drag coefficient, position 5 is the optimum position as it results the least aerodynamic coefficient. However, in terms of lift coefficient the value obtained at position 6 is the most negative value and therefore the optimum position for the exhaust pipe if lowest lift coefficient is desired.

The outputted value for drag is similar to the experimental results, since 2D should result similar results to 3D. The error is around 2.4% which is due to the numerical errors, and error in predicting fluid behavior. However, the error is acceptable, and the results are satisfactory. Therefore, the numerical results obtained for all exhaust positions are experimentally validated by (Heft et al., 2012a).

Chapter 4

Chapter 4: Conclusions and Future Work

4.1 Conclusions

In this thesis, the effect of changing a mirror base on aerodynamic forces and acoustics generated is studied. Furthermore, following the mirror base conclusion, further study is done to determine the optimum position that results in least aeroacoustics generated. Lastly, the exhaust pipe is simulated at different placements on the vehicle's rear to determine the height relative to the ground, that results in least aerodynamic forces. The following summarizes the main findings of the thesis:

- 1) Mirror base position only slightly affects vehicle aerodynamics. However, it does on acoustics, where horizontal mirror position generates significantly more noise than mirrors placed in angular position. Furthermore, as long as the projected surface area is constant, the aerodynamic forces are not affected by changing the base orientation. Therefore, aerodynamic forces minimization does not necessarily mean lower acoustics generation.
- 2) It is concluded that the optimal mirror's base angle that results lowest aeroacoustics is at 85 ± 3.75 degrees angle, and relatively the lowest lift force compared to the surrounding orientations. As results show that if the base of the mirror is placed at 85 ± 3.75 degrees from the horizontal axis this results least noise emission compared to all other angles studied. Furthermore, the aerodynamic force analysis shows almost constant drag force, but changing lift force, as increasing the angle increases the lift force until reaching 90 degrees where the force drops significantly but still isn't as small as 0 degrees. Although there is a change in lift force the maximum change is around 15 newtons, and this small increase doesn't affect the vehicle stability as much as the effect on reducing noise emission. When comparing the optimum angle of 85 degrees to the 45-

degree angle, significant difference in noise emission is noticed, reaching up to 32 dB. The work concluded an industry standard design for mirror base.

- 3) The effect of exhaust tail pipe position at different heights on the aerodynamic forces over 2D realistic DrivAer model is presented in this study. The exhaust pipe has a significant effect on aerodynamic forces, especially lift. The traditional position of exhaust pipe at the rear bottom affects the vehicle's aerodynamics negatively and decreases the overall efficiency. However, a vertical height increase of 100 mm results the lowest drag coefficient value, and further 25 mm increase results in lowest lift coefficient value.

4.2 Future work

Further work can be carried out to investigate and expand the potentials of the suggested base mirror orientation and exhaust pipe position. In terms of the mirror part, work could be done to create a system that adapts to air velocity and changes mirror tilt angle without affecting the driver's side view, to result in least aerodynamic forces and acoustics generated at every air velocity. Furthermore, in terms of exhaust pipe, further work can be done in 3D space on the aerodynamic effect of different number of exhaust pipes.

References

- Afgan, I., Moulinec, C., & Laurence, D. (2008). Numerical simulation of generic side mirror of a car using large eddy simulation with polyhedral meshes. *International Journal for Numerical Methods in Fluids*, 56(8), 1107–1113. <https://doi.org/10.1002/flid.1719>
- Ahmed, S. R. (1981). An experimental study of the wake structures of typical automobile shapes. *Journal of Wind Engineering and Industrial Aerodynamics*, 9(1-2), 49–62. [https://doi.org/10.1016/0167-6105\(81\)90077-5](https://doi.org/10.1016/0167-6105(81)90077-5)
- Ahmed, S. R., Ramm, G., & Faltin, G. (1984). Some Salient Features of the time averaged Ground. *SAE Transactions*, 93(1984), 473–503. <https://doi.org/10.4271/840300>
- Aljure, D. E., Calafell, J., Baez, A., & Oliva, A. (2018). Flow over a realistic car model: Wall modeled large eddy simulations assessment and unsteady effects. *Journal of Wind Engineering and Industrial Aerodynamics*, 174, 225–240. <https://doi.org/10.1016/j.jweia.2017.12.027>
- Ask, J., & Davidson, L. (2005). The near field acoustics of a generic side mirror based on an incompressible approach. Chalmers University of Technology. Report 05/05
- Ask, J., & Davidson, L. (2006). The sub-critical flow past a generic side mirror and its impact on sound generation and propagation. *Collection of Technical Papers - 12th AIAA/CEAS Aeroacoustics Conference*, 3(May), 1925–1944. <https://doi.org/10.2514/6.2006-2558>
- Ask, J., & Davidson, L. (2009). A numerical investigation of the flow past a generic side mirror and its impact on sound generation. *Journal of Fluids Engineering, Transactions of the ASME*, 131(6), 0621011–06110212. <https://doi.org/10.1115/1.3129122>
- Auton, T. R. (1987). The lift force on a spherical body in a rotational flow. *Journal of Fluid Mechanics*, 183, 199–218. <https://doi.org/10.1017/S002211208700260X>
- Bauer, W. D., Wenisch, J., & Heywood, J. B. (1998). Averaged and time-resolved heat transfer of steady and pulsating entry flow in intake manifold of a spark-ignition engine. *International Journal of Heat and Fluid Flow*, 19(1), 1–9. [https://doi.org/10.1016/S0142-727X\(97\)10001-7](https://doi.org/10.1016/S0142-727X(97)10001-7)

- Bauskar, M. P., Dhande, D. Y., Vadgeri, S., & Patil, S. R. (2019). Study of aerodynamic drag of sports utility vehicle by experimental and numerical method. *Materials Today: Proceedings*, 16, 750–757. <https://doi.org/10.1016/j.matpr.2019.05.155>
- Belamri, T., Egorov, Y., & Menter, F. (2007). CFD simulation of the aeroacoustic noise generated by a generic side view car mirror. 13th AIAA/CEAS Aeroacoustics Conference (28th AIAA Aeroacoustics Conference), 1–12. <https://doi.org/10.2514/6.2007-3568>
- Bernard, R. . (2010). *Road Vehicle Aerodynamic Design (Third Edition)*. Mechaero Publishing.
- Blanchet, D., Golota, A., Zerbib, N., & Mebarek, L. (2014). Wind noise source characterization and how it can be used to predict vehicle interior noise (No. 2014-01-2052). *SAE Technical Papers*. <https://doi.org/10.4271/2014-01-2052>
- Bremner, P. G., & Wilby, J. F. (2002). Aero-vibro-acoustics: Problem statement and methods for simulation-based design solution. In 8th AIAA/CEAS Aeroacoustics Conference and Exhibit (p. 2551). <https://doi.org/10.2514/6.2002-2551>
- Bremner, Paul G., & Zhu, M. (2003). Recent progress using SEA and CFD to predict interior wind noise. *SAE International*, 2003-01-1705. <https://doi.org/10.4271/2003-01-1705>
- Caton, J. A., & Heywood, J. B. (1981). An experimental and analytical study of heat transfer in an engine exhaust port. *International Journal of Heat and Mass Transfer*, 24(4), 581–595. [https://doi.org/10.1016/0017-9310\(81\)90003-X](https://doi.org/10.1016/0017-9310(81)90003-X)
- Chaouat, B. (2017). The State of the Art of Hybrid RANS/LES Modeling for the Simulation of Turbulent Flows. *Flow, Turbulence and Combustion*, 99(2), 279–327. <https://doi.org/10.1007/s10494-017-9828-8>
- Chode, K. K., Viswanathan, H., & Chow, K. (2021). Noise emitted from a generic side-view mirror with different aspect ratios and inclinations. *Physics of Fluids*, 33(8), 084105. <https://doi.org/10.1063/5.0057166>
- Cogotti, A. (1998). A parametric study on the ground effect of a simplified car model. *SAE Technical Papers*, 107, 180–204. <https://doi.org/10.4271/980031>

- Constantinescu, G. S., & Squires, K. D. (2000). LES and DES investigations of turbulent flow over a sphere. 38th Aerospace Sciences Meeting and Exhibit, 267–298. <https://doi.org/10.2514/6.2000-540>
- Constantinescu, G., & Squires, K. (2004). Numerical investigations of flow over a sphere in the subcritical and supercritical regimes. *Physics of Fluids*, 16(5), 1449–1466. <https://doi.org/10.1063/1.1688325>
- Dong, S., Zheng, L., Zhang, X., & Lin, P. (2014). Improved drag force model and its application in simulating nanofluid flow. *Microfluidics and nanofluidics*, 17(2), 253–261. <https://doi.org/10.1007/s10404-014-1330-1>
- Egorov, Y., Menter, F., Lechner, R., & Cokljat, D. (2010). The Scale-Adaptive Simulation Method for Unsteady Turbulent Flow Predictions. Part 2: Application to Complex Flows. *Flow, Turbulence and Combustion*, 85, 139–165. <https://doi.org/10.1007/s10494-010-9265-4>
- Ehlert, G. J., Chapman, R. J., & Thomas, R. S. (2018). Wind Noise and Aerodynamic Drag optimization of outside rear view mirrors. *SAE International*, 931292. <https://doi.org/10.4271/931292>
- Ferziger, J. H., Peric, M., & Leonard, A. (1997). Computational Methods for Fluid Dynamics. *Physics Today*, 50(3), 80. <https://doi.org/10.1063/1.881751>
- Ffowes Williams, J. E., and Hawkings, D. L. (1969). Sound generation by turbulence and surfaces in arbitrary motion. *Philosophical Transactions of the Royal Society of London. Serie A, Mathematical and Physical Sciences*, 264(1151), 321–342. <https://doi.org/10.1098/rsta.1969.0031>
- Goines, L., & Hagler, L. (2007). Noise pollution: a modern plague. *Southern Medical Journal. South Med J*, 100(3), 287–294.
- Guilmineau, E. (2008). Computational study of flow around a simplified car body. *Journal of Wind Engineering and Industrial Aerodynamics*, 96(6–7), 1207–1217. <https://doi.org/10.1016/j.jweia.2007.06.041>
- Haag, L., Kiewat, M., Indinger, T., & Blacha, T. (2017). Numerical and experimental investigation of rotating wheel aerodynamics on the DrivAer model with engine bay flow. *ASME*, 1–13. <https://doi.org/10.1115/FEDSM2017-69305>

- Harrison, M. (2004). Interior noise: assessment and control. *Vehicle Refinement*, 145–233. <https://doi.org/10.1016/b978-075066129-4/50006-7>
- Hartmann, M., Ocker, J., Lemke, T., Mutzke, A., Schwarz, V., Tokuno, H., Toppinga, R., Unterlechner, P., & Wickern, G. (2012). Wind noise caused by the a-pillar and the side mirror flow of a generic vehicle model. 18th AIAA/CEAS. In *CEAS Aeroacoustics Conference* (pp. 2012-2205).
- Haselton, M. G., & Buss, D. M. (2000). Error management theory: A new perspective on biases in cross-sex mind reading. *Journal of Personality and Social Psychology*, 78(1), 81–91. <https://doi.org/10.1037/0022-3514.78.1.81>
- Haselton, M. G., & Nettle, D. (2006). The paranoid optimist: An integrative evolutionary model of cognitive biases. *Personality and Social Psychology Review*, 10(1), 47–66. https://doi.org/10.1207/s15327957pspr1001_3
- Heft, A. I., Indinger, T., & Adams, N. A. (2012, July). Experimental and numerical investigation of the DrivAer model. In *Fluids Engineering Division Summer Meeting*. American Society of Mechanical Engineers. 44755, 41-51. <https://doi.org/10.1115/FEDSM2012-72272>
- Heft, A. I., Indinger, T., & Adams, N. A. (2012b). Introduction of a new realistic generic car model for aerodynamic investigations. *SAE Technical Papers*, 1–5. <https://doi.org/10.4271/2012-01-0168>
- Höld, R., Brenneis, A., Eberle, A., Schwarz, V., & Siegert, R. (1999). Numerical simulation of aeroacoustic sound generated by generic bodies placed on a plate: Part I - Prediction of aeroacoustic sources. 5th AIAA/CEAS Aeroacoustics Conference and Exhibit, May. <https://doi.org/10.2514/6.1999-1896>
- Huang, T., Kohonen, T., & Schroeder, M. (1988). *Psychoacoustics*. Springer.
- Jasak, H. (1996). Error analysis and estimation for the finite volume method with applications to fluid flows. (Master's thesis). Imperial College, UK
- Kim, D., Safdari, A., & Kim, K. C. (2021). Sound pressure level spectrum analysis by combination of 4D PTV and ANFIS method around automotive side-view mirror models. *Scientific Reports*, 11(1), 1–16. <https://doi.org/10.1038/s41598-021-90734-1>

- Kim, J. H., & Han, Y. O. (2011). Experimental investigation of wake structure around an external rear view mirror of a passenger car. *Journal of Wind Engineering and Industrial Aerodynamics*, 99(12), 1197–1206. <https://doi.org/10.1016/j.jweia.2011.10.002>
- Kok, J. C. (2000). Resolving the dependence on freestream values for the $k-\omega$ turbulence model. *AIAA Journal*, 38(7), 1292–1295. <https://doi.org/10.2514/2.1101>
- Kshirsagar, V., & Chopade, J. V. (2018). Aerodynamics of high performance vehicles. *International Research Journal of Engineering and Technology (IRJET)*, 5(03), 2395-0056.
- Lee, M., & Ho, C. (1990). Lift force of delta wings. *American Society of Mechanical Engineers*, 43(9), 209-221.
- Li, A., & Sharma, A. (2021). Aeroacoustic analysis of an air amplifier. *Aerospace Research Central*, 2022–2561. <https://doi.org/10.2514/6.2022-2561>
- Li, B., Ye, C. C., Wan, Z. H., Liu, N. S., Sun, D. J., & Lu, X. Y. (2020). Noise control of subsonic flow past open cavities based on porous floors. *Physics of Fluids*, 32(12), 125101 <https://doi.org/10.1063/5.0028689>
- Lighthill, M. J. (1952). On sound generated aerodynamically I. General theory. *Proceedings of the Royal Society of London. Series A. Mathematical and Physical Sciences*, 211(1107), 564–587. <https://doi.org/10.1098/rspa.1952.0060>
- Liu, H., Lu, Y., Yang, J., Wang, X., Ju, J., Tu, J., Yang, Z., Wang, H., & Lai, X. (2021). Aeroacoustic optimization of the bionic leading edge of a typical blade for performance improvement. *Machines*, 9(8), 175. <https://doi.org/10.3390/machines9080175>
- Löfdahl, L. (2005). A Brief History of Road Vehicle Aerodynamics. In *Chalmers Applied Mechanics*. Göteborg, Sweden.
- Lorenz, K. (1943). The innate forms of potential experience. *Z Tierpsychol*, 5, 235–409.
- LucidMotors. (2020, June 30). Lucid Air Is the World’s Most Aero-Efficient Luxury Car. *Lucidmotors.com*. Retrieved July 26, 2022, from <https://www.lucidmotors.com/stories/lucid-air-is-worlds-most-aero-efficient-luxury-car>

- Mahato, B., Ganta, N., & Bhumkar, Y. G. (2020). Mitigation of aerodynamic sound for a laminar flow past a square cylinder using a pair of cowl plates. *Physics of Fluids*, 32, 076108. <https://doi.org/10.1063/5.0010932>
- Maisonneuve, N., Stevens, M., Niessen, M. E., Hanappe, P., & Steels, L. (2009). Citizen noise pollution monitoring. <https://doi.org/10.1145/1556176.1556198>
- Maury, C., Bravo, T., & Pinhède, C. (2012, April). Laboratory synthesis of turbulent boundary layer wall-pressures and the induced vibro-acoustic response. In *Acoustics 2012* (No. Session AH-S01: Wall pressure fluctuations-Paper 57)
- Maxit, L., & Denis, V. (2013). Prediction of flow induced sound and vibration of periodically stiffened plates. *The Journal of the Acoustical Society of America*, 133(1), 146–160. <https://doi.org/10.1121/1.4768875>
- Menter, F. R. (1992). Influence of freestream values on $k-\omega$ turbulence model predictions. *AIAA Journal*, 30(6), 1657–1659. <https://doi.org/10.2514/3.11115>
- Nasif, G., Balachandar, R., & Barron, R. M. (2019). Influence of bed proximity on the three-dimensional characteristics of the wake of a sharp-edged bluff body. *Physics of Fluids*, 31(2), 025116. <https://doi.org/10.1063/1.5085666>
- Navier, C.-L. M. H. (1822). Sur les lois du mouvement des fluides, en ayant égard à l'adhésion de leurs molécules. *Bull. Soc. Philomath*, 59–75.
- Of, C., & European, T. H. E. (2017). Future noise policy: European commission green paper. *Noise News International*, 5(2), 74–94. <https://doi.org/10.3397/1.3703028>
- Parliament, T. H. E. E. C., & Union, E. (2001). Assessment and Management of Environmental Risks. *Assessment and Management of Environmental Risks*, 12–25. <https://doi.org/10.1007/978-94-010-0987-4>
- Peng, G. C. (2011). Measurement of exterior surface pressures and interior cabin noise in response to vehicle form changes. *SAE International*. <https://doi.org/10.4271/2011-01-1618>
- Rotta, J. (1951). Statistische Theorie nichthomogener Turbulenz. *Zeitschrift Für Physik*, 129(6), 547–572. <https://doi.org/10.1007/BF01330059>

- Rüttgers, M., Park, J., & You, D. (2019). Large-eddy simulation of turbulent flow over the DrivAer fastback vehicle model. *Journal of Wind Engineering and Industrial Aerodynamics*, 186, 123–138. <https://doi.org/10.1016/j.jweia.2019.01.003>
- Schmidt, S., & Thiele, F. (2003). Detached Eddy Simulation of Flow Around A-Airfoil. *Flow, Turbulence and Combustion*, 71(1–4), 261–278. <https://doi.org/10.1023/B:APPL.0000014933.66058.22>
- Shur, M., Spalart, P. R., Strelets, M., & Travin, A. (1999). Detached-eddy simulation of an airfoil at high angle of attack. In *Engineering Turbulence Modelling and Experiments 4*. Woodhead Publishing Limited. <https://doi.org/10.1016/b978-008043328-8/50064-3>
- Siegert, R., Schwarz, V., & Reichenberger, J. (1999). Numerical simulation of aeroacoustic sound generated by generic bodies placed on a plate: Part II - Prediction of radiated sound pressure. 5th AIAA/CEAS Aeroacoustics Conference and Exhibit, May. <https://doi.org/10.2514/6.1999-1895>
- Singh, N., & Davar, S. C. (2004). Noise Pollution-Sources, Effects and Control. *Journal of Human Ecology*, 16(3), 181–187. <https://doi.org/10.1080/09709274.2004.11905735>
- Soares, R. (2015). Drag of Road Cars: Cost-Effective CFD Setup, Proposal of an Aerodynamic Concept and Case Studies. (Master's thesis). Federal University of Uberlândia.
- Soares, R. F., Knowles, A., Goñalons Olives, S., Garry, K., & Holt, J. (2018). On the Aerodynamics of an Enclosed-Wheel Racing Car: An Assessment and Proposal of Add-On Devices for a Fourth, High-Performance Configuration of the DrivAer Model. *SAE Technical Papers*, 2018-April, 1–27. <https://doi.org/10.4271/2018-01-0725>
- Spalart, P. R. (2000). Strategies for turbulence modelling and simulations. *International Journal of Heat and Fluid Flow*, 21(3), 252–263. [https://doi.org/10.1016/S0142-727X\(00\)00007-2](https://doi.org/10.1016/S0142-727X(00)00007-2)
- Stansfeld, S. A., & Matheson, M. P. (2003). Noise pollution: Non-auditory effects on health. *British Medical Bulletin*, 68, 243–257. <https://doi.org/10.1093/bmb/ldg033>
- Stokes, G. G. (1850). On the Effect of the Internal Friction of Fluids on the Motion of Pendulums. *Mathematical and Physical Papers*, 1–10. <https://doi.org/10.1017/cbo9780511702266.002>

- Strelets, M. (2001). Detached eddy simulation of massively separated flows. *American Institute of Aeronautics & Astronautics*, 20191–4344. <https://doi.org/10.2514/6.2001-879>
- Taştan, U. (2011). Investigation of turbulence models used in automotive industry (Master's thesis, Middle East Technical University).
- Travin, A., Shur, M., Strelets, M., & Spalart, P. (2000). Detached-eddy simulations past a circular cylinder. *Flow, Turbulence and Combustion*, 63(1), 293–313. <https://doi.org/10.1023/a:1009901401183>
- Van Herpe, F., Bordji, M., Baresch, D., & Lafon, P. (2011). Wavenumber-frequency analysis of the wall pressure fluctuations in the wake of a car side mirror. 17th AIAA/CEAS Aeroacoustics Conference 2011 (32nd AIAA Aeroacoustics Conference), June, 5–8. <https://doi.org/10.2514/6.2011-2936>
- Vatsa, V. N., & Singer, B. A. (2003). Evaluation of a second-order accurate Navier-Stokes code for detached eddy simulation past a circular cylinder. 21st AIAA Applied Aerodynamics Conference, June, 1–9. <https://doi.org/10.2514/6.2003-4085>
- Wang, Y., Thompson, D., & Hu, Z. (2019). Effect of wall proximity on the flow over a cube and the implications for the noise emitted. *Physics of Fluids*, 31(7), 077101. <https://doi.org/10.1063/1.5096072>
- Wang, Y., Thompson, D., & Hu, Z. (2020). Numerical investigations on the flow over cuboids with different aspect ratios and the emitted noise. *Physics of Fluids*, 32(2), 025103. <https://doi.org/10.1063/1.5131827>
- Watkins, S., & Oswald, G. (1999). The flow field of automobile add-ons - With particular reference to the vibration of external mirrors. *Journal of Wind Engineering and Industrial Aerodynamics*, 83(1–3), 541–554. [https://doi.org/10.1016/S0167-6105\(99\)00100-2](https://doi.org/10.1016/S0167-6105(99)00100-2)
- Weckmüller, C., Guérin, S., Wellner, J., & Michel, U. (2010). Ffowcs williams & hawkins formulation for the convective wave equation and permeable data surface. 16th AIAA/CEAS Aeroacoustics Conference (31st AIAA Aeroacoustics Conference), 1–13. <https://doi.org/10.2514/6.2010-3710>
- Wilcox, D. C. (1988). Reassessment of the scale-determining equation for advanced turbulence models. *AIAA Journal*, 26(11), 1299–1310. <https://doi.org/10.2514/3.10041>

- Wilcox, D. C. (1998). Turbulence modeling for CFD (Vol. 2, pp. 103-217). La Canada, CA: DCW industries.
- Wilcox, D. C. (2008). Formulation of the $k-\omega$ turbulence model revisited. *AIAA Journal*, 46(11), 2823–2838. <https://doi.org/10.2514/1.36541>
- Windhager, S., Hutzler, F., Carbon, C. C., Oberzaucher, E., Schaefer, K., Thorstensen, T., Leder, H., & Grammer, K. (2010). Laying eyes on headlights: Eye movements suggest facial features in cars. *Collegium Antropologicum*, 34(3), 1075–1080.
- Wu, J., Stalnov, O., Chen, W., Yang, Z., & Huang, X. (2022). Transient analysis of blade-vortex interaction noise. *Aerospace Science and Technology*, 120, 107294. <https://doi.org/10.1016/j.ast.2021.107294>
- Yao, H. D., & Davidson, L. (2018). Generation of interior cavity noise due to window vibration excited by turbulent flows past a generic side-view mirror. *Physics of Fluids*, 30(3), 036104. <https://doi.org/10.1063/1.5008611>
- Yao, H. D., Davidson, L., & Eriksson, L. E. (2017). Noise radiated by low-Reynolds number flows past a hemisphere at $Ma = 0.3$. *Physics of Fluids*, 29(7), 1–14. <https://doi.org/10.1063/1.4994592>
- Ye, J., Xu, M., Xing, P., Cheng, Y., Meng, D., Tang, Y., & Zhu, M. (2021). Investigation of aerodynamic noise reduction of exterior side view mirror based on bionic shark fin structure. *Applied Acoustics*, 182, 108188. <https://doi.org/10.1016/j.apacoust.2021.108188>
- Yuan, H., Yang, Z., Wang, Y., Fan, Y., & Fang, Y. (2020). Experimental analysis of hydrodynamic and acoustic pressure on automotive front side window. *Journal of Sound and Vibration*, 476(March 2021), 115296. <https://doi.org/10.1016/j.jsv.2020.115296>
- Zaareer, M., & Mourad, A. H. (2021). Effect of Vehicle Side Mirror Base Position on Aerodynamic Forces and Acoustics. *Alexandria Engineering*, 61(2), 1437–1448. <https://doi.org/10.1016/j.aej.2021.06.049>

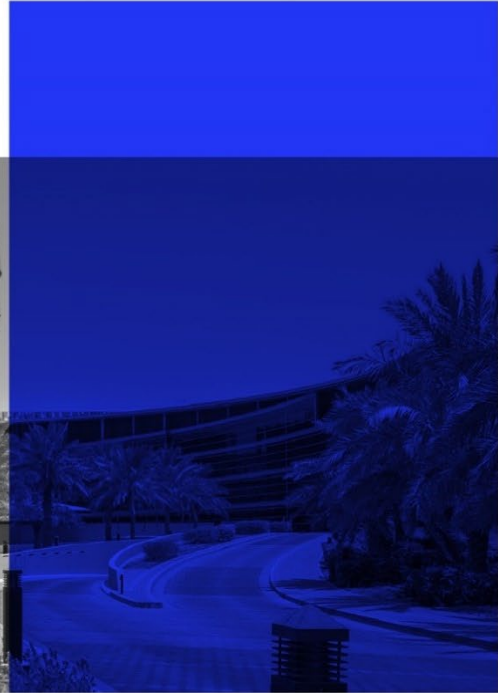
List of Publications

Zaareer, M., & Mourad, A. H. (2021). Effect of Vehicle Side Mirror Base Position on Aerodynamic Forces and Acoustics. *Alexandria Engineering*, 61(2), 1437–1448.
<https://doi.org/10.1016/j.aej.2021.06.049>



UAEU

جامعة الإمارات العربية المتحدة
United Arab Emirates University



UAE UNIVERSITY MASTER THESIS NO. 2022: 39

This master thesis has pursued the goal of investigation of automotive aerodynamics by means of CFD methodology. Two major noise sources are studied in terms of aerodynamics and/or aeroacoustics, and the optimum position or orientation is determined that results either least aerodynamic forces or least acoustics generation.

Moath Nayef Mohamed Zaareer received his Master of Science in Mechanical Engineering from the Department of Mechanical and Aerospace Engineering, College of Engineering at UAE University, UAE. He received her BSc from the College of Science, UAE University, UAE.

www.uaeu.ac.ae

Online publication of thesis:
<https://scholarworks.uaeu.ac.ae/etds/>

UAEU عمادة المكتبات
Libraries Deanship

جامعة الإمارات العربية المتحدة
United Arab Emirates University

قسم الخدمات المكتبية الرقمية - Digital Library Services Section